An investigation of doubly charmed *B* meson decays with the Belle detector

Eric M. Heenan

Submitted in fulfilment of the requirements

of the degree of Doctor of Philosophy

The School of Physics

The University of Melbourne

September 2002

Abstract

An investigation of the doubly charmed B meson decay modes $B^0 \to D^0 D^{*-} K^+$, $B^0 \to D^{*0} D^{*-} K^+$, $B^+ \to D^{*+} D^{*-} K^+$ and $B^0 \to D^{*+} D^{*-} K_S$ is presented. This analysis is performed on a sample of 84.97 million $B\bar{B}$ pairs, produced at the $\Upsilon(4S)$ resonance by the KEKB accelerator, which was collected by the Belle detector.

An analysis of $B^0 \to D^{*+} D^{*-} K_S$ decays can be used to measure time dependent *CP* asymmetry in the neutral B meson system, and constrain the parameters of the Unitarity Triangle. In addition to increasing the precision of the current measurement of $\sin(2\phi_1)$, such an analysis would also remove any $\phi_1 \to \pi/2 - \phi_1$ ambiguity as it can also be used to measure $\cos(2\phi_1)$.

Theoretical predictions of $B \to D^{(*)} \bar{D}^{(*)} K$ branching ratios imply that intermediate broad charm resonances dominate the decay amplitudes. An analysis of these modes can also be used to constrain the strong coupling constants g and h which appear in the effective Lagrangian describing the interaction of heavy mesons with light pseudoscalars.

The $D^0 D^{*-} K^+$, $D^{*+} D^{*-} K^+$ and $D^{*+} D^{*-} K_S$ final states are assembled using a full reconstruction technique. This method allows for a partial reconstruction of the $D^{*0} D^{*-} K^+$ final state. Branching ratios for three of these modes are determined:

$$\begin{aligned} \mathcal{B}(B^0 \to D^0 D^{*-} K^+) &= (1.66 \pm 0.33 \pm 0.35) \times 10^{-3}, \\ \mathcal{B}(B^0 \to D^{*0} D^{*-} K^+) &= (8.17 \pm 0.80 \pm 1.88) \times 10^{-3}, \\ \mathcal{B}(B^0 \to D^{*+} D^{*-} K^0) &= (7.05 \pm 2.03 \pm 1.97) \times 10^{-3}, \end{aligned}$$

and an upper limit of

$$\mathcal{B}(B^+ \to D^{*+} D^{*-} K^+) < 1.6 \times 10^{-3},$$

is placed at a 90% confidence level.

A preliminary Dalitz analysis of the three body $D^0 D^{*-} K^+$ final state is performed, but no definitive evidence for intermediate hadronic resonances is found.

This is to certify that

i. this thesis comprises only my original work towards my PhD,

ii. due acknowledgement has been made of all other material used,

iii. this thesis is less than 100,000 words in length, exclusive of tables, bibliographies and appendices.

Eric M. Heenan

Acknowledgements

I owe a great debt of gratitude to my parents, Eric and Elizabeth Heenan, whose unfailing love and support have made this possible. This thesis is dedicated to them, and to my grandparents.

My thanks are extended to Masashi Hazumi, Geoff Taylor, and my supervisor Martin Sevior, who have each provided me with insight and guidance during this research. The large scale collaborative nature of High Energy Physics makes it impossible to mention all those who have contributed in one way or another to the successful running of the experiment. I would like to thank all members of the Belle and KEKB collaborations who have worked tirelessly on the Belle experiment. I have had many fruitful discussions with Andrzej Bozek, Tim Gershon, Glenn Moloney, and Bruce Yabsley. Each of them has devoted more of their time to answering my questions than they ever had to, and they have my thanks.

My many and frequent trips to Tsukuba were lively, thanks in no small part to Leon Moffitt. His exuberance was often relied upon. I could never have made it this far without all of my friends, who are too numerous to mention here. But you know who you are.

Contents

List of Figures

List of Tables

Chapter 1

Introduction

> "In any subject which has principles, causes, and elements, scientific knowledge and understanding stems from a grasp of these, for we think we know a thing only when we have grasped its first causes and principles and have traced it back to its elements. It obviously follows that if we are to gain scientific knowledge of nature as well, we should begin by trying to decide about its principles."[1]

Written over twenty three hundred years ago, this idea, that we can best understand the world around us by understanding it at its most fundamental level, is still the underpinning philosophy of the study of physics. We are closer to this understanding than we have been at any point in our history. Yet there are still many gaps in our knowledge, and irreconcilable inconsistencies in our theories which require effort to resolve. Some of the tasks that lie ahead are large – such as the search for a grand unified theory of all the forces, and some are small. Yet the devil has been in the details before.

What might be the next modern day solution to the ultraviolet catastrophe, a problem whose solution led to the development of the quantum theory and forever changed our perception of nature? At the dawn of this century, when the biological revolution is gathering speed, many physicists wish the landscape would be shook asunder once more, lest the great era of physics be relegated to the past, and allow the new century to be marked by the ascension of the biologist.

The quest for the new "New Physics" is earnest. Searches for the Higgs boson, Supersymmetry, and Standard Model violating effects are often justified by the statement that their discovery would open up fields for new study. Mechanisms within the Standard Model, such as the phenomenology of *CP* violation and the formalism for heavy quark physics are also far from completely understood. Do the current theories accurately reflect the true nature of the Universe?

A troubled Dane once remarked,

[1] *Physics*, see [1]

"There are more things in Heaven and earth, Horatio,
Than are dreamt of in your philosophy."[2]

And so in this spirit we search in increasingly remote regions of our theory, hoping perversely that the Prince might be right.

P.A.M. Dirac famously observed that above all else one must "have beauty in one's equations." The Standard Model, unifying the electromagnetic, weak and strong forces, is certainly beautiful, and represents the culmination of thousands of years of philosophy and empirical study. And yet it is flawed - it is only a model, not a complete theory, and does not explain the origins of the particles and fields it describes. Some of the symmetries which were held dear fell by the wayside when they were variously found to be broken as experiments further probed our understanding. First the symmetric nature of the laws of physics under a transformation of parity, and then also charge conjugation. But at least the combination of the two was still invariant... that is until this symmetry too was found to be violated in the kaon sector.

The mechanism of *CP* violation represents an area of physics that has not been thoroughly studied, due primarily to its rare occurrence in nature. While the work of Kobayashi and Maskawa provides a formalism for it within the Standard Model, no comprehensive test of this has been completed. However, with the B–factories at KEK and SLAC commencing operation in the last three years this area of the Standard Model is now being thoroughly probed. Is the Kobayashi–Maskawa mechanism for *CP* violation enough to account for its observed rate? Can *CP* violation, core to Sakharov's conditions for baryon asymmetry [2], help solve the mystery of the matter–antimatter imbalance in the universe today?

The decay of neutral B mesons to the final state $J/\psi\, K_S$ provides the cleanest and easiest means to measure *CP* asymmetry in the heavy quark sector. To a large extent the B–factories were designed to maximise the chance of measuring these modes. However, there are many other B meson decays which can be used to probe the mechanism for *CP* violation within the Standard Model. One such mode is $B^0 \to D^{*+}D^{*-}K_S$, which has not yet been studied due to the difficulties in reconstructing events with so many final state particles. However, the large numbers of B meson events created at KEKB provides a perfect avenue to begin such an investigation.

These decay modes can also be used to probe inconsistencies between the number of charmed hadrons per B meson decay and the inclusive semileptonic branching ratio. If these doubly charmed decay modes form a substantial portion of the B meson branching fractions, as theoretically predicted, then this dilemma could in large part be resolved. Again, it is mainly because of the difficulty in reconstructing decay modes with relatively little momentum to distribute to the final state particles that these decays have not yet been comprehensively studied.

This thesis concentrates on the most promising doubly charmed decay modes. As mentioned, the mode $B^0 \to D^{*+}D^{*-}K_S$ can be used to measure time dependent *CP* asymmetries. Measurements of the

[2] Hamlet: Act I, Scene V

branching ratios for the decays $B^0 \to D^0 D^{*-} K^+$ and $B^0 \to D^{*0} D^{*-} K^+$ are a good first step towards determining the inclusive branching ratio for $B \to D^{(*)} \bar{D}^{(*)} K$. These modes can also be used to search for broad intermediate charm resonances which are predicted to dominate their decay amplitudes.

Chapter 2

On doubly charmed *B* meson decays

2.1 The Standard Model

The Standard Model is a field–theoretic description of the strong and electroweak interactions. It can explain a vast number of results from all areas of particle physics, such as neutrino scattering experiments, hadronic sum rules, weak decays and current algebras.

The Standard Model combines Quantum Chromodynamics with the Weinberg–Salam model. It unifies all known experimental data concerning particle interactions via the gauge group $SU(3) \times SU(2) \times U(1)$. The gauge fields of colour $SU(3)$ are responsible for binding the quarks together, while the gauge fields of $SU(2) \times U(1)$ mediate the electromagnetic and weak interactions.

Altogether there are nineteen free parameters in the theory, suggesting it is not a complete account of particle interactions. There are three coupling constants for the groups in $SU(3) \times SU(2) \times U(1)$, two parameters in the Higgs sector, 6 quark masses. 3 mixing angles and one phase, 3 lepton masses, and the QCD vacuum angle.

Recent results concerning neutrino oscillations [3, 4, 5, 6] suggest that the Standard Model must be extended to include mixing in the lepton sector. There are also many theoretical extensions, such as Supersymmetry, which may soon be shown to provide a clearer explanation of the interactions of the fundamental particles. However, for the purposes of the discussions in this thesis the Minimal Standard Model as described above suffices.

2.1.1 Quarks and leptons

In the Standard Model, the fundamental fermionic constituents of matter are the quarks and the leptons. The Standard Model neither explains the number of quarks and leptons nor predicts any of their properties such as charge and mass.

There is evidence for three types, or families, of leptons: electron (ν_e, e); muon (ν_μ, μ); and tau

(ν_τ, τ). The leptons fall into two classes according to electric charge, the neutral neutrinos ν_e, ν_μ, ν_τ, and the negatively charged e^-, μ^-, τ^-. Neutrinos only interact via the weak interaction. The charged leptons interact both via the weak and the electromagnetic interactions.

Quarks			Leptons		
Flavour	Mass	Charge	Flavour	Mass	Charge
u	1 to 5 MeV	$2e/3$	ν_e	< 3 eV	0
d	3 to 9 MeV	$-e/3$	e	0.5110 MeV	$-e$
c	1.15 to 1.35 GeV	$2e/3$	ν_μ	< 0.19 MeV	0
s	75 to 170 MeV	$-e/3$	μ	105.7 MeV	$-e$
t	174.3 GeV[a]	$2e/3$	ν_τ	< 18.2 MeV	0
b	4.0 to 4.4 GeV	$-e/3$	τ	1777 MeV	$-e$

[a] by direct observation. 168.2 GeV from SM electroweak fit

Table 2.1: Quark and lepton properties (from [7]).

As quarks are believed to be permanently confined entities the definition of quark mass is not as obvious as for the masses of the leptons. The masses of the u, d and s quarks in table 2.1 are estimates of *current quark masses*. The c and b quark masses are estimates made from observation of bound states.

Like the leptons, the quarks fall into two classes according to their electrical charge, but there are no neutral quarks and quark electrical charge is fractional. Quarks engage in strong interactions as a result of their colour charge, as well as via the electroweak interaction.

2.1.2 Electroweak Interactions

In the Weinberg–Salam model [8, 9, 10] the quarks interact with the leptons via the exchange of W and Z vector mesons. The traditional description of electromagnetic and low energy charged weak interactions of fermions is expressed by the Lagrangian

$$\mathscr{L}_{\rm int} = -eA_\mu J^\mu_{\rm em} - \frac{G_F}{\sqrt{2}} J^{\mu\dagger}_{\rm ch} J^{\rm ch}_\mu, \tag{2.1}$$

where $J^\mu_{\rm em}$ is the electromagnetic current and $J^\mu_{\rm ch}$ is the charged weak current. G_F is the Fermi constant.

Charged Current Interactions

The charged hadronic weak current for the first two families of quarks can be written as

$$\begin{aligned} J^\mu_{\rm ch} &= \begin{pmatrix} \bar{u} & \bar{c} \end{pmatrix} \gamma^\mu (1-\gamma_5) \begin{pmatrix} d \\ s \end{pmatrix} \\ &= \bar{u}\gamma^\mu(1-\gamma_5)d + \bar{c}\gamma^\mu(1-\gamma_5)s, \end{aligned} \tag{2.2}$$

where the terms u, c, d, and s, represent the mass eigenstates of the quarks. But since the weak interactions do not respect global $SU(3)$ symmetry, and since the d and s quarks have the same charges, there is nothing to prevent the d and s quarks from mixing within the same $SU(2)$ doublet. That is, the weak eigenstates need not necessarily be equal to the mass eigenstates. One set of eigenstates can be expanded in terms of another, so we can write

$$\begin{pmatrix} d' \\ s' \end{pmatrix}_L = V \begin{pmatrix} d \\ s \end{pmatrix}_L \tag{2.3}$$

where V must be a unitary 2×2 matrix. The mixing is normally parametrised by one mixing angle, such that

$$V = \begin{pmatrix} \cos\theta_C & \sin\theta_C \\ -\sin\theta_C & \cos\theta_C \end{pmatrix}, \tag{2.4}$$

where θ_C is called the Cabibbo mixing angle [11].

Generalised to three families of quarks the full charged current is

$$J^\mu_{\text{ch}} = \begin{pmatrix} \bar{u} & \bar{c} & \bar{t} \end{pmatrix} \gamma^\mu (1-\gamma_5) V \begin{pmatrix} d \\ s \\ b \end{pmatrix}, \tag{2.5}$$

where

$$V = \begin{pmatrix} V_{ud} & V_{us} & V_{ub} \\ V_{cd} & V_{cs} & V_{cb} \\ V_{td} & V_{ts} & V_{tb} \end{pmatrix} \tag{2.6}$$

is a unitary 3×3 matrix. The matrix V of equation 2.6 is called the Cabibbo–Kobayashi–Maskawa (CKM) matrix [12]. For three families of quarks there is the possibility of three Euler angles and six phases in the parameterisation of V. Kobayashi and Maskawa demonstrated that this could be reduced to four parameters by adjusting the relative phases of left–handed quark fields. Traditionally these four mixing angles are parametrised with three angles, $\theta_i,\ i = 1, 2, 3$, and one complex phase δ. Then the matrix V can be expressed as

$$\begin{aligned} V = &\begin{pmatrix} 1 & 0 & 0 \\ 0 & C_2 & S_2 \\ 0 & -S_2 & C_2 \end{pmatrix} \times \begin{pmatrix} C_1 & S_1 & 0 \\ -S_1 & C_1 & 0 \\ 0 & 0 & 1 \end{pmatrix} \\ &\times \begin{pmatrix} 1 & 0 & 0 \\ 0 & 1 & 0 \\ 0 & 0 & e^{i\delta} \end{pmatrix} \times \begin{pmatrix} 1 & 0 & 0 \\ 0 & C_3 & S_3 \\ 0 & -S_3 & C_3 \end{pmatrix} \end{aligned} \tag{2.7}$$

where $C_i = \cos\theta_i$ and $S_i = \sin\theta_i$. Written out explicitly this is:

$$V = \begin{pmatrix} C_1 & S_1C_3 & S_1S_3 \\ -S_1C_2 & C_1C_2C_3 - S_2S_3e^{i\delta} & C_1C_2S_3 + S_2C_3e^{i\delta} \\ S_1S_2 & -C_1S_2C_3 - C_2S_3e^{i\delta} & -C_1S_2S_3 + C_2C_3e^{i\delta} \end{pmatrix}. \tag{2.8}$$

Experimentally, the three mixing angles θ_i are either smaller than or comparable with the Cabibbo angle. In the limit $\theta_2 = \theta_3 = 0$, θ_1 reduces to the Cabibbo angle.

2.1.3 Quantum Chromodynamics

Quantum Chromodynamics (QCD) [13, 14], the $SU(3)$ nonabelian gauge theory of colour charge, provides the best understanding that we currently have of the strong interactions. It describes the strong forces as gauge interactions between quarks and gluons. The quarks are the fermions which carry colour charge, each with field $q_j^{(\alpha)}$ and mass $m^{(\alpha)}$, where $\alpha = u, d, s, \ldots$ represents their flavour and $j = 1, 2, 3$ their colour. The gauge bosons are the gluons, each with the field A_μ^a, where $a = 1, \ldots, 8$ denotes their colour.

QCD is defined by the Lagrangian

$$\mathscr{L}_{\mathrm{QCD}} = -\frac{1}{4}F^a_{\mu\nu}F_a^{\mu\nu} + \sum_\alpha \bar{q}_j^{(\alpha)}(i\not{D}_{jk} - m^{(\alpha)}\delta_{jk})q_k^{(\alpha)}, \tag{2.9}$$

where

$$D_\mu = \partial_\mu + igA_\mu^a T^a \tag{2.10}$$

is the $SU(3)$ colour covariant derivative, and g is the gauge coupling. $F^a_{\mu\nu}$ is the gluon field strength tensor,

$$F^a_{\mu\nu} = \partial_\mu A^a_\nu - \partial_\nu A^a_\mu - gf^{ABC}A^B_\mu A^C_\nu, \tag{2.11}$$

and T^a are the $SU(3)$ group generators in the triplet representation of quarks. The generators obey the commutation relations $[T^A, T^B] = if^{ABC}T^C$, where f^{ABC} are the complete antisymmetric structure constants of $SU(3)$.

The QCD Lagrangian in equation 2.9 has a simple structure but leads to a complex spectrum of hadrons, implies the properties of confinement and asymptotic freedom, and has an approximate chiral symmetry which is spontaneously broken. At long distances QCD confines physical states to colour singlet states called hadrons. Bosonic hadrons are called mesons and fermionic hadrons are called baryons. The simplest way to form mesons and baryons are the combinations of quark fields $\bar{q}^\alpha q_\alpha$ and $\epsilon^{\alpha\beta\gamma}q_\alpha q_\beta q_\gamma$.

Although unproven, it is believed that the QCD coupling grows very large as the energy scale is lowered, leading to the phenomenon of quark confinement. At a scale of $\Lambda_{\mathrm{QCD}} \approx 200\mathrm{MeV}$ QCD becomes strongly coupled so that perturbation theory breaks down and nonperturbative effects become important. Because

the complexity of low energy QCD has so far prevented direct analytic solution of the theory various approximations are often made. The u, d, and s quark masses are small compared with the scale $\Lambda_{\rm QCD}$ of nonperturbative strong interaction physics, so an approximation is often made in which the masses of these *light* quarks are set to zero. The limit $m_q \to 0$ is often known as the chiral limit.

2.1.4 Heavy Quark Physics

The scale $\Lambda_{\rm QCD}$ is much lower than the masses of the *heavy* quarks (t, b, c) (table 2.1). For processes that occur at energies well below these masses it is often appropriate to use an effective theory of the strong interactions where these heavy quarks are integrated out of the theory and no longer occur as explicit degrees of freedom in the Lagrangian.

A colour singlet state, such as a meson made up of a quark–antiquark pair, is bound by the nonperturbative gluon dynamics. If the quarks are light, the typical size of such a system is of the order of $\Lambda_{\rm QCD}^{-1}$. A $Q\bar{q}$ meson containing a heavy quark with mass $m_Q \gg \Lambda_{\rm QCD}$, and a light quark with mass $m_q \ll \Lambda_{\rm QCD}$ is also typically of the size $\Lambda_{\rm QCD}^{-1}$. The typical momentum transfer Δp between the heavy and light quarks in this system arising from nonperturbative QCD dynamics is of the order of $\Lambda_{\rm QCD}$, with the consequence that the velocity v of the heavy quark is almost unchanged in such strong interactions, since $\Delta v = \Delta p / m_Q$.

In the limit $m_Q \to \infty$ the heavy quark in the meson can be modelled with a constant velocity. The heavy quark then acts like a static external source that transforms as a colour triplet, and the dynamics of the system reduces to that of light degrees of freedom[1] interacting with this colour source. Thus in this limit the mass of the heavy quark becomes irrelevant, so that all heavy quarks interact in the same way within heavy mesons, leading to *heavy quark flavour symmetry*. The only strong interactions of the heavy quark are with gluons, and are spin independent, leading to *heavy quark spin symmetry*.

Heavy Quark Effective Theory

The QCD Lagrangian of equation 2.9 does not explicitly contain heavy quark spin–flavour symmetry as $m_Q \to \infty$. It is often useful to use an effective field theory for QCD in which this symmetry is apparent. The effective field theory for hadrons containing a single heavy quark is the Heavy Quark Effective Theory (HQET) [15, 16, 17] which is valid for momenta much smaller than the mass of the heavy quark m_Q. The effective field theory is constructed so that only inverse powers of m_Q appear in the effective Lagrangian. To leading order in $1/m_Q$ the effective Lagrangian is

$$\mathscr{L}_{\rm eff} = \sum_{i=1}^{N_h} \bar{Q}_v^{(i)} (iv \cdot D) Q_v^{(i)}, \tag{2.12}$$

The HQET has been used extensively in analytic and lattice studies of meson spectroscopy.

[1] the light quark and gluons

2.2 *CP* violation in the Standard Model

One of the uncertainties in our understanding of nature as provided by the Standard Model is the mechanism for *CP* violation. A C transformation corresponds to the conjugation of charge, while P transforms the parity of a state, changing left–handed into right–handed states and vice–versa. Physically a *CP* transformation corresponds to the transformation of a left–handed particle into a right–handed antiparticle. The Standard Model is invariant under the combined action of C, P, and the third transformation of time reversal, T. This is because all quantum field theories obey *CPT* symmetry under very general conditions [18, 19, 20, 21].

It was long thought that the laws of physics were invariant under the individual operations of C, P and T. Lee and Yang [22] questioned this assumption and later had their work confirmed when experiments demonstrated P and C violation in weak decays of nuclei [23] and pions and muons [24, 25]. However *CP* symmetry was still believed to be in good shape.

By this stage neutral strange mesons had been discovered, and it was known that since they had non–zero strangeness they could not be their own antiparticle, unlike the π^0. Therefore two neutral kaons had to exist, the K^0 and $\bar{K}^0$, differing by two units of strangeness. But how then to tell them apart? Gell-Mann and Pais [26] analysed this problem, assuming *CP* invariance. A consequence of their argument was that the observed neutral kaons, the K_1 and its antiparticle the K_2, were a mixture of two strangeness eigenstates, the K^0 and $\bar{K}^0$, produced in strong interactions. If the weak interaction was *CP* invariant then the observed particles should be eigenstates of *CP*, such that

$$\begin{aligned} CP\,|K_1\rangle &= CP\left[\frac{1}{\sqrt{2}}\left(\left|K^0\right\rangle + \left|\bar{K}^0\right\rangle\right)\right] \\ &= \frac{1}{\sqrt{2}}\left(\left|\bar{K}^0\right\rangle + \left|K^0\right\rangle\right) = K_1 \end{aligned} \tag{2.13}$$

$$\begin{aligned} CP\,|K_2\rangle &= CP\left[\frac{1}{\sqrt{2}}\left(\left|K^0\right\rangle - \left|\bar{K}^0\right\rangle\right)\right] \\ &= \frac{1}{\sqrt{2}}\left(\left|\bar{K}^0\right\rangle - \left|K^0\right\rangle\right) = -K_2 \end{aligned} \tag{2.14}$$

Since $CP\,|\pi^+\pi^-\rangle = |\pi^+\pi^-\rangle$, equations 2.13 and 2.14 would imply that the decay to the final state $\pi^+\pi^-$ is allowed for the K_1, but is forbidden for the K_2 meson if *CP* symmetry holds. This explained the longer lifetime of the K_2.

However, in 1964 Christenson et al. [27] reported $\mathcal{B}(K_2^0 \to \pi^+\pi^-) = (2.0 \pm 0.4) \times 10^{-3}$, indicating that the two observed neutral kaons were not *CP* eigenstates. Since it was now known that the observed long lived neutral kaon was not the *CP* eigenstate K_2 it became known as the K_L meson. Similarly the short lived state is referred to as the K_S meson.

2.2.1 The Kobayashi–Maskawa implementation of *CP* violation

After *CP* violation was discovered theorists scrambled to provide an explanation for it. However, it was not realised for some time that *CP* violation cannot arise from charged current interactions between only the u, d, and s quarks. Extending the model to include the existence of charm quarks, which were hypothesised by Glashow, Illiopollous and Maiani (GIM) in order to rule out strangeness changing neutral currents [28], still did not accommodate a mechanism for *CP* violation as observed, since the phases of the quark mass matrices and V (equation 2.4) could be rotated away by redefining the phases of the quark fields.

Kobayashi and Maskawa [12] expanded the quark model to three generations, so that the charged weak current takes the form of equation 2.5. The CKM matrix of equation 2.6 contains one phase, δ, which cannot be rotated away. This is significant, since the the Lagrangian of equation 2.1 is only *CP* symmetric if all the coupling parameters are real. Thus a non zero complex phase, δ, in V provides a mechanism for *CP* violation within the Standard Model. If the phase is zero then *CP* symmetry would be conserved in electroweak interactions.

There are any number of ways to express the CKM matrix in terms of three rotation angles and one phase. The matrix can also be parameterised such that the phase appears in any element so desired. However, various representations are better at exposing the underlying physics than others, although of course the physics remains the same for all. The parameterisation chosen by the Particle Data Group was shown in equation 2.8. Another parameterisation, which offers a somewhat intuitive description of *CP* violation and quark mixing, was suggested by Wolfenstein [29]. In it, the CKM matrix is expressed through an expansion in powers of $\sin\theta_C = \lambda$, such that

$$V = \begin{pmatrix} 1-\frac{1}{2}\lambda^2 & \lambda & A\lambda^3(\rho - i\eta + \frac{i}{2}\eta\lambda^2) \\ -\lambda & 1-\frac{1}{2}\lambda^2 - i\eta A^2\lambda^4 & A\lambda^2(1+i\eta\lambda^2) \\ A\lambda^3(1-\rho-i\eta) & -A\lambda^2 & 1 \end{pmatrix}. \tag{2.15}$$

The three Euler angles and one phase of equation 2.8 are replaced by the four real quantities $\lambda,\ A,\ \rho$ and η, where $|\lambda|$, $|A|$, and $|\rho|$ are of the order of unity. This parameterisation neatly illustrates that V is almost diagonal and symmetric, and its elements get smaller the further away from the diagonal they are.

2.2.2 The Unitarity Triangle

The unitarity of the CKM matrix imposes constraints upon its elements. Most notably,

$$\begin{array}{ccccc} V_{ud}^* V_{us} + & V_{cd}^* V_{cs} + & V_{td}^* V_{ts} & = 0 \\ \mathcal{O}(\lambda) & \mathcal{O}(\lambda) & \mathcal{O}(\lambda^5) \end{array} \tag{2.16}$$

$$\begin{array}{lll} V_{ud}V_{cd}^* + & V_{us}V_{cs}^* + & V_{ub}V_{cb}^* \\ \mathcal{O}(\lambda) & \mathcal{O}(\lambda) & \mathcal{O}(\lambda^5) \end{array} = 0 \tag{2.17}$$

$$\begin{array}{lll} V_{us}^*V_{ub} + & V_{cs}^*V_{cb} + & V_{td}^*V_{tb} \\ \mathcal{O}(\lambda^4) & \mathcal{O}(\lambda^2) & \mathcal{O}(\lambda^2) \end{array} = 0 \tag{2.18}$$

$$\begin{array}{lll} V_{ud}V_{ub}^* + & V_{cd}V_{cb}^* + & V_{td}V_{tb}^* \\ \mathcal{O}(\lambda^3) & \mathcal{O}(\lambda^3) & \mathcal{O}(\lambda^3) \end{array} = 0 \tag{2.19}$$

These relations each require that the sum of three complex quantities is zero, so they may also be thought of as triangles in the complex plane. These relations define what are known as the *unitarity triangles*. Characterising these using the parameterisation of equation 2.15 it is apparent that the first two triangles described by equations 2.16 and 2.17 are extremely squashed, two sides are of order λ, the third one is of order λ^5. These equations describe strange and charm decays. The third triangle is still squashed, but less so, two sides are of order λ^2 and, the third is of order λ^4.

Drawing the triangles described by equations 2.16 to 2.18 using experimentally measured values of V_{ij} confirms that for the first two triangles one side is much shorter than the others, and thus the triangles collapse into a line. This intuitively explains why *CP* violation is small in the leading K meson decays (the first triangle) and the leading B_s meson decays (the third triangle).

The fourth triangle, described by equation 2.19, is known as the *Unitarity Triangle*. It is shown in figure 2.1(a). The openness of this triangle points to large *CP* violating effects in B_d decays. The triangle

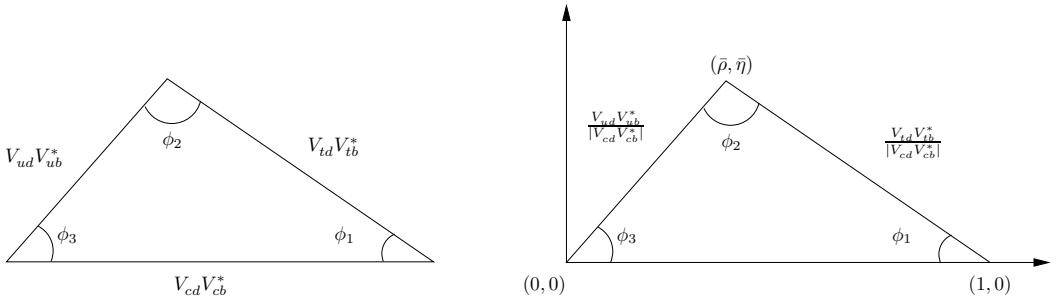

(a) The angles of the Unitarity Triangle are related to the CKM parameters.

(b) The rescaled Unitarity Triangle, all sides divided by $V_{cb}^*V_{cd}$.

Figure 2.1: The Unitarity Triangle.

in figure 2.1(b) is constructed by choosing a phase convention such that $(V_{cd}V_{cb}^*)$ is real, and then rescaling the triangle by dividing all sides by $|V_{cd}V_{cb}^*|$. The triangle then has coordinates $(0,0)$, $(1,0)$ and $(\bar{\rho},\bar{\eta})$,

where

$$\bar{\rho} \cong (1 - \frac{\lambda^2}{2})\rho, \qquad \bar{\eta} \cong (1 - \frac{\lambda^2}{2})\eta. \tag{2.20}$$

The angles of the Unitarity Triangle are denoted as ϕ_1, ϕ_2 and ϕ_3:

$$\phi_1 \equiv \arg\left[-\frac{V_{cd}V_{cb}^*}{V_{td}V_{tb}^*}\right]; \qquad \phi_2 \equiv \arg\left[-\frac{V_{td}V_{tb}^*}{V_{ud}V_{ub}^*}\right]; \qquad \phi_3 \equiv \arg\left[-\frac{V_{ud}V_{ub}^*}{V_{cd}V_{cb}^*}\right]. \tag{2.21}$$

These angles are real quantities which may be measured via *CP* asymmetries in B decays. They are also commonly referred to as β, α and γ respectively.

2.3 Some fundamentals of *B* physics

CP violation was first detected in the neutral kaon system, where the *CP* violating effects were attributable solely to dilution of the *CP* eigenstates of equations 2.13 and 2.14, as discussed in §2.2. In 1980, Sanda and Carter [30, 31, 32] showed that the Kobayashi–Maskawa (KM) model indicated the possibility of sizable *CP* violation in the neutral B meson system. When first the MAC [33], and then the MARKII [34] collaborations discovered an unusually long beauty lifetime, followed by the measurement of significant $B^0 - \bar{B}^0$ oscillations by the ARGUS collaboration [35], hopes of detecting significant *CP* violation in the B meson decays were increased.

Although *CP* violation can occur in the mixing of B^0 and $\bar{B}^0$ mesons, as in the neutral kaon system, this is not the dominant method through which the KM phase is exhibited in the B sector. Rather, sizable *CP* asymmetries are expected through the interference between decays of B^0 and $\bar{B}^0$ mesons to the same final state with and without mixing, a process which is known as *indirect CP* violation. Further, different magnitudes for the amplitudes for a decay and its *CP* conjugate process would be evidence for *direct CP* violation.

2.3.1 Mixing and time evolution of neutral *B* mesons

The flavour eigenstates for the B_d system are $B^0 = \bar{b}d$ and $\bar{B}^0 = b\bar{d}$. These states mix according to the

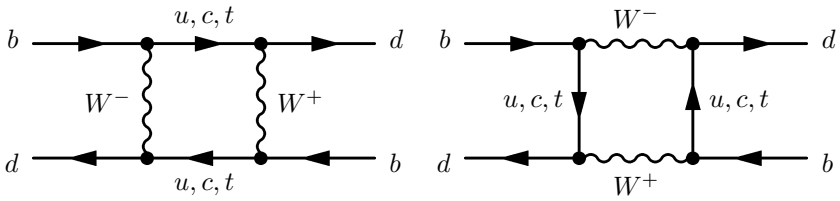

Figure 2.2: Box diagrams describing B^0– $\bar{B}^0$ mixing.

Feynman diagrams of figure 2.2. These mixing diagrams are commonly known as box diagrams due to

their distinctive shape. An initial flavour eigenstate of $\left|B^0\right\rangle$ or $\left|\bar{B}^0\right\rangle$ will evolve over time into a state

$$|\Psi(t)\rangle = a(t)\left|B^0\right\rangle + b(t)\left|\bar{B}^0\right\rangle, \tag{2.22}$$

as governed by the time dependent Schrödinger equation

$$i\frac{\partial}{\partial t}\begin{pmatrix} a(t) \\ b(t) \end{pmatrix} = \left(\mathbf{M} - \frac{i}{2}\mathbf{\Gamma}\right)\begin{pmatrix} a(t) \\ b(t) \end{pmatrix}, \tag{2.23}$$

where $\mathbf{M}$ and $\mathbf{\Gamma}$ are the Hermitian mass and decay matrices respectively. *CPT* invariance guarantees

$$\Gamma_{11} = \Gamma_{22} \equiv \Gamma \tag{2.24}$$

which is the decay width of the B^0 and $\bar{B}^0$ flavour eigenstates, and

$$M_{11} = M_{22} \equiv M. \tag{2.25}$$

The off–diagonal elements of $\mathbf{M}$ and $\mathbf{\Gamma}$ arise from the box diagrams of figure 2.2, and play an important role in *CP* violation.

The neutral B meson system is like the neutral kaon system, in that two *CP*-conjugate states exist. The mass eigenstates are not *CP* eigenstates, but are mixtures of the two *CP*-conjugate quark states. The two mass eigenstates can be written

$$\begin{aligned} |B_L\rangle &= p\left|B^0\right\rangle + q\left|\bar{B}^0\right\rangle, \\ |B_H\rangle &= p\left|B^0\right\rangle - q\left|\bar{B}^0\right\rangle \end{aligned} \tag{2.26}$$

where the H and L stand for heavy and light respectively, as the two states have nearly equal predicted widths (and thus lifetimes), but significantly different masses. These are denoted $\Delta m \equiv m_H - m_L$ and $\Delta\Gamma \equiv \Gamma_H - \Gamma_L \simeq 0$. *CPT* invariance requires

$$\left|\frac{q}{p}\right|^2 = \left|\frac{M_{12}^* - \frac{i}{2}\Gamma_{12}^*}{M_{12} - \frac{i}{2}\Gamma_{12}}\right| \tag{2.27}$$

$$= 1 + \left|\frac{\Gamma_{12}}{M_{12}}\right|\sin\Delta\varphi + \mathcal{O}\left(\left|\frac{\Gamma_{12}}{M_{12}}\right|^2\right), \tag{2.28}$$

where

$$\Delta\varphi = \arg(M_{12}) - \arg(\Gamma_{12}) = -\arg\left(\frac{\Gamma_{12}}{M_{12}}\right) \tag{2.29}$$

is the phase difference between M_{12} and Γ_{12}.

The time evolution of a state that begins at $t = 0$ as either a B^0 or $\bar{B}^0$ is given by

$$\begin{aligned} \left|B^0(t)\right\rangle &= g_+(t)\left|B^0\right\rangle + \frac{q}{p} g_-(t)\left|\bar{B}^0\right\rangle, \text{ or} \\ \left|\bar{B}^0(t)\right\rangle &= \frac{p}{q} g_-(t)\left|B^0\right\rangle + g_+(t)\left|\bar{B}^0\right\rangle, \end{aligned} \tag{2.30}$$

where

$$\begin{aligned} g_+(t) &= e^{-iMt} e^{-\Gamma t/2} \cos(\Delta m t/2), \text{ and} \\ g_-(t) &= e^{-iMt} e^{-\Gamma t/2} i \sin(\Delta m t/2) \end{aligned} \tag{2.31}$$

as governed by equation 2.23.

2.3.2 *CP* violation in the *B* meson system

If *CP* symmetry was conserved then the *CP* eigenstates of the neutral B mesons would be the same as the mass eigenstates given by equation 2.26. In this case the relative phase between M_{12} and Γ_{12} vanishes, and equation 2.27 becomes equal to one. Therefore, $|q/p| \neq 1$ would imply *CP* violation in the mixing of B^0 and $\bar{B}^0$ mesons, similar to the neutral kaon system.

In the neutral B meson system the t quark contribution dominates the box diagrams of figure 2.2 since $m_t \gg m_c$ and m_u, which implies that $|\Gamma_{12}| \ll |M_{12}|$, such that

$$1 - \left|\frac{q}{p}\right|^2 \simeq \mathcal{O}(10^{-3}). \tag{2.32}$$

Hence, *CP* violation in $B^0 - \bar{B}^0$ mixing is expected to be quite small, as in the case of the neutral kaon system. Nonetheless, there are other mechanisms by which *CP* symmetry can be significantly broken in B meson decays.

Direct *CP* violation

In the absence of mixing, *CP* symmetry can still be violated in B meson decays. If the amplitude for a decay to a final state f is given by $\mathcal{A}_f$, and its *CP* conjugate is $\bar{\mathcal{A}}_{\bar{f}}$, then their ratio, $\left|\frac{\bar{\mathcal{A}}_{\bar{f}}}{\mathcal{A}_f}\right|$ is independent of any phase conventions. Complex parameters in a Lagrangian term that contribute to the amplitude $\mathcal{A}_f$ will appear as their complex conjugate in $\bar{\mathcal{A}}_{\bar{f}}$. In the Standard Model these phases only occur in the CKM matrix, and are often called *weak* phases.

Alternatively, a phase can appear in the scattering or decay amplitudes even if the Lagrangian is real. These phases do not violate *CP* since they appear in $\mathcal{A}_f$ and $\bar{\mathcal{A}}_{\bar{f}}$ with the same sign, and are usually referred to as *strong* phases since the rescattering is normally due to strong interactions.

Therefore it is useful to write each contribution to $\mathcal{A}$ in three parts: its magnitude $\mathcal{A}_i$; the weak phase

$e^{i\phi_i}$; and the strong phase term $e^{i\delta_i}$. The total amplitude for a decay, $\mathcal{A}_f$, is the sum of all possible processes that may contribute. If there is only one possible decay mechanism then no information may be determined about the complex phase. However, if several processes contribute, then the amplitude and its conjugate are given by

$$\mathcal{A}_f = \sum_i \mathcal{A}_i e^{i(\delta_i+\phi_i)}, \text{ and} \tag{2.33}$$

$$\bar{\mathcal{A}}_{\bar{f}} = e^{2i(\xi_f-\xi_B)} \sum_i \mathcal{A}_i e^{i(\delta_i-\phi_i)}, \tag{2.34}$$

where ξ_f and ξ_B are convention dependent phases. The ratio of the amplitude and its conjugate, which is convention independent is given by

$$\left|\frac{\bar{\mathcal{A}}_{\bar{f}}}{\mathcal{A}_f}\right| = \left|\frac{\sum_i \mathcal{A}_i e^{i(\delta_i-\phi_i)}}{\sum_i \mathcal{A}_i e^{i(\delta_i+\phi_i)}}\right|. \tag{2.35}$$

When *CP* is conserved the weak phases ϕ_i are equal, and so the ratio of equation 2.35 must be one. Any deviation from this is an indication of *CP* violation. This type of *CP* violation will not occur unless there are at least two contributions to the amplitude with different weak phases that have different strong phases, since

$$|\mathcal{A}|^2 - |\bar{\mathcal{A}}|^2 = -2\sum_{i,j} \mathcal{A}_i\mathcal{A}_j \sin(\phi_i-\phi_j)\sin(\delta_i-\delta_j). \tag{2.36}$$

Since charged B mesons cannot mix, *CP* violation in B^+ and B^- meson decays would have to occur via this mechanism if they are to be described within the Standard Model. The existence of direct *CP* violation in the neutral kaon system was confirmed in 1999 by the KTeV [36] and NA48 [37] collaborations.

Indirect *CP* violation

The term *indirect CP* violation usually refers to all mechanisms by which *CP* symmetry is broken that involve mixing between B^0 and $\bar{B}^0$ mesons. As discussed earlier, *CP* violation purely from mixing is quite small in the B sector. However, *CP* violation in the interference between decays with and without mixing has long been regarded as the most promising means of measuring *CP* violation in B meson decays. It can be observed by comparing decays to a final *CP* eigenstate of a neutral B state that began at time $t = 0$ as a B^0 to those of a state that began as a $\bar{B}^0$. The time dependent *CP* asymmetry can be defined as

$$a_{CP}(t) = \frac{\Gamma(B^0(t) \to f_{CP}) - \Gamma(\bar{B}^0(t) \to f_{CP})}{\Gamma(B^0(t) \to f_{CP}) + \Gamma(\bar{B}^0(t) \to f_{CP})}, \tag{2.37}$$

where f_{CP} is the *CP* eigenstate. For this asymmetry to be non zero the mixing weak phase in q/p must be different to the weak decay phase in $\bar{\mathcal{A}}_{f_{CP}}/\mathcal{A}_{f_{CP}}$, where

$$\mathcal{A}_{f_{CP}} \equiv \left\langle f_{CP}|B^0\right\rangle, \text{ and } \bar{\mathcal{A}}_{f_{CP}} \equiv \left\langle f_{CP}|\bar{B}^0\right\rangle. \tag{2.38}$$

These time dependent *CP* asymmetries are measured by producing coherent pairs of B mesons, and looking for events where one B decays to a final *CP* eigenstate f_{CP} at time t_{CP}, while the second decays to a *tagging* mode, $f_{\rm tag}$, that identifies its flavour at time $t_{\rm tag}$. For instance, if one B particle is tagged as a $\bar{B}^0$ through its decay at time $t_{\rm tag}$, then the other B particle must be a B^0 at time $t_{\rm tag}$, and it will continue to oscillate until t_{CP}. The flavour of the second B when it decays at t_{CP} to the *CP* eigenstate f_{CP} can be deduced according to equation 2.30. The second particle's flavour can be worked out this way even if $t_{CP} < t_{\rm tag}$. In this case the state of the second B at time t_{CP} must be just the right mixture such that it would have evolved to be a B^0 at time $t_{\rm tag}$.

The time dependent decay rates of the processes in equation 2.37 can be evaluated using the time evolution formalism described in §2.3.1. Assuming that *CP* violation purely in mixing is insignificant, so that $|q/p| = 1$ and $\Delta\Gamma = 0$ the amplitudes can be shown to be

$$\begin{aligned}
\Gamma(B^0(t) \to f_{CP}) &= \left|\left\langle f_{CP}|B^0(t)\right\rangle\right|^2 \\
&= e^{-\Gamma t}\cos^2\left(\frac{\Delta m t}{2}\right)|\mathcal{A}_{f_{CP}}|^2 + e^{-\Gamma t}\sin^2\left(\frac{\Delta m t}{2}\right)|\bar{\mathcal{A}}_{f_{CP}}|^2 \\
&\quad - e^{-\Gamma t}\sin(\Delta m t)\mathrm{Im}\left[\left(\frac{q}{p}\right)^* \mathcal{A}_{f_{CP}}\bar{\mathcal{A}}^*_{f_{CP}}\right], \text{ and}
\end{aligned} \tag{2.39}$$

$$\begin{aligned}
\Gamma(\bar{B}^0(t) \to f_{CP}) &= \left|\left\langle f_{CP}|\bar{B}^0(t)\right\rangle\right|^2 \\
&= e^{-\Gamma t}\cos^2\left(\frac{\Delta m t}{2}\right)|\bar{\mathcal{A}}_{f_{CP}}|^2 + e^{-\Gamma t}\sin^2\left(\frac{\Delta m t}{2}\right)|\mathcal{A}_{f_{CP}}|^2 \\
&\quad - e^{-\Gamma t}\sin(\Delta m t)\mathrm{Im}\left[\left(\frac{q}{p}\right)^* \mathcal{A}_{f_{CP}}\bar{\mathcal{A}}^*_{f_{CP}}\right].
\end{aligned} \tag{2.40}$$

By introducing the product

$$\lambda_{f_{CP}} \equiv \frac{q}{p}\cdot\frac{\bar{\mathcal{A}}_{f_{CP}}}{\mathcal{A}_{f_{CP}}} = \eta_{f_{CP}}\frac{q}{p}\cdot\frac{\bar{\mathcal{A}}_{\bar{f}_{CP}}}{\mathcal{A}_{f_{CP}}}, \tag{2.41}$$

which is independent of phase conventions, the asymmetry defined in equation 2.37 can be expressed as

$$a_{CP}(t) = \frac{\left|\left\langle f_{CP}|B^0(t)\right\rangle\right|^2 - \left|\left\langle f_{CP}|\bar{B}^0(t)\right\rangle\right|^2}{\left|\left\langle f_{CP}|B^0(t)\right\rangle\right|^2 + \left|\left\langle f_{CP}|\bar{B}^0(t)\right\rangle\right|^2} \tag{2.42}$$

$$= \frac{(1-|\lambda_{f_{CP}}|^2)\cos(\Delta m t) - 2\mathrm{Im}(\lambda_{f_{CP}})\sin(\Delta m t)}{1+|\lambda_{f_{CP}}|^2} \tag{2.43}$$

where $\eta_{f_{CP}}$ is the *CP* eigenvalue of f_{CP}. Thus *CP* asymmetry occurs if $\mathrm{Im}(\lambda_{f_{CP}}) \neq 0$, ie. if the mixing weak phase is different from the weak decay phase, as mentioned earlier.

However, *CP* violation can also occur if $|\lambda_{f_{CP}}|^2 \neq 1$. Since $|q/p| \simeq 1$, this can only occur if the size of the decay amplitudes are different. This is essentially direct *CP* violation, as it occurs without any reference to $B^0 - \bar{B}^0$ mixing. However, *CP* violation can also occur if there are multiple processes with different weak decay phases contributing to the amplitude. This can generally be quite complicated to express, but the product $|\lambda_{f_{CP}}| \cong 1$ for decays to a *CP* eigenstate which are dominated by a single amplitude, so that equations 2.39, 2.40 and 2.43 simplify to

$$\Gamma(B^0(t) \to f_{CP}) = e^{-\Gamma t}|\mathcal{A}_{f_{CP}}|^2[1 - \mathrm{Im}(\lambda_{f_{CP}})\sin(\Delta m t)], \quad (2.44)$$

$$\Gamma(\bar{B}^0(t) \to f_{CP}) = e^{-\Gamma t}|\mathcal{A}_{f_{CP}}|^2[1 + \mathrm{Im}(\lambda_{f_{CP}})\sin(\Delta m t)], \quad (2.45)$$

$$a_{CP}(t) = -\mathrm{Im}(\lambda_{f_{CP}})\sin(\Delta m t) \quad (2.46)$$

The decay $B^0 \to J/\psi\, K_S$, which occurs via the quark transition $b \to c\bar{c}s$, is the most promising avenue through which to investigate indirect *CP* violation [31, 32]. The dominant process for these decays is the tree diagram of figure 2.3. Contributions from the loop, or *penguin*, diagrams of figure 2.4 are extremely

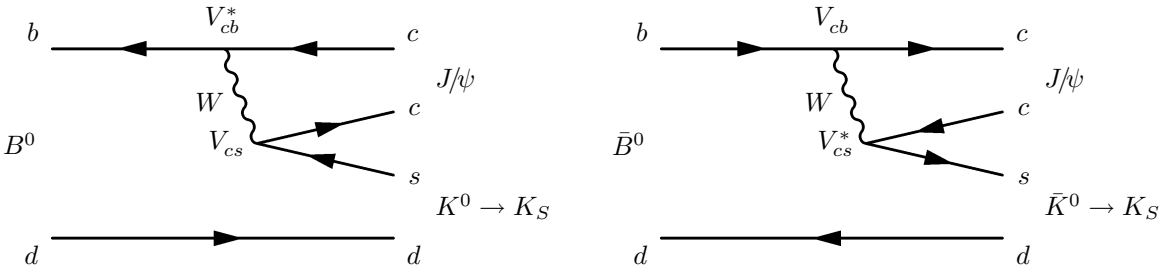

Figure 2.3: Tree diagrams for $B \to J/\psi\, K_S$.

small. Further, the phases of the penguin diagrams are expected to be the same as those of the tree diagrams. Therefore these decays are very unlikely to exhibit direct *CP* violation, and the assumption

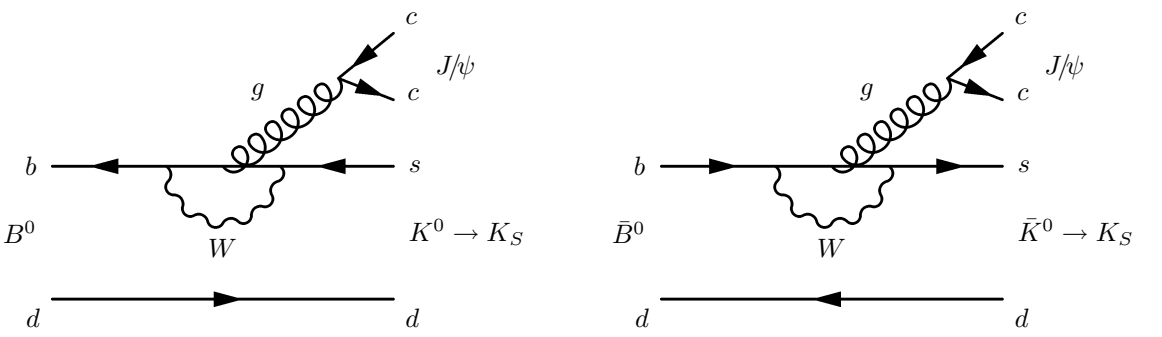

Figure 2.4: Penguin diagrams for $B \to J/\psi\, K_S$.

$$\left|\frac{\bar{\mathcal{A}}_{f_{CP}}}{\mathcal{A}_{f_{CP}}}\right| = 1 \quad (2.47)$$

can be made [38], where the final *CP* eigenstate in this instance is $f_{CP} = J/\psi\, K_S$. The ratio

$$\bar{\rho}(J/\psi\, K_S) \equiv \frac{\bar{\mathcal{A}}_{J/\psi\, K_S}}{\mathcal{A}_{J/\psi\, K_S}} = \frac{V_{cb}V_{cs}^*}{V_{cb}^*V_{cs}} \tag{2.48}$$

can be expressed in terms of the CKM elements. Since the ratio Γ_{12}/M_{12} is found to be of the order of 10^{-2} [39], equation 2.27 can be approximated as

$$\frac{q}{p} \simeq +\sqrt{\frac{M_{12}^*}{M_{12}}} = \frac{V_{tb}^*V_{td}}{V_{tb}V_{td}^*} = e^{-2i\phi_1}, \tag{2.49}$$

where ϕ_1 is one of the angles of the Unitarity Triangle. There is an additional phase to be accounted for, coming from the $K^0 - \bar{K}^0$ mixing amplitude, which is given by

$$\left(\frac{q}{p}\right)_K = \frac{V_{cs}V_{cd}^*}{V_{cs}^*V_{cd}}. \tag{2.50}$$

The $J/\psi\, K_S$ final state is *CP* odd, so $\eta_{J/\psi\, K_S} = -1$. Therefore

$$\begin{aligned} \lambda_{J/\psi\, K_S} &= -\left(\frac{q}{p}\right)\cdot\left(\frac{q}{p}\right)_K \cdot \frac{\bar{\mathcal{A}}_{J/\psi\, K_S}}{\mathcal{A}_{J/\psi\, K_S}} \\ &\simeq -\frac{V_{tb}^*V_{td}}{V_{tb}V_{td}^*}\cdot\frac{V_{cs}V_{cd}^*}{V_{cs}^*V_{cd}}\cdot\frac{V_{cb}V_{cs}^*}{V_{cb}^*V_{cs}} \\ &= -e^{-2i\phi_1}, \end{aligned} \tag{2.51}$$

which leads to

$$\mathrm{Im}(\lambda_{J/\psi\, K_S}) \simeq \sin(2\phi_1), \tag{2.52}$$

and hence a measurement of time dependent *CP* violation in $B^0 \to J/\psi\, K_S$ decays is a direct measurement of $\sin(2\phi_1)$, and constrains the parameters of the Unitarity Triangle. Both the Belle and BABAR collaborations have now measured this parameter very precisely. The latest measurement from Belle is [40]

$$\sin(2\phi_1) = 0.719 \pm 0.074 \pm 0.035, \tag{2.53}$$

and BABAR 's most recent result [41] is

$$\sin(2\phi_1) = 0.741 \pm 0.067 \pm 0.033. \tag{2.54}$$

2.3.3 Measuring *CP* violation at a *B*–factory

A measurement of *CP* violation in the B meson sector requires an analysis of millions of decays. Since the branching ratios of even the most promising decay modes (such as $B^0 \to J/\psi\, K_S$) are of the order of 10^{-4} large numbers of B mesons must be produced in order to measure any *CP* asymmetries precisely.

Furthermore, in order to measure time dependent *CP* violation there must be some means of producing coherent B meson pairs, and measuring the time, t, between their decays. The $\Upsilon(4S)$ mass is just above the production threshold for B mesons, and since it decays to $B\bar{B}$ pairs more than 96% of the time [7], an $e^+\,e^-$ accelerator operating at the $\Upsilon(4S)$ resonance is an ideal source of large numbers of B mesons. Such a facility is often referred to as a B–factory.

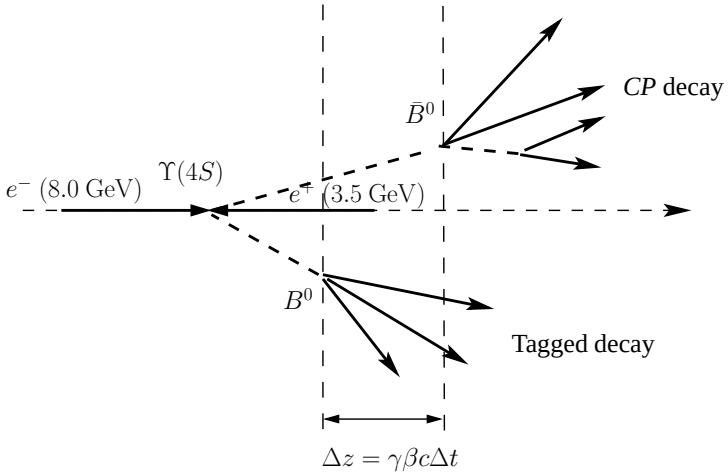

Figure 2.5: Decay of a $B\bar{B}$ pair at an asymmetric B–factory.

As discussed in §2.3.2, time dependent *CP* asymmetries are measured by observing decays of B mesons to a final *CP* eigenstate at some time t_{CP} after they were produced. In a B–factory B mesons are produced in $B\bar{B}$ pairs, which evolve over time as do single B mesons. However, they evolve coherently, so that at any one time there is only one B^0 and one $\bar{B}^0$. Once one of the particles decays, the other continues to evolve, and may later decay with the same flavour as the first.

The aim is to identify events where one of these B mesons decays to a *CP* eigenstate, and the other decays to a state $f_{\rm tag}$ which can be used to *tag* its flavour at time $t_{\rm tag}$. By knowing the flavour of one of the particles at $t_{\rm tag}$ we know the flavour of the other. For instance, if one B meson is *flavour tagged* as a B^0 at $t_{\rm tag}$, then the second must be a $\bar{B}^0$ at $t_{\rm tag}$. Thus the second B meson's flavour when it decays at t_{CP} can be deduced by applying the time evolution formalism to a particle which starts in a $\bar{B}^0$ state at $t_{\rm tag}$ that evolves until t_{CP}.

The proper time, t, in the time dependent *CP* asymmetry of equation 2.37 is then the time interval between the *CP* and tagged decays, such that

$$\Delta t = t_{CP} - t_{\rm tag}. \tag{2.55}$$

It is very difficult to measure this proper time directly. However, if the accelerator is designed to collide electrons and positrons of different energies, the resulting $\Upsilon(4S)$ will be produced with a boost in the lab

frame, as shown in figure 2.5. Then the proper time interval between the B meson decays can be measured as a spatial separation between the B meson decay vertices,

$$\Delta z \equiv z_{CP} - z_{\rm tag} = \gamma\beta c\Delta t. \tag{2.56}$$

This can be achieved by using silicon vertexing detectors which are capable of resolving vertex locations to within tens of microns.

The design of one such B–factory, the KEKB accelerator and the Belle detector, is discussed in the next chapter.

2.4 *CP* violation in doubly charmed *B* meson decays

While the decay $B^0 \to J/\psi\, K_S$ is touted as being the cleanest and easiest way to measure indirect *CP* violation in B meson decays, it is not the only means to do so.

Another such decay is the mode $B^0 \to D^{(*)}\bar{D}^{(*)}$. In this mode the D^+D^- final state is a *CP* eigenstate, but contamination from loop diagrams and final state interactions makes a clean extraction of $\sin(2\phi_1)$ from these decays difficult. The $D^{*+}D^{*-}$ final state is an admixture of *CP* even and odd eigenstates, since states with different angular momenta and hence different parities can contribute. Since the *CP* asymmetry is opposite in sign for the two *CP* states, they tend to cancel each other out, or dilute the asymmetry. The degree of dilution is represented by a dilution factor, D. An angular analysis of the final state can be used to determine the amplitude of each *CP* contribution separately, and hence measure D [42, 43]. However, using the factorisation approximation and HQET it has been shown that the $D^{*+}D^{*-}$ final state is dominated by a single *CP* eigenstate [44, 45, 46]. Furthermore, contamination from final state interactions and penguin contributions is expected to be smaller in this mode than for D^+D^- [43], making a measurement of *CP* violation in the decay $B^0 \to D^{*+}D^{*-}$ simpler.

Similarly, the decays $B^0 \to D^{(*)}\bar{D}^{(*)}K_S$ can be used to measure $\sin(2\phi_1)$, but more significantly they can be used to resolve the $\phi_1 \to \pi/2 - \phi_1$ ambiguity [47, 48, 49] in the *CP* asymmetry by also measuring $\cos(2\phi_1)$. These decays proceed via the quark level process $b \to c\bar{c}s$, similar to $B^0 \to J/\psi\, K_S$, and are theoretically enhanced by a factor of $|V_{cs}/V_{cd}|^2 \sim 20$ relative to $B^0 \to D^{(*)}\bar{D}^{(*)}$. Three body decays to $D^+D^-\pi^0$ and $D^+D^-K_S$ were first analysed by Colangelo et al. [50]. Long distance QCD effects make the theoretical calculation of multi–body hadronic B decays difficult, but by assuming that intermediate hadronic resonances dominated the amplitudes, Colangelo et al. were able to predict a rate for $B \to D^+D^-\pi^0$ and $B \to D^+D^-K_S$. However, as in the D^+D^- case, the $D^+D^-K_S$ final state is more likely to be affected by penguin contributions than the decay $B^0 \to D^{*+}D^{*-}K_S$, making a measurement of *CP* violation more difficult.

Browder et al. [51] considered the possibility of using $B^0 \to D^{*+}D^{*-}K_S$ to measure $\sin(2\phi_1)$ and

$\cos(2\phi_1)$, calculating the decay amplitudes using similiar approximations as [50]. As in the case for $B^0 \to D^{*+}D^{*-}$, the final state for $B^0 \to D^{*+}D^{*-}K_S$ is an admixture of *CP* odd and even states, which will dilute any *CP* asymmetry. Any resonance in the decay further dilutes the *CP* asymmetry, since the resonance would occur in a different kinematical point of the B^0 and $\bar{B}^0$ decay, and hence the amplitudes of the B^0 and $\bar{B}^0$ decays would be different.

Various cuts to remove contamination from intermediate resonances are discussed in [51]. One suggestion is to remove events where the neutral kaon energy, E_k, is less than some critical value, E_{k0}, below which the resonant contributions dominate the decay amplitude. Alternatively, for events where the K_S energy is below E_{k0}, they suggest requiring that the angle, θ, between the K_S and D^{*+} in the $D^{*+}D^{*-}$ rest frame satisfies $-0.5 \leq \cos\theta \leq 0.5$. This removes events where the K_S is close to either the D^{*+} or D^{*-}, which is more likely if the event contains a D^*K_S resonance. However, it is most likely that the selection of cuts to remove any intermediate resonances will be far simpler once these decays have actually been observed. Observation of any intermediate resonances will require a large sample of $B^0 \to D^{*+}D^{*-}K_S$ events, and is currently out of reach for both the SLAC and KEK B–factories. Hopefully both experiments will have accumulated enough events within the next twelve months to perform such an analysis.

Using a formalism similar to that employed in §2.3.2, Browder et al. formulate an expression for the decay rate asymmetry for $B^0 \to D^{*+}D^{*-}K_S$,

$$\frac{\Gamma(t) - \bar{\Gamma}(t)}{\Gamma(t) + \bar{\Gamma}(t)} = D\sin(2\phi_1)\sin(\Delta m t). \tag{2.57}$$

The dilution factor, D, is dependent on the relative contributions of the various amplitudes. The $\cos(2\phi_1)$ term can be investigated through a time integrated analysis of $\Gamma(t) + \bar{\Gamma}(t)$. Approximations for D are made in [51], where the effect of the two cuts previously mentioned is also modelled. It should also be noted that the dilution factor is heavily dependent on the strong coupling constant h, which appears in the effective Lagrangian for the interactions of the heavy mesons with the light pseudoscalars. Various methods of measuring this coupling constant are discussed later in §2.6.

2.5 The charm counting problem

For many years there has been disagreement between theoretical calculations and experimental measurements for fitting both the inclusive semileptonic branching ratio and the number of charmed hadrons per B decay [52, 53, 54, 55, 56, 57, 58, 59],

$$\begin{aligned} n_c &= 1 - \mathcal{B}(b \to \text{no charm}) + \mathcal{B}(b \to c\bar{c}s') \\ &\approx 1 + \mathcal{B}(b \to c\bar{c}s'). \end{aligned} \tag{2.58}$$

The semileptonic branching ratio, $\mathcal{B}_{\rm sl}$, has been measured accurately to be [7]

$$\mathcal{B}(\bar{B} \to X l \nu) = (10.49 \pm 0.17 \pm 0.43)\%, \tag{2.59}$$

and is significantly below the theoretical lower bound of 12.5% set by QCD calculations within the parton model [53]. $\mathcal{B}_{\rm sl}$ and n_c are related since the semileptonic and hadronic widths sum to the total width for B decays,

$$\frac{1}{\tau} = \Gamma = \Gamma_{\rm Semileptonic} + \Gamma_{\rm Hadronic}. \tag{2.60}$$

The hadronic width can be expressed as

$$\Gamma_{\rm Hadronic} = \Gamma(b \to c\bar{c}s) + \Gamma(b \to c\bar{u}d) + \Gamma(b \to sg + \text{no charm}) \tag{2.61}$$

which is constrained by n_c as in equation 2.58. Thus the measured value of n_c [60],

$$n_c = 1.10 \pm 0.06, \tag{2.62}$$

leads to a prediction of the semileptonic branching ratio that is too large.

The measurement of (2.62) was performed by the summation of various exclusive final states, and is hence prone to error. By omitting some final states the result could significantly underestimate the true value. A larger value for $n_{cc} = \mathcal{B}(b \to c\bar{c}s)$, implying a significant number of charmed B meson decay modes were omitted from (2.62), would resolve this discrepancy.

It was thought that the $b \to c\bar{c}s$ transition hadronized predominantly in $\bar{B} \to X_c D_s^{(*)-}$ with the $D_s^{(*)-}$ meson originating from the virtual W. This would mean that most D mesons produced in B decays come from $b \to c\bar{u}d \to DX$ and $b \to c\bar{c}s \to DD_sX$ transitions. However, Buchalla et al. [61] suggested that a significant fraction of D mesons could also arise from $b \to c\bar{c}s$ transitions with light quark pair production at the upper vertex. Using the well measured inclusive semileptonic branching ratio (2.59) they predict

$$\mathcal{B}(b \to c\bar{c}s') = 0.32 \pm 0.05, \tag{2.63}$$

and

$$n_c = 1.30 \pm 0.05. \tag{2.64}$$

Such a large value of $\mathcal{B}(b \to c\bar{c}s')$ would require a significant rate for $\bar{B} \to D\bar{D}\bar{K}X$, and lead Buchalla et al. to predict

i. $\bar{B} \to D^{(*)}\bar{D}^{(*)}\bar{K}$ modes with significant branching ratios,

ii. enhanced $l^+\bar{D}$ and l^-D correlations where the primary lepton originates from one B and the charmed hadron from the other B in the event, and

iii. enhanced DD and $\bar{D}\bar{D}$ correlations at the $\Upsilon(4S) \to B\bar{B}$

The $\bar{B} \to D\bar{D}\bar{K}^* X$ process is unlikely to occur since analysis of the inclusive K^* yields in B meson decays suggests that most K^* mesons in B decays come from intermediate charmed hadrons.

Due to the difficulties in reconstructing modes with such high multiplicity and low Q very little is known experimentally about $B \to D\bar{D}K$ decays. Results of a preliminary study [62] by the CLEO collaboration of the prediction (i) are shown in table 2.2. CLEO also found evidence for these decays by studying wrong sign D–lepton correlations, where they observed $\mathcal{B}(B \to DX) = (7.9 \pm 2.2)\%$ [63].

Mode	Branching fraction
$\mathcal{B}(\bar{B}^0 \to D^{*+}\bar{D}^0 K^-)$	$0.45^{+0.25}_{-0.19} \pm 0.08\%$
$\mathcal{B}(B^- \to D^{*0}\bar{D}^0 K^-)$	$0.54^{+0.33}_{-0.24} \pm 0.12\%$
$\mathcal{B}(\bar{B}^0 \to D^{*+}\bar{D}^{*0} K^-)$	$1.30^{+0.61}_{-0.47} \pm 0.27\%$
$\mathcal{B}(B^- \to D^{*0}\bar{D}^{*0} K^-)$	$1.45^{+0.78}_{-0.58} \pm 0.36\%$

Table 2.2: CLEO results on $B \to DDK$ decays.

Including these measurements in the determination of n_c results in a value of [7]

$$n_{cc} = (23.9 \pm 3.0)\%, \tag{2.65}$$

which is consistent with theoretical calculations [64, 65].

More recently the BABAR [66] and Belle [67] collaborations have also investigated these modes, reporting the preliminary results of table 2.3.

	Mode	Branching fraction
BABAR	$\mathcal{B}(B^0 \to D^{*-}D^0 K^+)$	$0.28 \pm 0.07 \pm 0.05\%$
	$\mathcal{B}(B^0 \to D^{*-}D^{*0} K^+)$	$0.68 \pm 0.17 \pm 0.17\%$
	$\mathcal{B}(B^+ \to D^{*+}D^{*-} K^+)$	$0.34 \pm 0.16 \pm 0.09\%$
Belle	$\mathcal{B}(B^0 \to D^0 D^{*-} K^+)$	$0.32 \pm 0.08 \pm 0.07\%$

Table 2.3: BABAR and Belle results on $B \to DDK$ decays.

While these results have done much to allay the differences between the theoretical predictions and experiment, further measurements of the $B \to D\bar{D}K$ exclusive final states will shed more light on the matter.

2.6 Intermediate resonances

As discussed in §2.4, theoretical calculations of the amplitudes for $B \to D^{(*)}\bar{D}^{(*)}K$ decays show that intermediate hadronic resonances dominate. Many of the predicted contributions are from resonances that

have not yet been experimentally detected. Analyses of the decay widths and Dalitz plots of $D^{(*)}\bar{D}^{(*)}K$ final states could confirm or deny the existence of the many hypothesised intermediate states.

$B \rightarrow D^{(*)}\bar{D}^{(*)}K$ decays can occur through either external or internal $W-$emission processes, as shown in figures 2.6 and 2.7. The $B^0 \rightarrow D^{*-}D^{(*)0}K^+$ decays modes are perhaps the simplest to

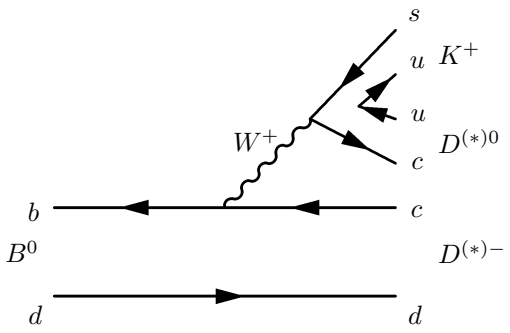

Figure 2.6: External $W-$emission diagram for $B^0 \rightarrow D^{(*)-}D^{(*)0}K^+$ decays

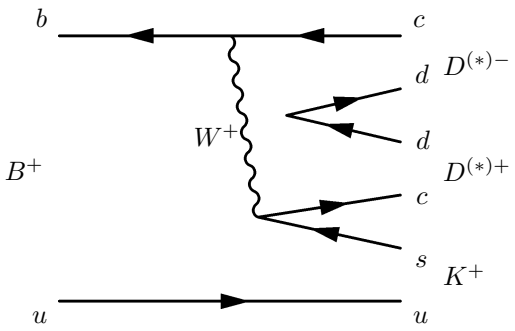

Figure 2.7: Internal $W-$emission diagram for $B^+ \rightarrow D^{(*)+}D^{(*)-}K^+$ decays

measure experimentally. They represent a good compromise between an expected high branching ratio and ease of reconstruction. It has been suggested by Colangelo and De Fazio [68] that these modes could be used to carry out tests of the validity of the factorisation approximation for nonleptonic B decays [69]. They show that if it is assumed that the processes

$$B^0 \rightarrow D^{*-}D^0K^+, \tag{2.66}$$

and

$$B^0 \rightarrow D^{*-}D^{*0}K^+ \tag{2.67}$$

proceed primarily through two–body intermediate states such as

$$B^0 \rightarrow D^{*-}D_s^X, \tag{2.68}$$

followed by the strong transition

$$D_s^X \to D^{(*)0} K^+, \tag{2.69}$$

then they can be used to measure the couplings of heavy mesons to light pseudoscalar states.

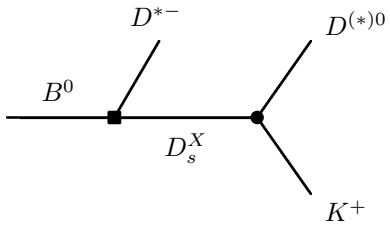

Figure 2.8: Diagram contributing to the decay $B^0 \to D^{*-} D^{(*)0} K^+$. The box represents a weak transition, the dot a strong vertex [68].

The CLEO collaboration provided the first determination of the strong coupling constant $g_{D^*D\pi}$ for $D^{*+} \to D^0\pi^+$ decays with a measurement of the total width of the D^{*+} meson, together with the branching fraction $\mathcal{B}(D^{*+} \to D^0\pi^+)$ [70]. This coupling, defined by the matrix element

$$\left\langle D^0(k)\pi^+(q)|D^{*+}(p,\epsilon)\right\rangle = g_{D^*D\pi}\epsilon \cdot q, \tag{2.70}$$

where ϵ is the D^* polarisation vector, was measured to be

$$g_{D^*D\pi} = 17.9 \pm 0.3 \pm 1.9. \tag{2.71}$$

The coupling $g_{D^*D\pi}$ in equation 2.70 is related to one of the basic parameters, g, in the heavy–quark chiral effective theory. It can be redefined [71] as

$$g_{D^*D\pi} = \frac{2\sqrt{m_D m_D^*}}{f_\pi} g_D = \frac{2\sqrt{m_D m_D^*}}{f_\pi} g \left(1 + \mathcal{O}\left(\frac{1}{m_c}\right)\right), \tag{2.72}$$

where g_D is an effective coupling[2], and f_π is the pion decay constant. The result (2.71) implies

$$g_D = 0.59 \pm 0.01 \pm 0.07. \tag{2.73}$$

Recent lattice QCD calculations agree very well with the CLEO result. Abada et al. [72] obtain

$$g_{D^*D\pi} = 18.8 \pm 2.3^{+1.1}_{-2.0}, \tag{2.74}$$

and

$$g_D = 0.67 \pm 0.08^{+0.04}_{-0.06}, \tag{2.75}$$

[2] assuming a (not so heavy) charmed heavy mass rather than an infinitely heavy quark mass

The coupling constant g in equation 2.72 describes the strong coupling of charmed and beauty mesons to members of the octet of light pseudoscalars in the heavy quark limit. Therefore, neglecting $SU(3)_F$ breaking effects, this coupling enters some matrix elements for the transitions in the process (2.69). It has been studied extensively, although most theoretical results for g have been lower than the experimentally determined one. An extensive list of the theoretical results can be found in Refs. [71, 73, 74, 75].

2.6.1 Decay amplitudes

Following the formalism of Colangelo and De Fazio, the processes (2.66) and (2.67):

$$B^0(p) \quad \rightarrow \quad D^{*-}(p_-,\epsilon_-)D^0(p_D)K^+(q); \tag{2.76}$$

$$B^0(p) \quad \rightarrow \quad D^{*-}(p_-,\epsilon_-)D^{*0}(p_{D^*},\epsilon)K^+(q), \tag{2.77}$$

with momenta $p = m_B v$, $p_- = m_{D^*} v_-$ and $p_{D^{(*)}} = m_{D^{(*)}} w$, are, when penguin contributions are ignored, governed by the effective weak Hamiltonian

$$H_W = \frac{G_F}{\sqrt{2}} V_{cs} V_{cb}^* a_1 \bar{b}\gamma_\mu \left(1-\gamma_5\right) c\bar{c}\gamma^\mu \left(1-\gamma_5\right) s\,, \tag{2.78}$$

where G_F is the Fermi constant, and $a_1 = \left(c_1 + \frac{c_2}{N_c}\right)$, with $c_{1,2}$ short–distance Wilson coefficients and N_c is the number of colours. The Dalitz plot variables are defined as

$$\begin{aligned} s &= (p_{D^{(*)}} + q)^2 \\ s_- &= (p_- + q)^2\,, \end{aligned} \tag{2.79}$$

and are constrained by the kinematics of the decay to be

$$\begin{aligned} (m_{D^{(*)}} + m_K)^2 \leq \quad & s \quad \leq (m_B - m_{D^*})^2 \\ (s_-)_- \leq \quad & s_- \quad \leq (s_-)_+. \end{aligned} \tag{2.80}$$

Colangelo and De Fazio's work assumes that the $B^0 \rightarrow D^{*-}D^{(*)0}K^+$ decays proceed through polar diagrams such as figure 2.8, and uses the factorisation approximation for the weak transition. For $B^0 \rightarrow D^0 D^{*-} K^+$ the intermediate D_s^X state can either be a vector meson, D_s^{*+} $(J^P = 1^-)$, or a scalar meson, D_{s0}^+ $(J^P = 0^+)$, together with their radial excitations. The possibilities for $B^0 \rightarrow D^{*0}D^{*-}K^+$ are: D_s^{*+} $(J^P = 1^-)$; D_s^+ $(J^P = 0^-)$; and D_{1s}^{*+} $(J^P = 1^+)$ and their radial excitations. Therefore the calculation of the amplitudes in figure 2.8 requires the evaluation of the strong vertices

$$\left\langle D^0(p_D)K^+(q)|D_s^*(p_{D_s^*},\epsilon_s)\right\rangle \quad = \quad g_{D_s^* DK}(\epsilon_s \cdot q)$$

$$\begin{aligned}
\left\langle D^0(p_D)K^+(q)|D^+_{s0}(p_{D_{s0}})\right\rangle &= g_{D_{s0}DK} \\
\left\langle D^{*0}(p_{D^*},\epsilon)K^+(q)|D^*_s(p_{D^*_s},\epsilon_s)\right\rangle &= i\,\frac{g_{D^*_sD^*K}}{m_{D^*_s}}\,\epsilon_{\tau\theta\phi\psi}\epsilon^\tau_s\epsilon^{*\theta}p^\phi_{D^*_s}q^\psi \\
\left\langle D^{*0}(p^*_D,\epsilon)K^+(q)|D_s(p_{D_s})\right\rangle &= g_{D^*D_sK}(\epsilon^*\cdot q) \\
\left\langle D^{*0}(p^*_D,\epsilon)K^+(q)|D^{*+}_{s1}(p_{D^*_{s1}},\epsilon_s)\right\rangle &= \frac{g_{D^*_{s1}D^*K}}{m_{D^*_{s1}}}\,(\epsilon^*\cdot\epsilon_s)(p_{D^*}\cdot q)\ ,
\end{aligned} \tag{2.81}$$

and the associated matrix elements for their radial excitations.

In the heavy quark limit all the couplings in equation 2.81 may be expressed in terms of two coupling constants, g and h, for the D^X_s negative and positive parity states respectively, which arise in an effective Lagrangian [76, 77, 78, 79], where the term for the strong interactions of the heavy mesons with the light pseudoscalars is

$$\mathcal{L}_I = ig\mathrm{Tr}\left\{H_b\gamma_\mu\gamma_5\mathcal{A}^\mu_{ba}\bar{H}_a\right\} + \left[ih\mathrm{Tr}\left\{H_b\gamma_\mu\gamma_5\mathcal{A}^\mu_{ba}\bar{S}_a\right\} + \mathrm{h.c.}\right]. \tag{2.82}$$

The field H_a in equation 2.82 describes the negative parity $J^P = (0^-, 1^-)$ $\bar{q}Q$ meson doublet, with $s^P_l = \frac{1}{2}^-$. The field S_a describes the positive parity states with $s^P_l = \frac{1}{2}^+$.

In Heavy Hadron Chiral Perturbation Theory (HHChPT) the heavy mesons, H_a and S_a, are described by the 4×4 Dirac matrices

$$H_a = \frac{1+\not{v}}{2}[P^*_{a\mu}\gamma^\mu - P_a\gamma_5], \tag{2.83}$$

$$S_a = \frac{1+\not{v}}{2}[P^{'*}_{a\mu}\gamma^\mu\gamma_5 - P^{'}_a], \tag{2.84}$$

where in this instance v is the heavy meson velocity, and $P^*_{a\mu}$ and P_a are the annihilation operators of the 1^- and 0^- $\bar{q}_aQ$ mesons ($a = 1, 2, 3$ for u, d and s). The light pseudoscalar mesons enter through the axial vector current

$$\mathcal{A}_{\mu ba} = \frac{1}{2}\left(\xi^\dagger\partial_\mu\xi - \xi\partial_\mu\xi^\dagger\right)_{ba}, \tag{2.85}$$

where the field $\xi = e^{\frac{i\mathcal{M}}{f_\pi}}$ contains the octet of pseudoscalar mesons

$$\mathcal{M} = \begin{pmatrix} \sqrt{\frac{1}{2}}\pi^0 + \sqrt{\frac{1}{6}}\eta & \pi^+ & K^+ \\ \pi^- & -\sqrt{\frac{1}{2}}\pi^0 + \sqrt{\frac{1}{6}}\eta & K^0 \\ K^- & \bar{K}^0 & -\sqrt{\frac{2}{3}}\eta \end{pmatrix}. \tag{2.86}$$

From the relations of equation 2.82 the strong couplings defined in equation 2.81 may be expressed in terms of g and h as

$$g_{D^*_sDK} = \frac{2\sqrt{m_{D^*_s}m_D}}{f_K}\,g$$

$$\begin{aligned} g_{D_{s0}DK} &= -\sqrt{m_{D_{s0}} m_D}\, \frac{m_{D_{s0}}^2 - m_D^2}{m_{D_{s0}}}\, \frac{h}{f_K} \\ g_{D_s^* D^* K} &= \frac{2 m_{D_s^*}}{f_K}\, g \\ g_{D^* D_s K} &= \frac{2\sqrt{m_{D^*} m_{D_s}}}{f_K}\, g \\ g_{D_{s1}^* D^* K} &= -\frac{2\sqrt{m_{D_{s1}^*} m_{D^*}}}{f_K}\, h \ , \end{aligned} \tag{2.87}$$

which keeps some $SU(3)$ flavour breaking terms in the masses of the D_s^X mesons and in the leptonic constant f_K.

The weak transition of (2.68) can be modelled by the semileptonic $B^0 \to D^{*-}$ matrix element and the decay constants of the D_s^X mesons using the factorisation approximation. In the heavy quark limit the matrix element is

$$\begin{aligned} \left\langle D^{*-}(v_-, \epsilon_-) | V^\mu - A^\mu | B(v) \right\rangle &= \sqrt{m_B m_{D^*}}\, \xi(v \cdot v_-)\, \epsilon_{-\alpha}^* \\ &\quad \left(-i\varepsilon^{\rho\alpha\lambda\mu} v_\rho v_{-\lambda} - (1 + v \cdot v_-)\, g^{\alpha\mu} + v^\alpha v_-^\mu \right), \end{aligned} \tag{2.88}$$

with the Isgur–Wise function ξ. The decay constants for the D_s^X are given by

$$\begin{aligned} \left\langle D_s^+(p_{D_s}) | \bar{c}\gamma^\mu(1-\gamma_5)s|0 \right\rangle &= i f_{D_s} p_{D_s}^\mu \\ \left\langle D_s^{*+}(p_{D_s^*}, \epsilon_s) | \bar{c}\gamma^\mu(1-\gamma_5)s|0 \right\rangle &= f_{D_s^*} m_{D_s^*} \epsilon_s^{*\mu} \\ \left\langle D_{s0}^+(p_{D_{s0}}) | \bar{c}\gamma^\mu(1-\gamma_5)s|0 \right\rangle &= i f_{D_{s0}} p_{D_{s0}}^\mu \\ \left\langle D_{s1}^{*+}(p_{D_{s1}^*}, \epsilon_s) | \bar{c}\gamma^\mu(1-\gamma_5)s|0 \right\rangle &= f_{D_{s1}^*} m_{D_{s1}^*} \epsilon_s^{*\mu} \ . \end{aligned} \tag{2.89}$$

Decay widths

The widths of the decay modes $B^0 \to D^0 D^{*-} K^+$ and $B^0 \to D^{*0} D^{*-} K^+$ can then be expressed as

$$\Gamma(B^0 \to D^{(*)0} D^{*-} K^+) = \int_{(m_{D^{(*)}} + m_K)^2}^{(m_B - m_{D^*})^2} ds \int_{(s_-)_-}^{(s_-)_+} ds_- \, \frac{d\Gamma}{ds\, ds_-} \tag{2.90}$$

where

$$\frac{d\Gamma}{ds\, ds_-}(B^0 \to D^{(*)0} D^{*-} K^+) = \frac{1}{(2\pi)^3} \frac{1}{32 m_B^3} |\bar{\mathcal{A}}|^2, \tag{2.91}$$

and

$$\mathcal{A}(B^0 \to D^0 D^{*-} K^+) = \sum_{i=1,2} \mathcal{A}_i \tag{2.92}$$

$$\mathcal{A}(B^0 \to D^{*0} D^{*-} K^+) = \sum_{i=1,2,3} \mathcal{A}_i^* \ . \tag{2.93}$$

The amplitudes $\mathcal{A}_1$ and $\mathcal{A}_2$ correspond to the $B^0 \to D^0 D^{*-} K^+$ decaying via an intermediate D_s^* or D_{s0} meson respectively. Likewise, $\mathcal{A}_1^*$, $\mathcal{A}_2^*$, and $\mathcal{A}_3^*$ represent the amplitudes for $B^0 \to D^{*0} D^{*-} K^+$ proceeding through a D_s^*, D_s, or D_{s1}^* intermediate state. These amplitudes depend on g and h through the relationships of equations 2.87 and 2.81.

Using available experimental data and theoretical predictions for the decay widths of the intermediate states [7, 80, 81] Colangelo and De Fazio determined the theoretically allowable ranges for g and h. Their result is shown in figure 2.9. The vertical line represents the CLEO result [70], while the solid and dashed lines represent one and two standard deviation constraints respectively.

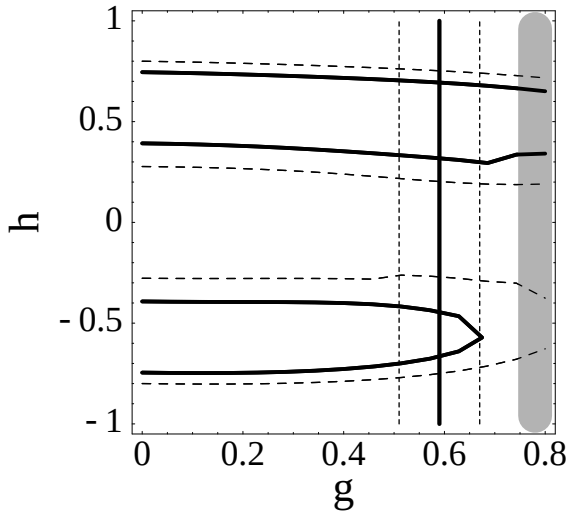

Figure 2.9: Theoretical constraints for the coupling constants g and h [68].

These results constrain h, the coupling constant for the D_s^X positive parity states, to the region $|h| = 0.6 \pm 0.2$, whereas g, the coupling for the negative parity states, extends over almost the whole allowable range. This implies that the main contributions to (2.66) and (2.67) are from the positive parity 0^+ and 1^+ states D_{s0} and D_{s1}^*, since the amplitudes display only a minor sensitivity to the coupling, g, of the negative parity intermediate states. If this is the case then a study of the Dalitz plot for the three body decays of (2.66) and (2.67) can be used to study the properties of the as yet unobserved D_{s0} and D_{s1}^* resonances [47, 50, 51].

Figure 2.10(a) shows the predicted differential decay width for $B^0 \to D^{*-}D^0K^+$, using $g = 0.5$ and $h = -0.6$. The main variation in the differential decay distribution occurs along the direction of the D^0

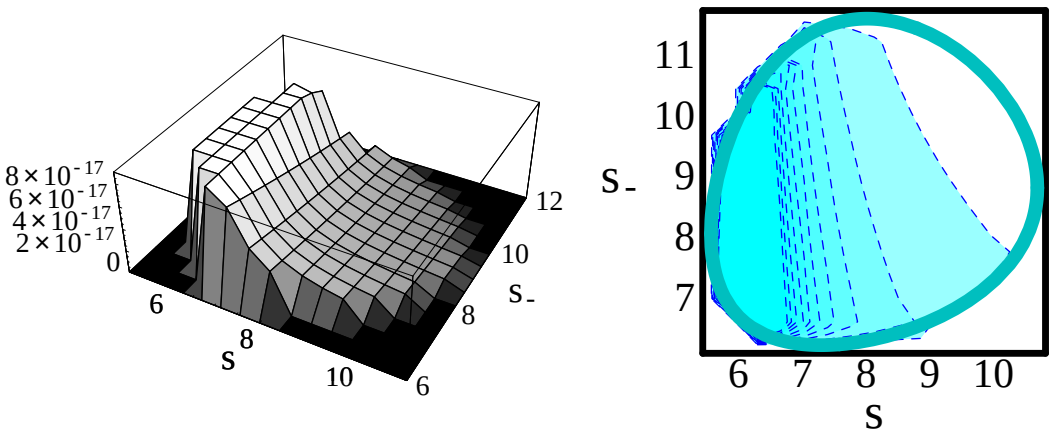

(a) Differential decay width $\frac{d\Gamma}{ds\,ds_-}$.

(b) Dalitz plot.

Figure 2.10: Differential decay width and Dalitz plot for $B^0 \to D^{*-}D^0K^+$. Units of s and s_- are GeV^2 [68].

K^+ invariant mass, which is due to the unique topology of the Cabibbo and colour allowed amplitudes for $B^0 \to D^{*-}D^0K^+$. The same features are exhibited in the Dalitz plot for $B^0 \to D^{*-}D^{*0}K^+$ in figure 2.11.

2.7 Summary

The ultimate goal of an analysis of doubly charmed B meson decays would be to measure *CP* violation via the decay $B^0 \to D^{*+}D^{*-}K_S$. While time dependent *CP* asymmetries have been measured by both the Belle and BABAR collaborations, further measurements using additional decay modes can only aid in increasing the precision of the measurement. Further, a time dependent analysis of $B^0 \to D^{*+}D^{*-}K_S$ decays could be used to resolve any $\phi_1 \to \pi/2 - \phi_1$ ambiguity by additionally measuring $\cos(2\phi_1)$. Unfortunately this aim remains out of reach for both the SLAC and KEK B–factories for the moment.

Nonetheless, it remains the case that at present little is known regarding $B \to D^{(*)}\bar{D}^{(*)}K$ decays generally. It has been predicted that they form a substantial fraction of B meson decays. Any measurement of doubly charmed decay branching ratios will increase the sum of knowledge in this area.

With a large enough sample with sufficient purity of $B^0 \to D^{*-}D^{(*)0}K^+$ decays it should also be possible to perform a Dalitz analysis to search for intermediate resonances. Some of these predicted resonances are states that have never been observed experimentally.

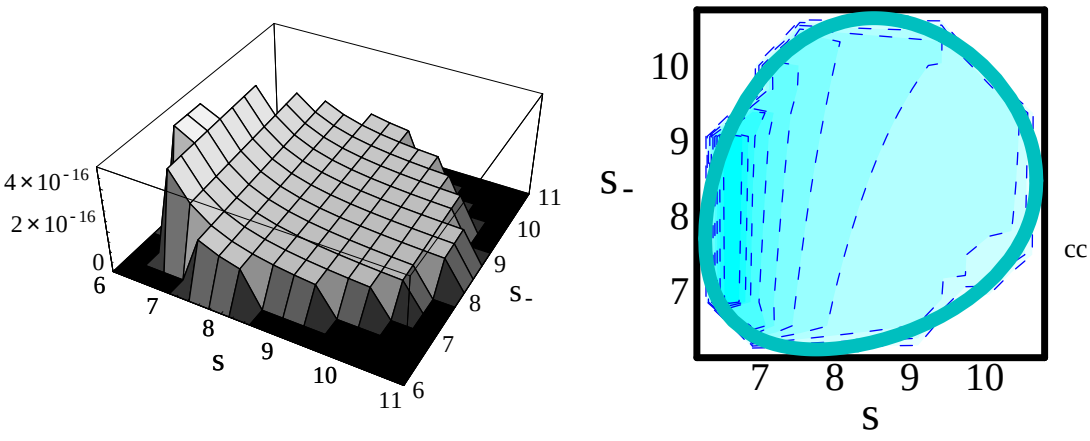

(a) Differential decay width $\frac{d\Gamma}{ds\, ds_-}$.

(b) Dalitz plot.

Figure 2.11: Differential decay width and Dalitz plot for $B^0 \to D^{*-} D^{*0} K^+$. Units of s and s_- are GeV^2 [68].

Large numbers of B meson decays are required to perform any of these analyses. Detection of time dependent *CP* violation requires an asymmetric particle collider, as discussed in §2.3.3. Two such accelerator and detector facilities have been built and are currently operational. One is at SLAC, the Stanford Linear Accelerator Centre. The other, the KEK B–factory, is discussed in the next chapter.

Chapter 3

The Belle experiment

The Belle experiment is a collaboration of over 350 scientists from 54 institutes in 10 countries. It is taking place at the KEK High Energy Accelerator Research Organisation in Tsukuba, Japan. The primary aim of the experiment is to observe and measure *CP* violation in the B meson system.

The KEKB accelerator is used to produce large numbers of B mesons for the Belle detector to study. Particle colliders which have been engineered to mass produce these types of particles have collectively been referred to as B–factories. CESR, PEP-II and KEKB are three such electron–positron colliders, where the centre of mass energy is tuned to the $\Upsilon(4S)$ resonance. Both PEP–II and KEKB are asymmetric colliders, ie, they collide electrons and positrons of different energies, so that the $\Upsilon(4S)$ is created with a boost in the laboratory reference frame.

Commissioning of the KEKB accelerator commenced in December 1998, and the Belle detector started to take data from beam interactions on 1 June 1999.

3.1 The KEKB accelerator and storage ring

KEKB is an asymmetric e^+ e^- collider operating at the $\Upsilon(4s)$ resonance. Electrons are accelerated to $8.0\,\mathrm{GeV}$ and then injected into the High Energy Ring (HER), while positrons are accelerated to $3.5\,\mathrm{GeV}$ and then stored in the Low Energy Ring (LER). The two meet in Tsukuba Hall, and the e^+ and e^- collide at the Interaction Point (IP), shown in figure 3.1.

The centre of mass energy of the collisions is

$$\sqrt{s} = \sqrt{4E^+E^-} = 10.58\ \mathrm{GeV}, \tag{3.1}$$

which is the invariant mass of the $\Upsilon(4S)$. Figure 3.2 illustrates the cross section for the production of Υ resonances in e^+ e^- collisions. Since more than 96% of $\Upsilon(4S)$ decays are to $B\bar{B}$ pairs [7], this a very efficient method to produce large samples of B mesons.

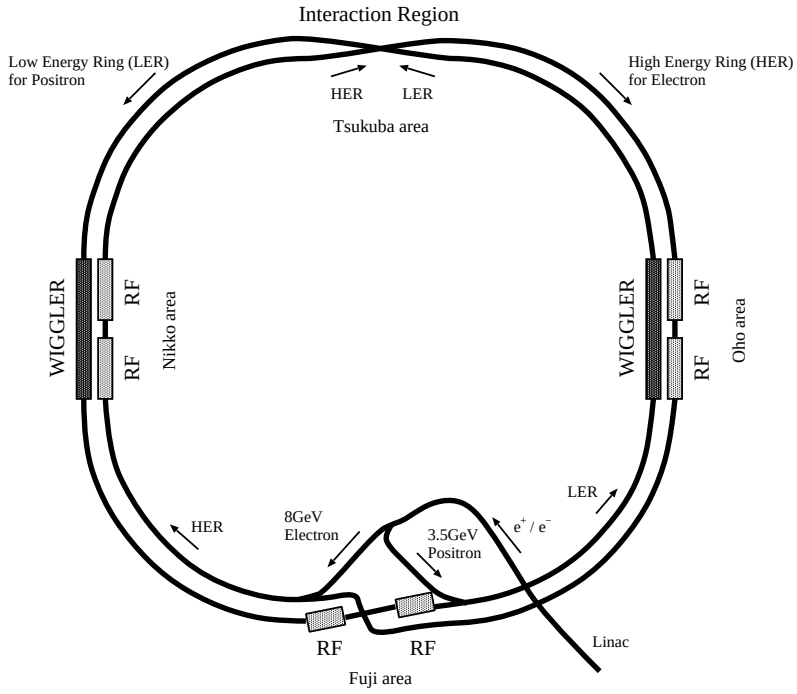

Figure 3.1: Confi guration of the KEKB storage ring.

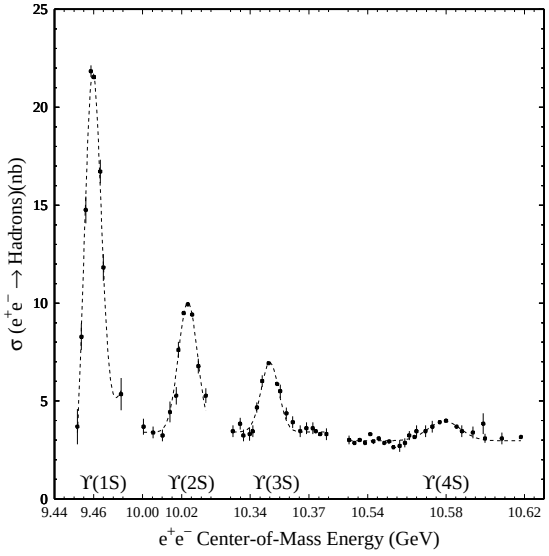

Figure 3.2: Cross section of Υ production in $e^+ e^-$ collisions.

Due to the asymmetry in the momentum of the e^+ and e^-, the $\Upsilon(4S)$ is produced with a Lorentz boost of

$$\beta\gamma = \frac{E^- - E^+}{\sqrt{s}} = 0.425 \tag{3.2}$$

in the laboratory rest frame.

The rate at which $B\bar{B}$ pairs can be created is also an important factor, and is measured as the luminosity. The luminosity can be expressed as

$$\mathcal{L} = 2.17 \times 10^{34} \xi (1+r) \frac{EI}{\beta_y^*}_{\pm} , \tag{3.3}$$

where

ξ	$=$	beam–beam tune shift
r	$=$	aspect ratio of the beam shape,
		where 1 corresponds to a circular beam and 0 to a flat beam
E	$=$	beam energy in GeV
I	$=$	the current stored in amps
β_y^*	$=$	the vertical beta function at the IP in cm

and the $\pm$ subscript implies that the current and energy parameters may be taken either from the HER or LER.

Electrons and positrons do not collide head on at the IP, but at a finite crossing angle of $22\ \mathrm{mrad}$. This substantially reduces background from synchrotron radiation, and allows for the future installation of *crab kickers* which will improve the maximum luminosity. The maximum design luminosity of KEKB is $10^{34}\ \mathrm{cm}^{-2}\mathrm{s}^{-1}$. By July 2002 the maximum luminosity achieved was $7.348 \times 10^{33}\,\mathrm{cm}^{-2}\mathrm{s}^{-1}$, and $90.04\,\mathrm{fb}^{-1}$ of data had been collected, which is some indication of the dedication of the many people working on the accelerator. The design specifications of KEKB are listed in table 3.1.

3.2 The Belle detector

The Belle detector is situated in Tsukuba Hall at the IP of the KEKB accelerator. Belle consists of several subdetectors as shown in figures 3.3 and 3.4. Tracking of charged particles is performed by the Central Drift Chamber (CDC) and Silicon Vertex Detector (SVD). Calorimetry and electron identification is done by the Electromagnetic Calorimeter (ECL) in conjunction with the Extreme Forward Calorimeter (EFC). Further particle identification is achieved with the aid of combined information from the CDC, Time of Flight counter (TOF) and the Aerogel Čerenkov Counter (ACC). The K_L and μ detector (KLM)'s primary purpose is to identify K_L mesons and muons. The performance of the Belle detector is described in detail elsewhere [83].

		LER	HER	
Energy	E	3.5	8.0	GeV
Circumference	C	3016.26		m
Luminosity	$\mathcal{L}$	1×10^{34}		$\mathrm{cm}^{-2}\mathrm{s}^{-1}$
Crossing angle	θ_x	± 11		mrad
Tune shifts	ξ_x/ξ_y	$0.039/0.052$		
Beta function at IP	β_x^*/β_y^*	$0.33/0.01$		m
Beam current	I	2.6	1.1	A
Natural bunch length	σ_z	0.4		cm
Energy spread	σ_E/E	7.1×10^{-4}	6.7×10^{-4}	
Bunch spacing	s_B	0.59		m
Particles per bunch	N	3.3×10^{10}	1.4×10^{10}	
Emittance	ξ_x/ξ_y	$1.8 \times 10^{-8}/3.6 \times 10^{-10}$		m
Synchrotron tune	ν_s	$0.01 \sim 0.02$		
Betatron tune	ν_x/ν_y	$45.52/45.08$	$47.52/46.08$	
Momentum compaction factor	α_p	$1 \times 10^{-4} \sim 2 \times 10^{-4}$		
Energy loss per turn	U_0	$0.81^{\dagger}/1.5^{\ddagger}$	3.5	MeV
RF voltage	V_c	$5 \sim 10$	$10 \sim 20$	MV
RF frequency	f_{RF}	508.887		MHz
Harmonic number	h	5120		
Longitudinal damping time	τ_ε	$43^{\dagger}/23^{\ddagger}$	23	ms
Total beam power	P_b	$2.7^{\dagger}/4.5^{\ddagger}$	4.0	MW
Radiation power	P_{SR}	$2.1^{\dagger}/4.0^{\ddagger}$	3.8	MW
HOM power	P_{HOM}	0.57	0.15	MW
Bending radius	ρ	16.3	104.5	m
Length of bending magnet	l_B	0.915	5.86	m

†: without wigglers, ‡: with wigglers

Table 3.1: KEKB accelerator design parameters (from [82]).

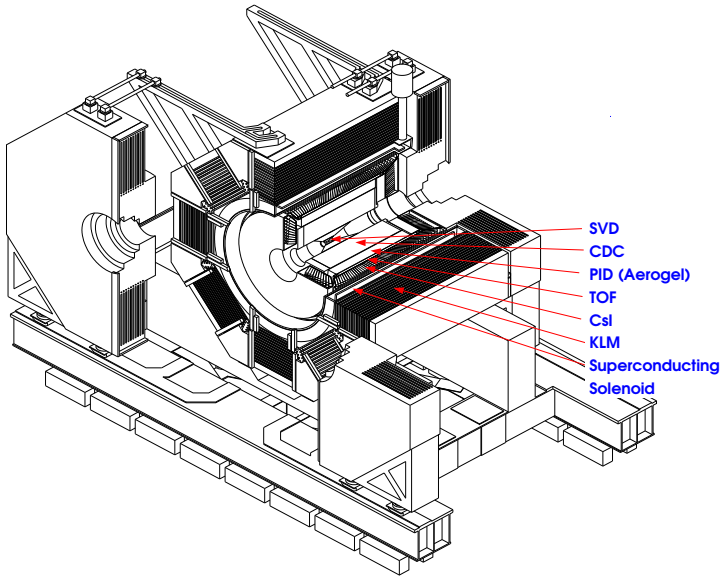

Figure 3.3: The Belle detector.

3.2.1 Silicon Vertex Detector (SVD)

The Lorentz boost of the $\Upsilon(4S)$ is introduced so that time–dependent *CP* asymmetries in the decay of B mesons may be measured by detecting the flight length difference between the two B mesons. The SVD is capable of measuring the difference in z–vertex positions for B meson pairs to within a precision of $100\ \mu\mathrm{m}$. The SVD is also used for charged particle tracking to a limited extent.

The SVD is the innermost of the detectors in Belle, and is mounted radially around the beam pipe. It consists of three layers of detector ladders, consisting of 8, 10 and 14 Double Sided Silicon Detectors (DSSDs), as shown in figure 3.5. The inner layer is at a radius of of $3.0\ \mathrm{cm}$, the middle at $4.55\ \mathrm{cm}$, and the outer layer at $6.05\ \mathrm{cm}$. A solid angle of $23^\circ < \theta < 139^\circ$, where θ is the angle from the beam axis, is covered, corresponding to 86% of the full solid angle.

Each ladder is made from two half ladders, which may be either short half ladders (DHSs) or long half ladders (DHLs). A DHS consists of a DSSD glued at one end to a pair of hybrid readout cards, which are glued back to back. Each hybrid card is responsible for the readout of the side of the DSSD to which it is attached. DHLs are made of two DSSDs, which are glued end to end. Ladders in the inner, middle and outer layers consist of short–short, short–long, and long–long half ladder pairs, are glued end to end such that the hybrid readout cards are at each end of the subdetector. Each half of a full ladder is electronically separate from the other half.

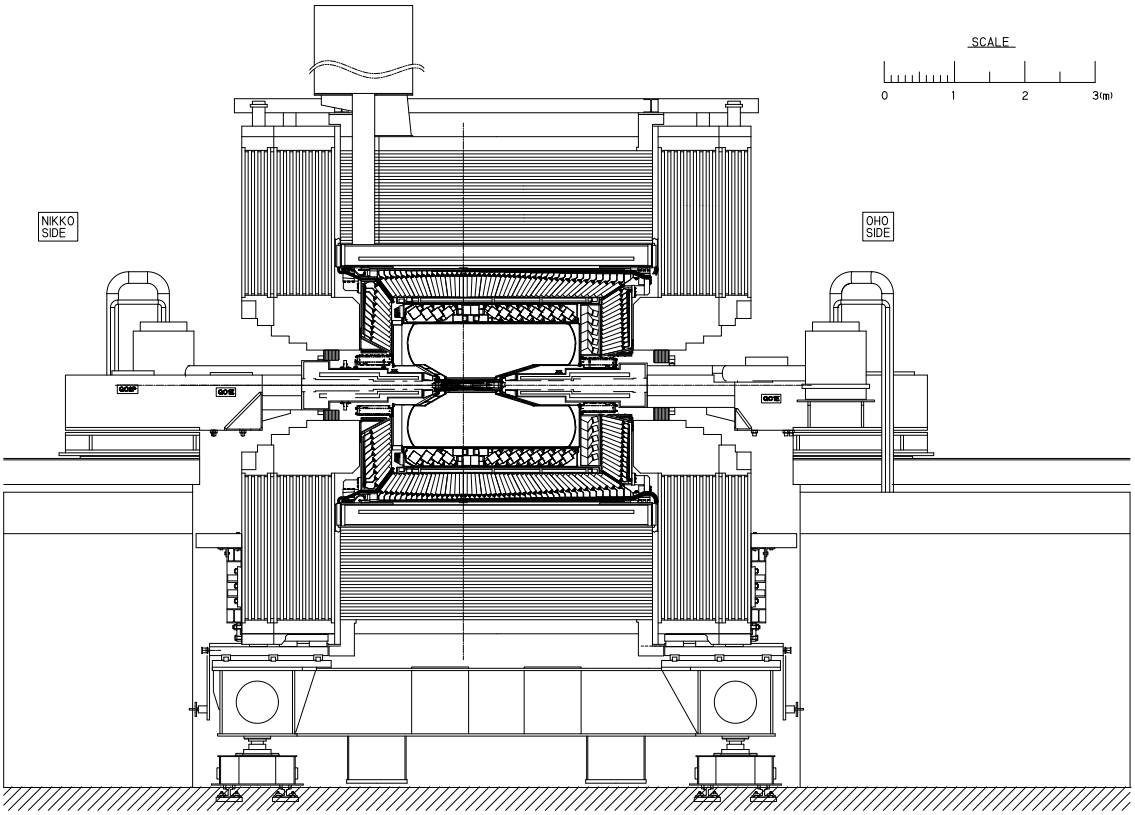

Figure 3.4: Side view of the Belle detector.

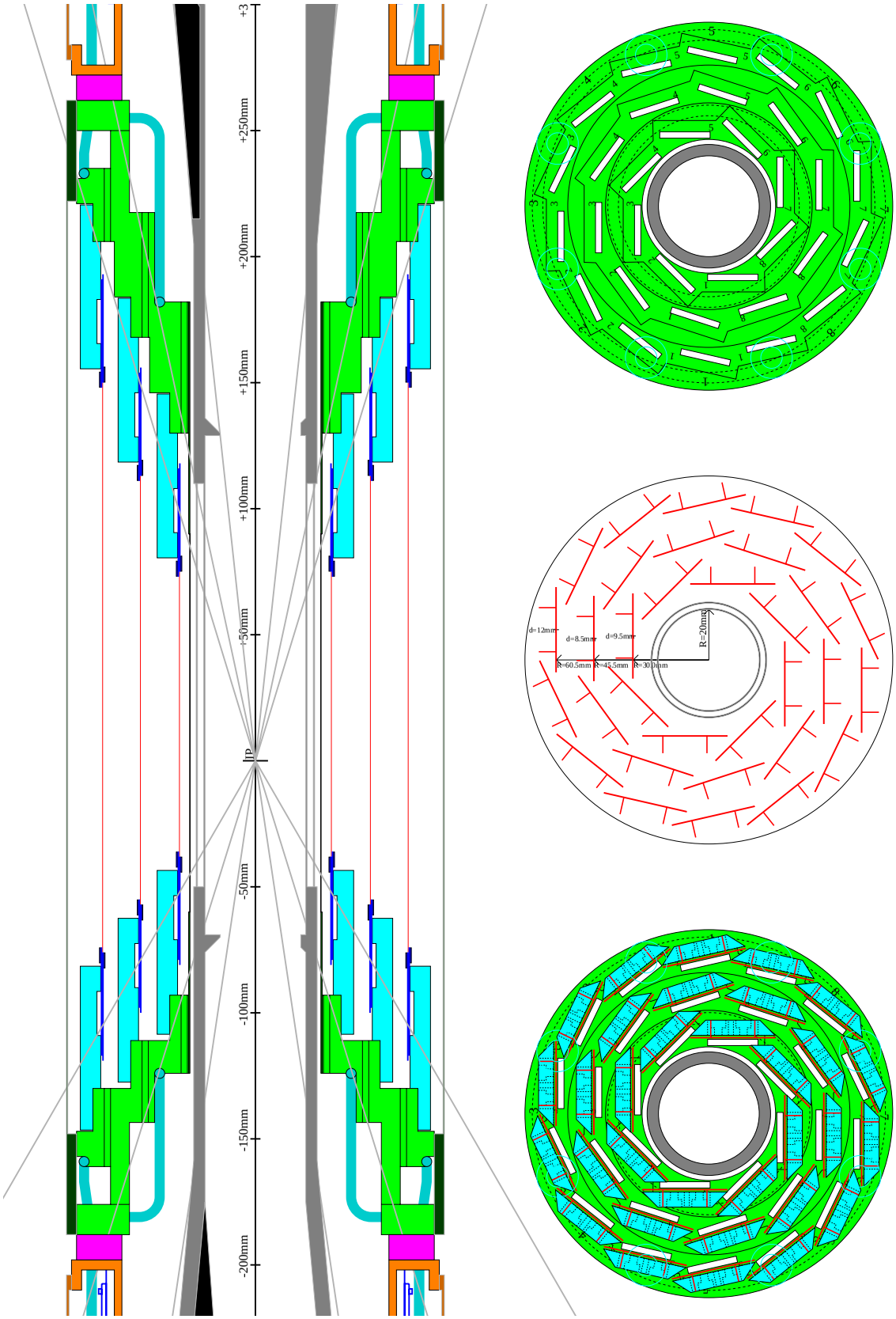

Figure 3.5: The Silicon Vertex Detector.

Each DSSD is essentially a pn junction. In operation each detector is reverse biased so that the bulk of the silicon reaches full depletion. When a charged particle travels through the detector it excites an electron out of the valence band of the silicon and into the conduction band, creating an electron–hole pair. The electron then travels towards towards the positively charged side, and the hole to the negatively charged side of the DSSD. When these reach the sense strips a hit is detected.

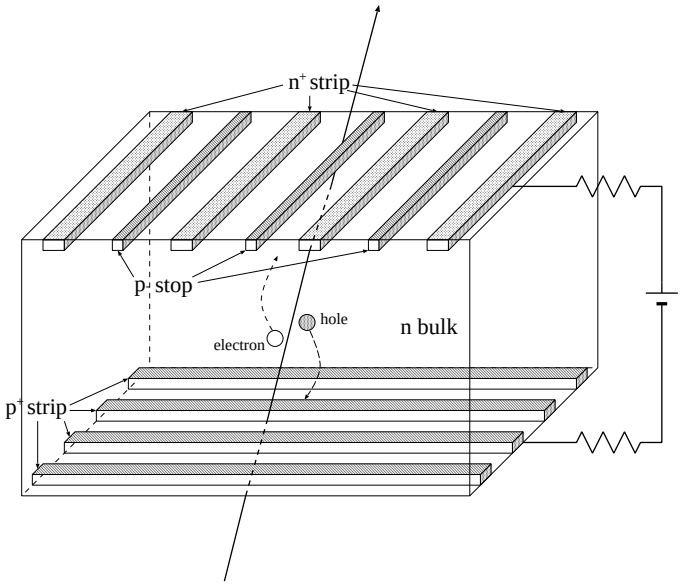

Figure 3.6: Schematic view of a Double Sided Silicon Detector.

The SVD uses S6936 DSSDs, fabricated by Hamamatsu Photonics, which were originally developed for the DELPHI micro–vertex detector. The bulk of the DSSD is n doped silicon, as shown in figure 3.6. The n^+ z readout strips have a pitch of 42 μm. Measurement of hits in the ϕ direction is made with p^+ strips, each with a pitch of 25 μm. Each side of the DSSD has 1280 sense strips, every second of which is connected to the 640 readout pads at each end. A DSSD measures $57.5 \times 33.5 \times 0.3$ mm.

3.2.2 Central Drift Chamber (CDC)

The CDC is a tracking wire chamber, and is used to determine the momenta and specific ionisation, dE/dx, of particles travelling through Belle. It provides an angular coverage of $17^\circ \leq \theta \leq 150^\circ$, from a radius of 77 to 880 mm, as shown in figure 3.7.

The CDC is made of 8400 drift cells. Each cell consists of a sense wire, held at a positive voltage, surrounded by 6 field wires held at a negative voltage, strung along the axis of the beam pipe. A charged particle travelling through the CDC ionises the gas mixture in which the wires are strung. The ionised electrons are attracted to the sense wire, and, as they move towards it, cause further ionisation of the gas mixture. When these electrons reach the sense wire a hit is registered on that wire. The path of particles

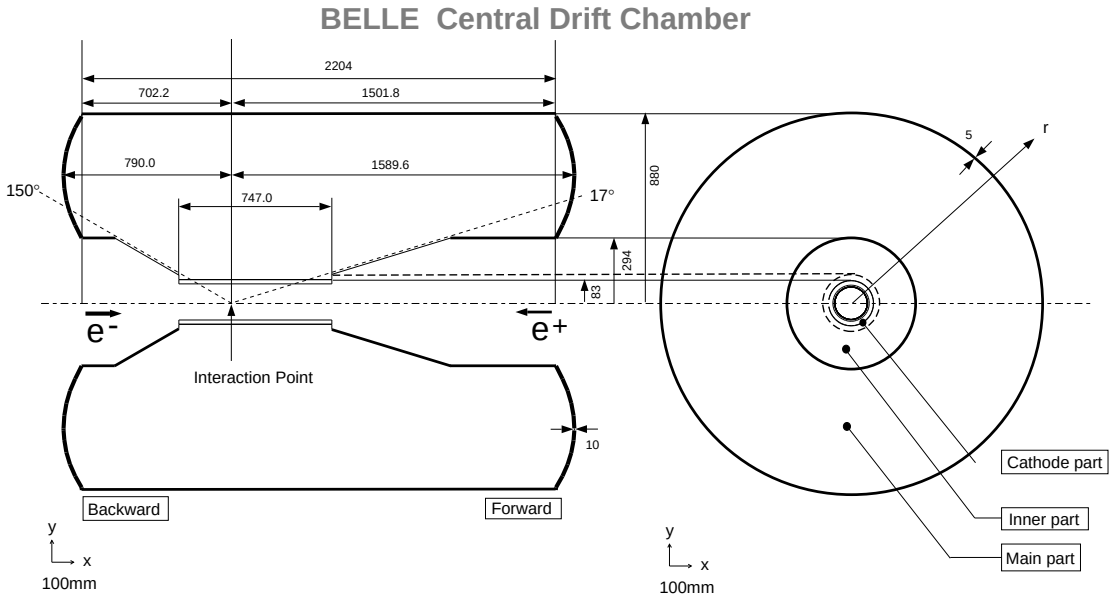

Figure 3.7: The Central Drift Chamber.

in the $r-\phi$ plane is measured by axial cells. Stereo cells, mounted at a slight angle to the beam pipe, are used to determine the z components of tracks.

The spatial resolution in $r-\phi$ is $130\ \mu\mathrm{m}$, and less than $2\ \mathrm{mm}$ in z. The transverse momentum resolution is

$$\frac{\sigma_{p_T}}{p_T} = \sqrt{(0.19 p_T)^2 + (0.34)^2}\% \tag{3.4}$$

The gas mixture of 50% helium and 50% ethane which is used in the CDC has a relatively long radiation length of $640\ \mathrm{m}$, which minimises multiple scattering and the associated tracking errors. The ethane component provides for good dE/dx resolution of 6.9% for minimum ionising particles since ethane has a very narrow energy loss distribution. Particle identification for tracks with momentum up to $0.8\ \mathrm{GeV}/c$ is performed using dE/dx information from the CDC. The distribution of dE/dx as a function of momentum is demonstrated in figure 3.8, where the different signal shapes from pions, kaons and protons can be clearly distinguished. The lines in the figure represent the expected energy loss for each type of particle.

3.2.3 Aerogel Čerenkov Counter (ACC)

A critical improvement in the design of Belle over detectors previously used in B physics experiments is the inclusion of particle identification subdetectors to provide pion and kaon separation. At low momenta, measurements of ionisation energy losses in the CDC (see §3.2.2) may be used for particle separation, however, this method becomes ineffective above about $0.8\ \mathrm{GeV}/c$. The TOF, described in §3.2.4, extends

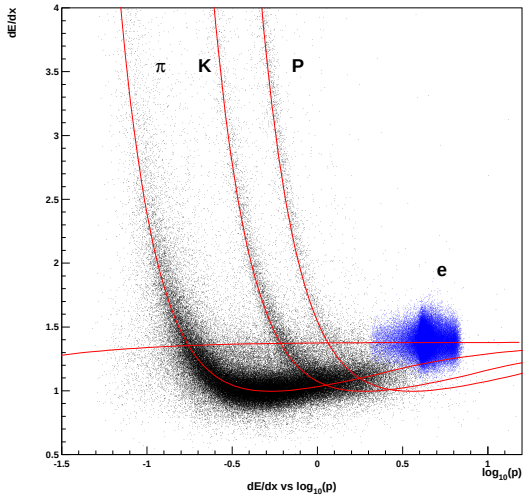

Figure 3.8: Truncated mean of dE/dx versus momentum. The points are measurements taken during accelerator operations, and the lines are the expected distributions for each particle type.

this for particles with momentum up to $1.2\ \mathrm{GeV}/c$, but only for the barrel region of the detector. The ACC is used primarily to distinguish particles with momentum of up to 2.5 or $3.5\ \mathrm{GeV}/c$, depending on the polar angle, in the barrel region. In the endcap region of the detector, where there is no TOF, the ACC is used to identify particles in the momentum range 0.8 to $2.1\ \mathrm{GeV}/c$.

The ACC is a threshold Čerenkov counter system. When a charged particle travels through a dispersive medium of refractive index n it excites, and partly polarises, the atoms in the material. If the velocity of the particle is greater than the speed of light in the medium, c/n, part of the excitation energy reappears as coherent radiation, emitted at a characteristic angle to the direction the particle is moving in. This is known as Čerenkov radiation.

Figure 3.9 demonstrates the materials of differing n in various parts of the detector. These refractive indexes are chosen in order to obtain good K/π separation for the whole kinematic range, depending on the polar angle. The ACC consists of modules containing silica Aerogel. This material was selected since it is very transparent to light, and its refractive index, which ranges from 1.01 to 1.03, is ideal for threshold separation of pions and kaons. For a pion and a kaon with identical momentum the pion will have a higher velocity due to its lower mass. In the momentum range 1 to $4\ \mathrm{GeV}/c$ pions will be travelling faster than c/n and will emit a flash of Čerenkov light. Thus particles with an associated pulse of light in the ACC are more likely to be pions than kaons.

There are two sections to the ACC:

The Barrel ACC consists of 960 modules, segmented into 60 cells in the ϕ direction;

The Endcap ACC is placed only on the forward side of the detector. It consists of 228 modules arranged

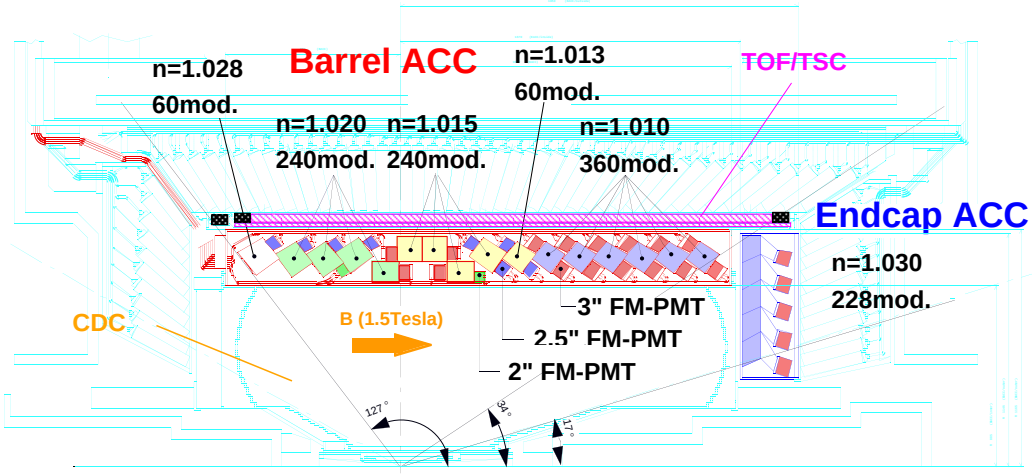

Figure 3.9: The configuration of the Aerogel Čerenkov Counter.

in 5 concentric layers.

Each module contains a silica Aerogel counter connected to a fine–mesh photomultiplier tube (FMPMT) by an air lightguide. The FMPMTs can operate inside the 1.5 T magnetic field.

Figure 3.10 demonstrates the efficiency for correctly identifying kaons and the false identification rate of pions in the barrel region for tracks in the momentum range 0.5 to 4.0 GeV/c. For most of this range the measured kaon efficiency is greater than 80%, while the pion fake rate is less than 10%.

3.2.4 Time of Flight counter (TOF)

For particles in the intermediate momentum range of 0.8 to 1.2 GeV/c the most effective means of particle identification is to measure the time it takes for the particle to travel a certain distance. This provides a direct measurement of the velocity of the particle, which, when combined with the momentum measured by the CDC (§3.2.2) can be used to determine the mass of the particle. The TOF is used to measure the time between a collision at the IP and the moment at which a particle hits one of the scintillation counters in the TOF. It is also used as part of the Belle trigger system.

The TOF system consists of 128 TOF counters and 64 Trigger Scintillation Counters (TSCs). Two TOF counters and one TSC form a module, with a 1.5 cm radial gap, as in figure 3.11. 64 TOF/TSC modules, located at a radius of 1.2 m, cover a polar angle range of $34°$ to $120°$ in the barrel region of Belle. TOF

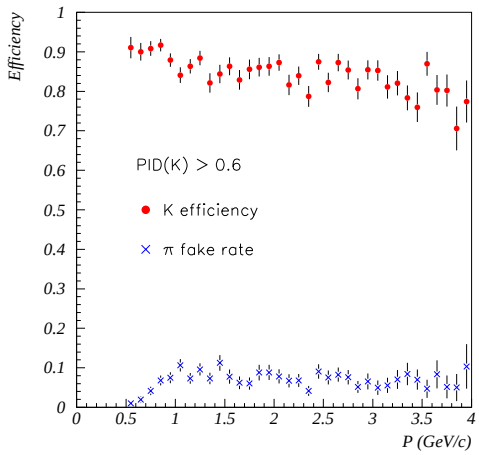

Figure 3.10: Kaon efficiency and pion fake rate, measured with $D^{*+} \rightarrow D^0(K\pi) + \pi^+$ decays, for the barrel region of the ACC.

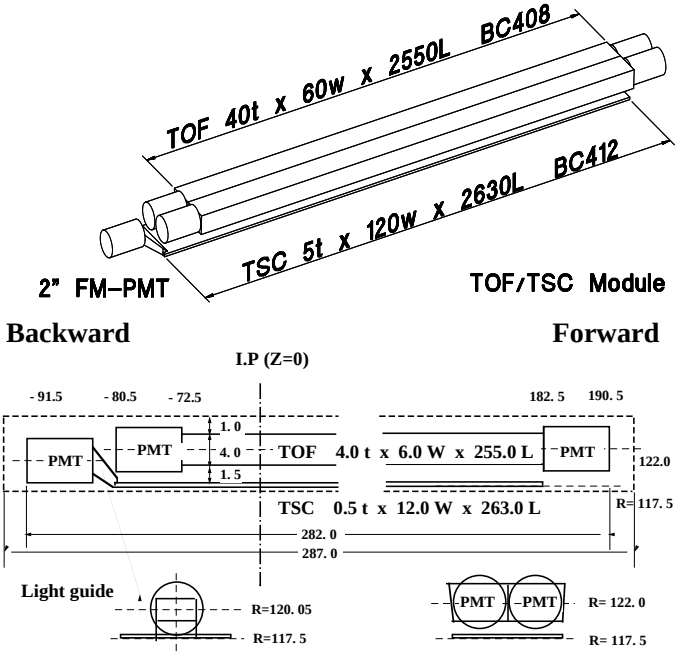

Figure 3.11: Dimensions of a TOF/TSC module.

counters are read out by two FMPMTs, while each TSC is read out by one FMPMT at each end.

The time resolution of the TOF is 100 ps, which implies approximately three standard deviation (3σ) kaon/pion separation at 1.25 GeV/c. Since the TOF is mounted on the inside of the ECL at a radius of approximately 1.2 m, particles with a transverse momentum less than 0.54 GeV/c curl around on themselves before making it as far as this subdetector. The mass distributions for pions, kaons, and protons, as measured by the TOF is shown in figure 3.12(a). The ability of the TOF to distinguish between kaons and pions is shown in figure 3.12(b) as a function of the particle's momentum.

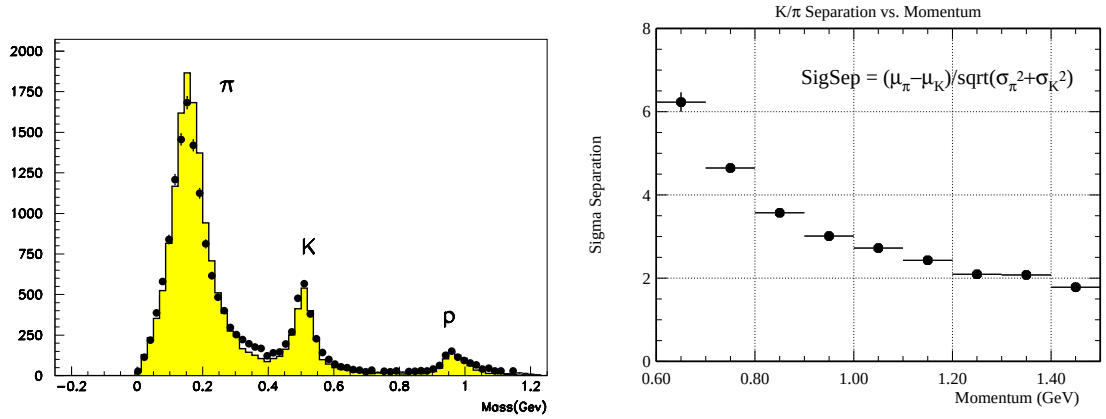

(a) Mass distribution from TOF measurements for particle momenta below 1.2 GeV/c.

(b) K/π separation performance of the TOF as a function of momentum.

Figure 3.12: Time of Flight counter performance.

3.2.5 Electromagnetic Calorimeter (ECL)

The ECL contains 8,736 Cesium Iodide crystals which are doped with Thallium (CsI(Tl)). When a charged or neutral particle travels through a crystal it loses energy. The crystal emits photons at a rate proportional to the energy loss, and thus the particle generates a shower of electromagnetic particles. The CsI crystals are doped with Tl in order to shift the wavelength of the photons in the electromagnetic showers into the visible spectrum so that the showers may be detected by the two photodiodes attached to the back of each crystal.

This subdetector is the principal means of detection of photons, which, in common with electrons, deposit most of their energy in an electromagnetic shower as they travel through the ECL. Electron identification relies primarily on a comparison of the charged particle momentum and the energy deposits in the

ECL, although ionisation energy losses in the CDC are also taken into account.

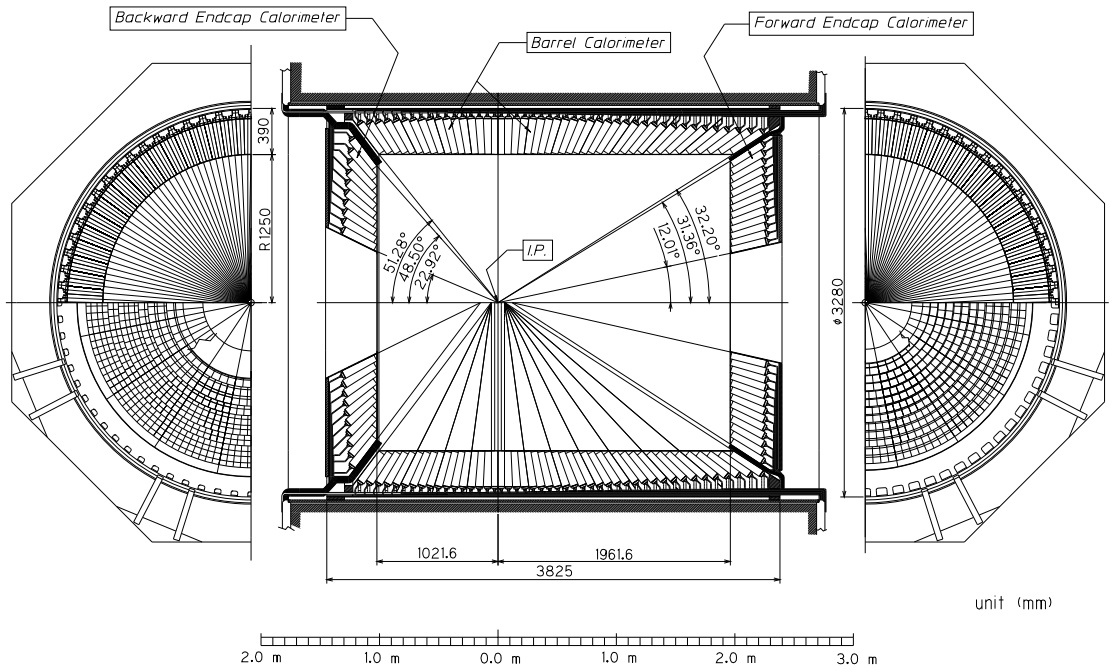

Figure 3.13: The Electromagnetic Calorimeter.

Each crystal has a tower like shape, and is arranged so that it points almost directly towards the IP, as shown in figure 3.13. There is a small tilt of $\sim 1.3^\circ$ in the θ and ϕ directions to avoid photons escaping through the gap between crystals. The size of the crystals is determined by the design condition that 80% of the energy deposited by a photon injected at the centre of a crystal should remain contained in that crystal. Crystals in different parts of the detector have different dimensions, but a typical crystal in the barrel region has a front face of $55\ \mathrm{mm} \times 55\ \mathrm{mm}$ and a rear face of $65\ \mathrm{mm} \times 65\ \mathrm{mm}$. Each crystal is $30\ \mathrm{cm}$ long, corresponding to over 16.2 radiation lengths for photons and electrons. This avoids shower leakage from the rear of the crystal at high energies.

The photon energy resolution of the ECL has been measured to be

$$\left(\frac{\sigma_E}{E}\right)^2 = 0.0134^2 + \left(\frac{0.00066}{E}\right)^2 + \left(\frac{0.0081}{E^{1/4}}\right)^2, \tag{3.5}$$

and the position resolution is

$$\sigma_{\mathrm{pos}} = \frac{0.5\ \mathrm{cm}}{\sqrt{E}}, \tag{3.6}$$

where E is measured in GeV.

3.2.6 K_L/μ Detector (KLM)

As its name suggests, the KLM's purpose is to detect K_L mesons and identify muons. Since muons have a relatively small interaction cross section they penetrate further through the Belle detector than most of the particles coming from the IP. Any track that penetrates several layers of the KLM after leaving a track in the CDC is almost certainly a muon, and is identified accordingly. In addition, the neutral K_L meson, which does not interact with any of the subdetectors closer to the IP, is identified when it is stopped by the 3.9 nuclear interaction lengths of iron contained in the KLM. Hits in the KLM without an associated charged track in the CDC are assumed to be from K_L mesons.

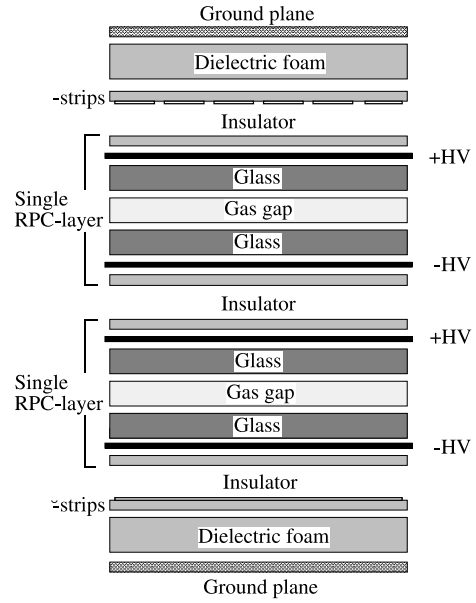

Figure 3.14: Cross section of a KLM superlayer.

The KLM consists of alternating layers of charged particle detectors and $4.7\ \mathrm{cm}$ thick iron plates. There are 15 detector layers and 14 iron layers in the octagonal barrel region, and 14 detector layers in each of the forward and backward end–caps. Each detector layer is a super–layer of glass–electrode resistive plate counters (RPCs). A detector super–layer consists of two RPCs, as shown in figure 3.14, which provide θ and ϕ hit information. In the barrel part of the detector an additional RPC superlayer is placed in front of the first iron plate. Figures 3.15(a) and 3.15(b) show barrel and endcap RPCs.

Each super–layer is read out through orthogonal strips, each of which is typically $5\ \mathrm{cm}$ wide, which provide ϕ and z information in the barrel region, and θ and ϕ in the endcaps. The 240 modules in the barrel region cover a polar angle region of 45° to 125°. This is extended to 20° to 155° by the 112 endcap modules.

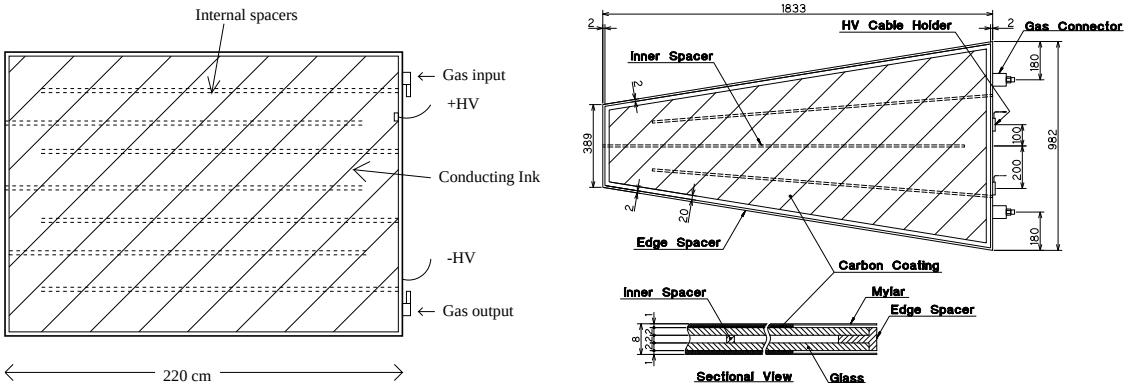

(a) Barrel RPC.

(b) Endcap RPC.

Figure 3.15: KLM RPCs.

3.2.7 Extreme Forward Calorimeter (EFC)

The EFC supplements the ECL by extending the polar angle coverage for calorimetry in the forward region to $6.4^\circ < \theta < 11.5^\circ$, and to $163.3^\circ < \theta < 171.2^\circ$ in the backward region. Its placement on the front faces of the solenoid magnet cryostats, and around the beam pipe allows it to function as a beam mask to reduce background radiation reaching the CDC. In addition it acts as a beam monitor for KEKB control and as a luminosity monitor for the Belle experiment.

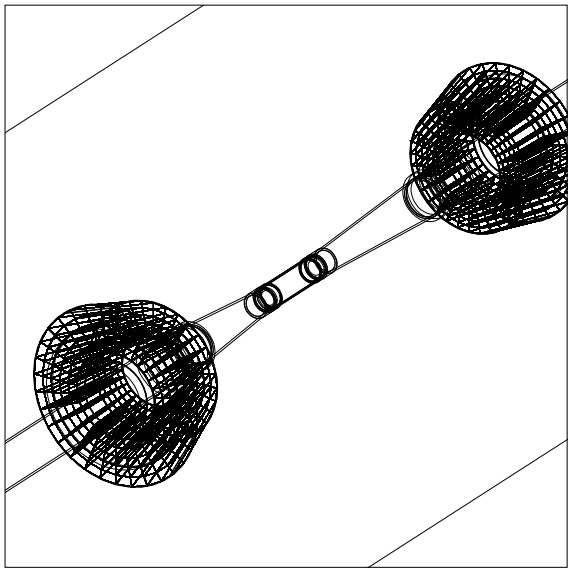

Figure 3.16: The Extreme Forward Calorimeter.

Since the EFC is in an area subject to high levels of radiation, it was constructed from Bismuth Ger-

manate (BGO) crystals which can withstand megarads of radiation, and which also provide good energy resolution. Figure 3.16 depicts the manner in which each tower shaped crystal faces inwards towards the IP.

3.2.8 Solenoid Magnet

All the subdetectors interior to the KLM are enveloped in a near uniform[1] 1.5 T magnetic field created by a superconducting solenoid magnet. The iron plate structure of the KLM serves as a return yoke for the magnetic field. The solenoid is summarised in table 3.2.

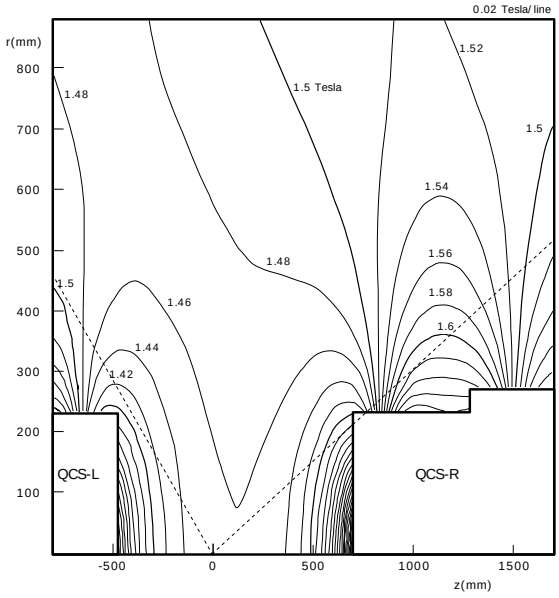

Figure 3.17: Contour plot of the measured magnetic field in the Belle detector.

3.3 Trigger and Data Acquisition System

The trigger system selects which events to write to tape and which events to discard. It combines information from all the detectors to eliminate as much background as possible from events such as beam–gas interactions, where electrons or positrons from the beam interact with remnant gas molecules in the beam pipe, or from other sources such as synchrotron radiation. The rate of background events is highly dependent on the conditions of the accelerator, such as the beam current and pressure, but the combined rate of all such background is typically around the order of hundreds of megahertz. The trigger is designed

[1] Figure 3.17 shows the field strength as function of z for various radii

Cryostat		
	Inner Radius	$1.70\ \mathrm{m}$
	Outer Radius	$2.00\ \mathrm{m}$
Central field		$1.5\ \mathrm{T}$
Length		$4.41\ \mathrm{m}$
Coil		
	Effective radius	$1.8\ \mathrm{m}$
	Length	$3.92\ \mathrm{m}$
	Superconductor	NbTi/Cu
	Nominal current	$4400\ \mathrm{A}$
	Inductance	$3.6\ \mathrm{H}$
	Stored energy	$35\ \mathrm{MJ}$
	Typical charging time	$0.5\ \mathrm{h}$

Table 3.2: Parameters of the solenoid coil.

to be flexible enough to cope with unexpectedly high levels of background events, yet at the same time, maximise the number of hadronic events stored.

The trigger conditions are multiply redundant, in order to cope with the many and various types of events we are trying to keep. The trigger system has four levels: two hardware – the level 0 and level 1 triggers; and two software – the level 3 and level 4 triggers.

The level 0 trigger is a timing signal from the TOF that issues a hold to the SVD.

The level 1 trigger combines trigger information from each of the subdetectors into the Global Decision Logic (GDL), as in figure 3.18. The subdetector trigger systems can be categorised as track triggers or energy triggers. The tracking trigger utilises the $r-\phi$ and z trigger from the CDC, the TOF trigger, and a count of the number of isolated hit clusters in the ECL. The energy trigger requires the aggregate energy deposited in the ECL to exceed $1\ \mathrm{GeV}$. If the event satisfies the criteria of the GDL a readout of the hits stored in all the subdetectors is performed.

The level 3 trigger performs a simple, fast reconstruction of the event to avoid unnecessarily writing to tape any junk events which pass the level 1 trigger.

The level 4 trigger occurs after the events have been stored. It further filters events before a full reconstruction using the offline computer farm is performed.

The exact conditions of the trigger vary from run to run, in accordance with changes to the KEKB operating conditions, and updates to the trigger system itself.

During data taking the condition of each subdetector is closely monitored with the aid of the Data Quality Monitor (DQM). This is part of the DAQ system, shown in figure 3.19, which controls the flow of data from the subdetector subsystems up until the point it is written to tape.

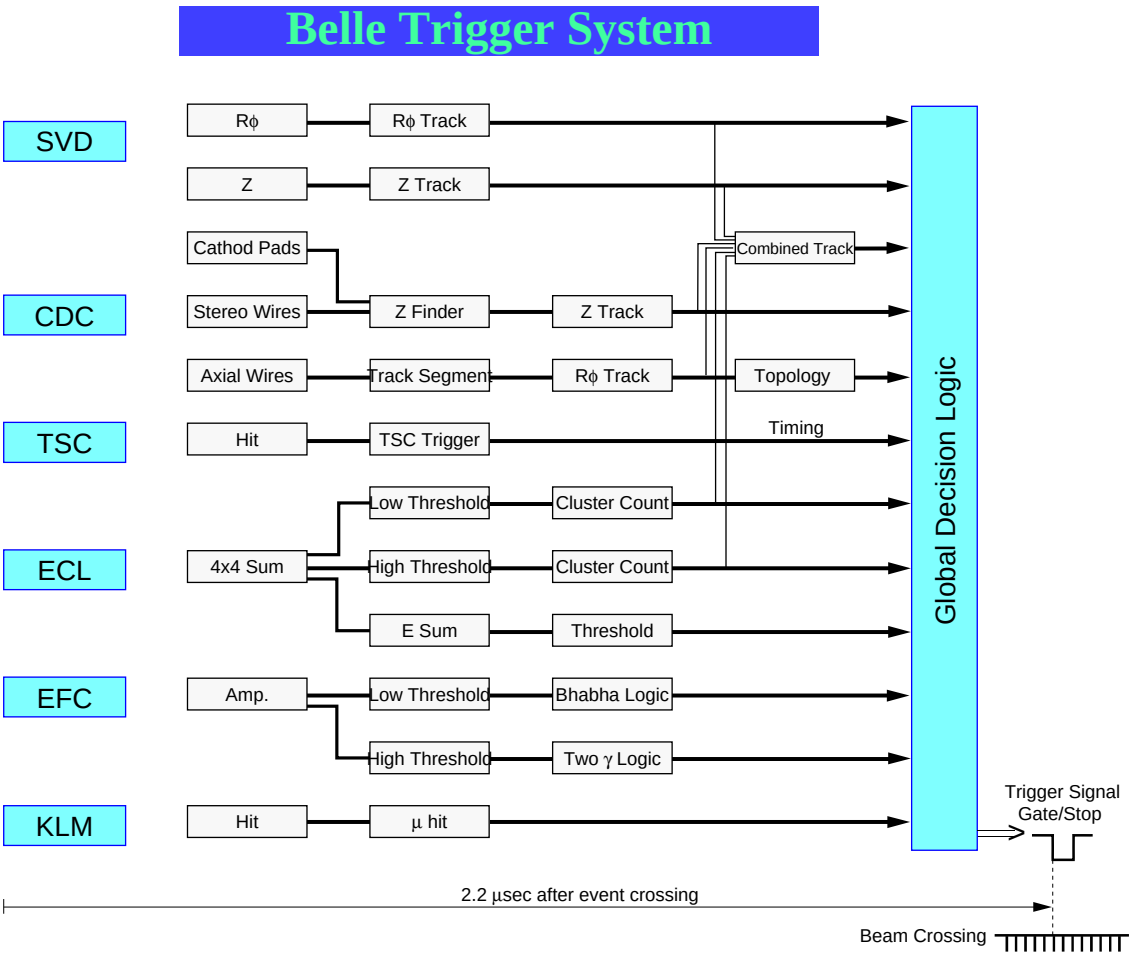

Figure 3.18: Overview of the Belle trigger system.

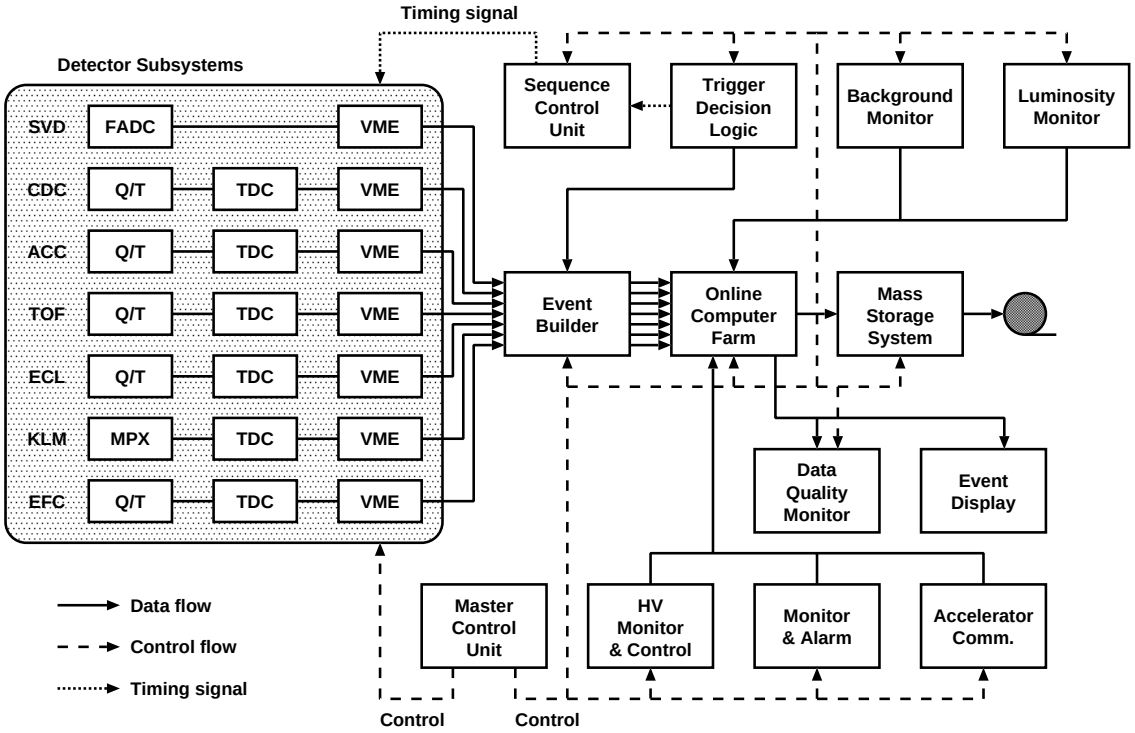

Figure 3.19: The Belle DAQ system.

Events which have passed the final trigger level and have been placed in the Mass Storage System are later processed offline with software that analyses the hit information from each subdetector and calculates the four–momentum of particles which have travelled through the detector. As advances in the tracking and other algorithms are made, this software is updated and the data is reprocessed.

3.4 Simulation

The behaviour of the Belle detector is modelled by Monte–Carlo simulation with a suite of software utilities, and is normally performed in three stages: generation; detector simulation; and reconstruction.

Simulation of the decay of the B mesons and other particles in each event is done by the `QQ98` event generator [84, 85], which was originally developed by the CLEO collaboration. Parameters such as the electron energy, positron energy, and collision angle are input to the event generator. Using these parameters a virtual photon to $B\bar{B}$ pair event is generated. The decay of these mesons via various user defined decay paths is then modelled, with `QQ98` determining the four–momenta of the intermediate and final state particles. This information is passed to the simulation stage software, which then simulates the transit of these particles through the detector. The decay of some particles which have a long lifetime, such as the K_S meson, are not modelled using `QQ98`, but rather are left to the detector simulation software to calculate.

The detector's geometry is modelled using `GEANT` [86]. The software modules which individually model the performance of each subdetector are collectively referred to as `GSIM`. The simulation stage creates data that mimics the output from the DAQ, so the same reconstruction software that is used to process experimental data is used for the Monte–Carlo data. The effect of backgrounds from beam–gas interactions, and other such events which are not directly related to the $e^+ e^-$ collision, is replicated using data accumulated when the KEKB accelerator was operating, but with random trigger conditions. This technique is used to create Monte–Carlo events which mimic the performance of the Belle detector on a run by run basis.

Chapter 4

Reconstruction technique

A full reconstruction of the decays $B^0 \to D^0 D^{*-} K^+$, $B^+ \to D^{*+} D^{*-} K^+$ and $B^0 \to D^{*+} D^{*-} K_S$ was performed using data collected by the Belle detector. The momentum of charged tracks and the energy of photon candidates is reconstructed and stored in Mini Data Summary Tape (`MDST`) tables [87]. These tables contain vectors of three–momenta for all the track candidates in each event detected by Belle.

Generally only the final state kaons, pions and photons leave traces in the detector for $B \to DDK$ decays . The intermediate K_S, D^0 and D^* mesons are reconstructed by summing the momenta of the various final state particles to form four–momentum vectors. Candidates are identified by searching for signal peaks in various discriminating spectra, such as invariant mass distributions, which are created from the reconstructed momentum vectors.

In this analysis neutral kaons are searched for via the mode $K_S \to \pi^+ \pi^-$. D^0 mesons decaying to $K\pi$, $K\pi\pi^0$ and $K\pi\pi\pi$ final states are reconstructed, where the neutral pion decays to two photons. D^* candidates are formed from summing the four–momenta of the D^0 meson candidates with that of tracks which are identified as low momentum pions.

Finally, B meson candidates are formed by adding the four–momenta of these intermediate charmed and strange mesons in the combinations mentioned above. The full reconstruction of $B^0 \to D^0 D^{*-} K^+$ also allows for a partial reconstruction of $B^0 \to D^{*0} D^{*-} K^+$ decays.

4.1 Data Set

This analysis is performed on data collected by the Belle detector between January 2000 and July 2002. In this time $78.13\ \mathrm{fb}^{-1}$ of data was accumulated at the $\Upsilon(4S)$ resonance. A further $8.83\ \mathrm{fb}^{-1}$ of data was collected at an energy just below this, in order to characterise the background from non $\Upsilon(4S)$ events. The rate at which this data set was amassed is demonstrated in figure 4.1

During this interval data was taken in seven different experiments, each with slightly different accel-

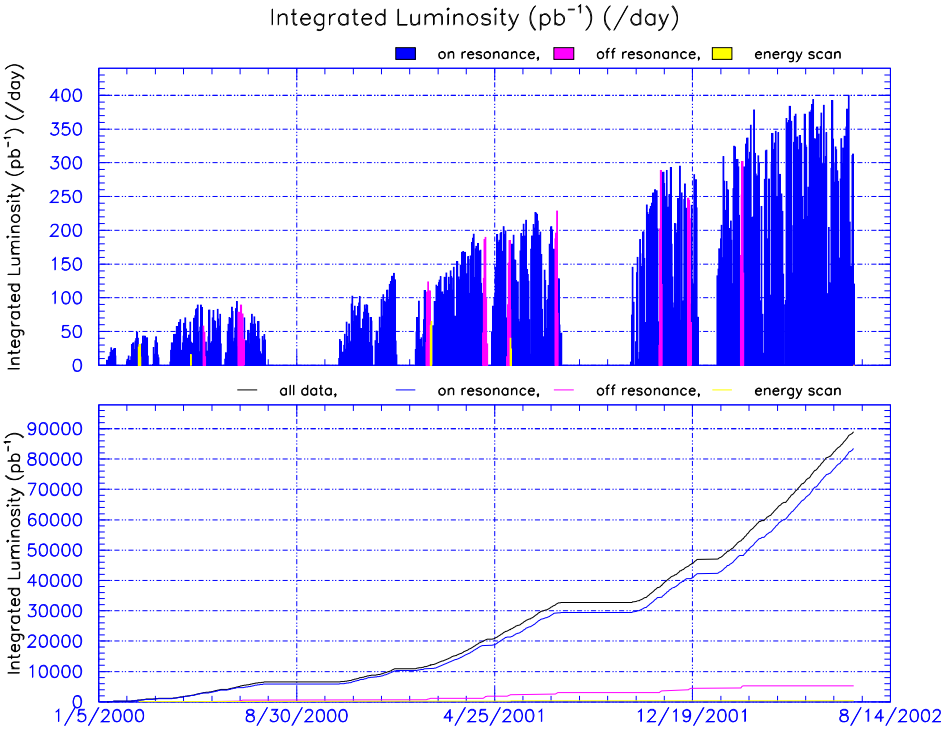

Figure 4.1: Integrated luminosity: per day (top) and as a function of day (bottom).

erator conditions. The convention within the Belle collaboration is to refer to experiments where data is accumulated at the $\Upsilon(4S)$ resonance with an odd number. Experiments which are used to calibrate the detector, for instance with the collection of cosmic ray events, are given an even number. The following analysis is performed on experiments 7, 9, 11, 13, 15, 17 and 19.

Most of the selection criteria described in this chapter were chosen from an analysis of a select number of runs in experiment 15, but are applied to events from all experiments. While accelerator conditions vary between experiments and runs, they do not do so to such an extent to invalidate these criteria. As well as being undesirable, it would also be a practical impossibility to have selection cuts tuned for each individual experiment or run period. A run is normally equivalent to the data accumulated during one fill of the LER and HER. However, if there are any DAQ errors which interrupt data taking there may be more than one run per fill.

4.2 Hadronic event selection

Many types of events pass the triggering system described in §3.3. Events from e^+ e^- interactions could be any of $e^+e^- \to u\bar{u}$, $d\bar{d}$, $s\bar{s}$, $b\bar{b}$, e^+e^-, $\mu^+\mu^-$, $\tau^+\tau^-$, $e^+e^-\gamma$, or 2 photons. Beam background events may also be recorded. These typically come from interactions between either the e^+ or e^- beam with residual gas particles in the beam pipe.

A general set of criteria for a hadronic skim is used for most analyses in the Belle collaboration, including this one. The `HadronB` [88] skim criteria are chosen to maximise the $B\bar{B}$ selection efficiency, minimise the number of non–hadronic events, and provide a reasonably high efficiency for $e^+e^- \to q\bar{q}$ events, where $q = u, d, s$, or c. The latter type of events are known as continuum events since they are distributed continuously below the $\Upsilon(4S)$ peak of figure 3.2.

The `HadronB` criteria are:

- The number of *good* charged tracks,

$$N_{\rm trk} \geq 3, \tag{4.1}$$

  where a good charged track is one where $p_t > 0.1$ GeV/c, $|dr| < 2.0$ cm, and $|dz| < 4.0$ cm. In this case $|dr|$ and $|dz|$ are the distance of closest approach between the track and the z–axis or the z–position of the nominal IP respectively.

- The distance between the primary event vertex and the origin of the detector co–ordinate system satisfies

$$|r| < 1.5 \text{ cm, and } |z| < 3.5 \text{ cm}, \tag{4.2}$$

  where the primary event vertex is determined from all the good charged tracks.

- The sum of the *good* cluster energies in the ECL meets the condition

$$0.18 \leq E_{\rm sum}/\sqrt{s} \leq 0.80, \tag{4.3}$$

  where a good cluster is one with $E > 0.1$ GeV.

- The total visible energy detected by the CDC and ECL, which is the sum of the good track momenta and good photon energies, is

$$E_{\rm vis} \geq 0.20\sqrt{s}. \tag{4.4}$$

  Good photons candidates are selected from good ECL clusters which do not have associated good tracks.

- The sum of the z–components of the good tracks and good photon momenta is balanced around zero, such that

$$\left|\sum p_z\right| \leq 0.5\sqrt{s}. \tag{4.5}$$

- There are at least two ECL clusters in the barrel region of the detector.

- The average cluster energy meets the condition

$$E_{\rm sum}/n_{\rm ECL} < 1 \text{ GeV}, \tag{4.6}$$

  where $n_{\rm ECL}$ is the calorimeter cluster hit multiplicity.

- The Heavy Jet Mass, $M_{\rm jet}$, satisfies

$$M_{\rm jet} > 0.25E_{\rm vis} \quad \text{or} \quad M_{\rm jet} > 1.8 \text{ GeV}/c^2. \tag{4.7}$$

  To calculate $M_{\rm jet}$ the event is divided into two hemispheres by a plane perpendicular to the event thrust axis. The invariant mass of the sum of all the tracks in each hemisphere is then determined, assuming a pion mass hypothesis for each track. The larger of the two invariant masses is the Heavy Jet Mass.

These selection criteria are more than 99% efficient for $B\bar{B}$ events and contain a non–hadronic component less than 5%.

4.3 Candidate event selection

To observe the decay $B^0 \to D^{*+}\bar{D}^0K^-$ at least six charged tracks must be detected by Belle. Similarly, reconstructions of $B^+ \to D^{*+}D^{*-}K^+$ and $B^0 \to D^{*+}D^{*-}K_S$ decays require the presence of at least

seven and eight charged tracks respectively. These requirements eliminate a significant number of `HadronB` events.

Selection of continuum events of the type described in §4.2 is suppressed through the use of the Fox–Wolfram moments [89]. These are defined as

$$H_l = \sum_{i,j} \frac{|\vec{p_i}||\vec{p_j}|}{E_{\rm vis}^2} P_l(\cos\phi_{ij}), \tag{4.8}$$

where the indices i and j run over the tracks produced in the event, ϕ_{ij} is the angle between particles i and j, and $P_l(x)$ is the Legendre polynomial of order l. The Fox–Wolfram moments are usually normalised to H_0.

The second normalised Fox–Wolfram moment, $R_2 = H_2/H_0$, is commonly used for continuum suppression. For events with spherical topology, such as $\Upsilon(4S) \rightarrow B\bar{B}$ decays, R_2 tends towards zero. Jet–like events, such as continuum decays where the final state particles are produced with significant energies, are inclined to higher values of R_2.

Figure 4.2 demonstrates the shape of R_2 for $B^0 \rightarrow D^0 D^{*-} K^+$ decays in signal Monte–Carlo (MC) events. This distribution is concentrated in lower values of R_2, in contrast with the shape for continuum events shown in the hatched histogram in the same figure. Events where $R_2 > 0.4$ are rejected to reduce any continuum background, but still maintain high signal efficiency.

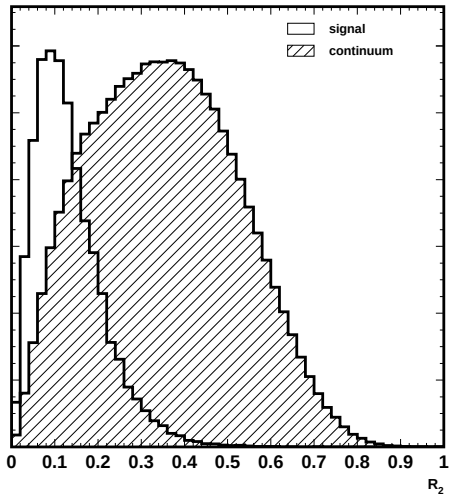

Figure 4.2: The second normalised Fox–Wolfram moment for $B^0 \rightarrow D^{*+}\bar{D}^0 K^-$ signal MC and continuum events.

4.4 The number of $B\bar{B}$ events

Data collected at the $\Upsilon(4S)$ resonance consists of $B\bar{B}$ and $q\bar{q}$ events in a ratio of roughly 1 to 3[1]. The number of $B\bar{B}$ events, $N(B\bar{B})$, in the `HadronB` sample is estimated [90] by examining the second normalised Fox–Wolfram moment.

The R_2 distribution for $q\bar{q}$ events is determined from data taken at energies below the $\Upsilon(4S)$ resonance. The equivalent shape for $B\bar{B}$ events is measured from a study of Monte–Carlo $B\bar{B}$ events. By fitting the R_2 distribution of data taken at the $\Upsilon(4S)$ resonance with these two shapes it is possible to estimate the relative proportions of these types of events in the `HadronB` sample.

However, vastly more on–resonance data is collected than off resonance data, and the accelerator conditions are different for each situation. This leads to an error in the calculation of $N(B\bar{B})$. The number of $B\bar{B}$ events in each experiment is detailed in table 4.1.

	$N(B\bar{B})$				
experiment 7	$6,468,729$	$\pm$	$161,468$		
experiment 9	$4,759,695$	$+$	$28,616$	$-$	$47,326$
experiment 11	$8,850,938$	$+$	$51,679$	$-$	$51,776$
experiment 13	$11,699,795$	$+$	$198,491$	$-$	$198,443$
experiment 15	$13,567,937$	$+$	$96,293$	$-$	$105,499$
experiment 17	$12,458,801$	$+$	$330,115$	$-$	$330,113$
experiment 19	$27,170,503$	$+$	$313,808$	$-$	$313,762$
total	$84,966,397$	$+$	$491,041$	$-$	$495,171$

Table 4.1: Number of $B\bar{B}$ events in each experiment.

4.5 Track selection

Charged tracks are detected primarily by the CDC (§3.2.2). Hit information from the axial wires is used to project tracks in the $r-\phi$ plane, then hits in the stereo wires are used to determine the z trajectory of the track and all the hits are parameterised in a helix to calculate the momentum of the track [91]. These tracks are then matched with hits in the SVD and the momentum is refitted using the Kalman filter algorithm. The tracks are then extrapolated to the outer detectors using a Runge–Kutta method [92].

A limitation of the above is the use of a helix parameterisation [93] as a track model. This method is valid for a uniform magnetic field, but as figure 3.17 demonstrates, the field in the forward and backward regions of the Belle detector is quite non–uniform. This can lead to shifts in the mass peaks of reconstructed particle candidates. Correction factors for track momenta in each experiment are determined from studies of well measured invariant mass peaks, and are applied with the use of the `fix_mdst` software module.

[1] In addition there are the background events described in 4.2, which are also dealt with in the estimation of $N(B\bar{B})$.

Poorly reconstructed tracks are rejected by imposing cuts on the shortest distance between each track's trajectory and the IP. This distance projected onto the $x - y$ plane is dr, and the distance in z is dz. Distributions of the impact parameters, dr and dz, for experiment 15 are shown in figures 4.3(a) and 4.3(b) respectively.

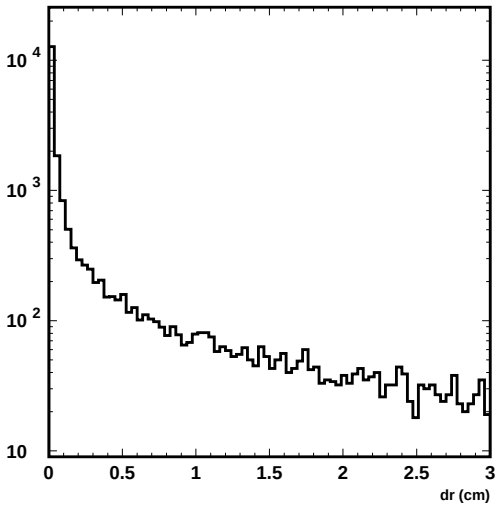

(a) dr distribution for charged tracks.

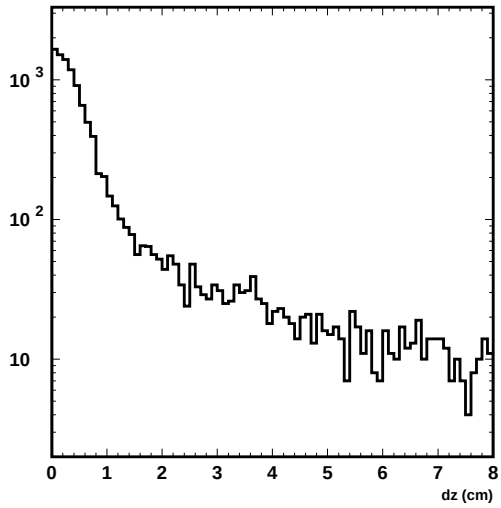

(b) dz distribution for charged tracks.

Figure 4.3: Charged track impact parameters for experiment 15.

All tracks used to reconstruct B meson candidates, except for slow pion candidates from the $D^{*\pm} \to D^0\pi_s^\pm$ decay, must satisfy

- $|dr| < 0.4$ cm, and
- $|dz| < 5.0$ cm.

These cuts are more generous than might normally be applied, but since all the final state particles in doubly charmed B meson decays at the $\Upsilon(4S)$ resonance have relatively low momentum the tracking quality tends to be poor. These criteria were chosen to eliminate only the most dubious tracks detected by Belle.

4.6 Charged particle identification

Separation of charged kaons and pions is the only form of particle identification used in this analysis. In the Belle detector this is performed by the ACC, TOF and CDC, and is implemented in the `atc_pid` software module [94].

Each of the subdetectors used for kaon and pion separation is most effective for particle identification in different momentum ranges, and their measurements are nearly independent. Information from these three subdetectors is combined using a likelihood method to form a single variable which is used to discriminate between kaon and pion candidates.

Particle identification using `atc_pid` is based on the probability of the detector response being consistent with the passage of a hypothesised signal particle type, compared to the probability that the same response is due to the passage of a given background type of particle. This is expressed as a likelihood ratio

$$\mathcal{P}(i:j) = \frac{P_i}{P_i + P_j}, \tag{4.9}$$

where P_i is the likelihood calculated for the signal particle type, and P_j is the likelihood for the background particle type. The variables i and j range over five particle types, e, μ, π, K and p.

Each likelihood, P_i, in equation 4.9 is a combination of likelihoods from the three subdetectors,

$$P_i = P_i^{dE/dx} \times P_i^{\mathrm{TOF}} \times P_i^{\mathrm{ACC}}, \tag{4.10}$$

which are calculated as follows:

dE/dx A χ^2 value for each particle hypothesis is calculated as

$$\chi^2 = \left(\frac{(dE/dx)_{\mathrm{measured}} - (dE/dx)_{\mathrm{expected}}}{\sigma_{dE/dx}} \right)^2, \tag{4.11}$$

where $(dE/dx)_{\mathrm{measured}}$ and $(dE/dx)_{\mathrm{expected}}$ are the measured and expected values of dE/dx respectively, and $\sigma_{dE/dx}$ is the expected resolution. A likelihood is calculated assuming a Gaussian distribution

$$P = \frac{e^{-\frac{1}{2}\chi^2}}{\sqrt{2\pi}\sigma_{dE/dx}}. \tag{4.12}$$

TOF A χ^2 value from TOF hit information is calculated by observing the time interval between hits in the two phototubes of a counter and comparing this with the time the hypothesised particle type should take to travel through the detector. The likelihood is

$$P = \frac{e^{-\frac{1}{2}\chi^2}}{\prod_{i=1}^{\mathrm{ndf}} \sqrt{2\pi}\sigma_i}, \tag{4.13}$$

where ndf is the number of PMT time intervals included in the determination of χ^2.

ACC As discussed in §3.2.3 the ACC is a threshold device, so it acts as an on/off detector. The observed signal, the number of photo–electrons, N_{pe}, is either zero or a small number. The ACC is treated rather simply by `atc_pid` – the likelihood is given by comparing the observed N_{pe} with a threshold

value, N_{pe}^{th}, using the expected efficiency, ϵ, at the measured momentum:

$$P = \quad \epsilon \quad (N_{pe} \geq N_{pe}^{th}) \tag{4.14}$$

$$P = \quad 1-\epsilon \quad (N_{pe} \leq N_{pe}^{th}). \tag{4.15}$$

The threshold value and the momentum dependent expected efficiencies for the various particle types are determined from MC studies and are referenced from lookup tables.

If one of the subdetector elements cannot positively identify the candidate track it will return a likelihood of 0.5. The distribution of $\mathcal{P}(K:\pi)$ in experiment 15 is shown in figure 4.4, where a small bump reflecting this default assignment can be seen at $\mathcal{P}(K:\pi) = 0.5$.

Particle identification using `atc_pid` is performed on all tracks used in the event reconstruction, except for those tagged as low momentum pion candidates. If $\mathcal{P}(K:\pi) > 0.1$ the track is identified as a kaon, if $\mathcal{P}(K:\pi) < 0.9$ the track is identified as a pion. Thus the K/π separation is not mutually exclusive, and care must be taken not to use the same track twice in the reconstruction. The prompt kaon candidates, which come directly from the B meson, are subject to the more stringent condition $\mathcal{P}(K:\pi) > 0.2$.

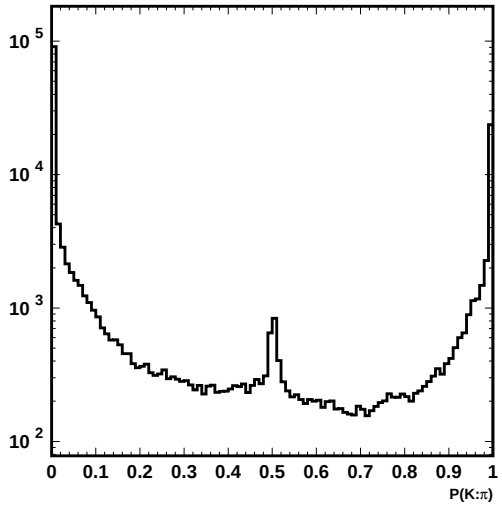

Figure 4.4: $\mathcal{P}(K:\pi)$ for charged tracks in experiment 15.

4.7 Kinematic fitting

The momentum resolution of candidates for the intermediate particles produced in the B meson decay can be improved by kinematically fitting the vertex locations of their decay products. If, for example, a D^0 meson decays to a $K\pi$ final state, then the momentum of the D^0 meson candidate, which in the first

instance is the vector sum of the kaon and pion momenta, can be refitted by requiring that both the kaon and pion were produced at the same geometric location. In addition, by assuming a D^0 mass hypothesis for the sum of the two final state momenta and refitting the D^0 candidate's momentum, the momentum resolution of any reconstructed particle made from the D^0 will be improved as well.

Kinematic fitting is implemented by the `kfitter` software module [95] which performs three main functions:

geometric vertexing fitting where a χ^2 value of the geometric fit is returned;

mass constrained fitting where the momentum of the mother candidate is refitted assuming the specified mass hypothesis; and

mass constrained vertex fitting where the daughter particles are constrained to originate from a common vertex location, and the momentum of the mother particle is refitted.

The fitting algorithm, described in detail elsewhere [96], is based on an iterative least square method using the Lagrange multiplier method.

4.8 Neutral pion selection

Photon candidates are reconstructed from 5×5 crystal hit clusters in the ECL. Only photon candidates with energies greater than $30\ \mathrm{MeV}$ are combined to form neutral pion candidates. In order to reduce combinatorial background only pion candidates with a momentum greater than $200\ \mathrm{MeV}/c$ are selected.

After these selection criteria have been applied the resolution of the signal peak in the invariant mass spectrum is determined and a three standard deviation (3σ) cut is made around the mean value. The resolution is determined to be $4.78\ \mathrm{MeV}/c^2$. The invariant mass spectrum shown in figure 4.5 is taken from runs 600 to 617 of experiment 15, as are all the following invariant mass spectra unless otherwise specified. The mass cut applied is $123 < m(\gamma\gamma) < 147\ \mathrm{MeV}/c^2$. Neutral pion candidates are mass constrained vertex fitted. However, since the origin of the photon candidates is not known the error of the vertex location is assigned a large value in the fit.

Figure 4.6 shows the neutral pion candidate invariant mass spectrum for signal Monte–Carlo generated to simulate experiment 15 conditions.

4.9 Short lived neutral kaon selection

K_S meson candidates are selected from combinations of oppositely charged pions. No particle identification cut is applied to these final state pions. All candidates are selected according to the `goodKS_loose` cuts of [97] which are also described below.

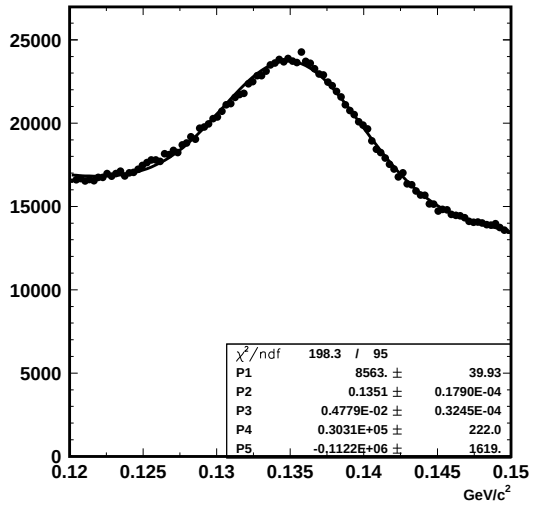

Figure 4.5: The invariant mass spectrum for neutral pion candidates. This spectrum is from runs 600 to 617 in experiment 15.

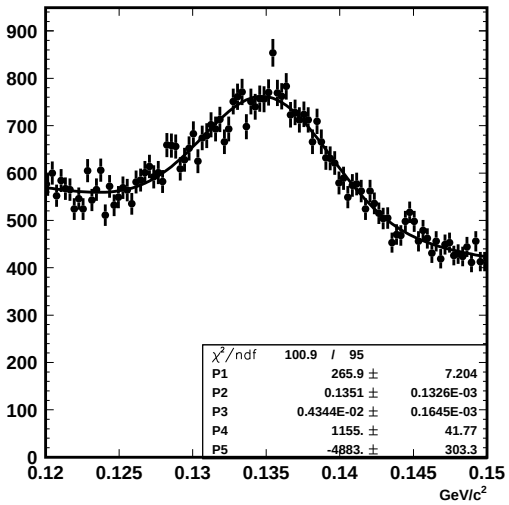

Figure 4.6: The invariant mass spectrum for neutral pion candidates in signal MC.

Reconstructed K_S meson candidates are categorised according to how many of the daughter pions recorded hits in the SVD:

1. Both daughter tracks have associated SVD hits.
2. Only one daughter track has associated SVD hits.
3. Neither daughter track has an associated SVD hit.

Candidates are then subjected to the cuts of table 4.2, where $d\phi$ is the angle in the $x-y$ plane between the momentum vector and the decay vertex vector of the K_S candidate, z_{dist} is the shortest distance between the two daughter tracks, and F_l is the flight length of the K_S candidate in the $x-y$ plane.

Momentum (GeV)	dr (cm)	$d\phi$ (rad)	z_{dist} (cm)	F_l (cm)
< 1.5, Category 1	> 0.03	< 0.35	< 2.0	> 0.08
< 1.5, Category 2	> 0.10	< 0.40	< 40	< 9.0
< 1.5, Category 3	> 0.10	< 0.05	< 6.5	> 1.5
> 1.5	> 0.03	< 0.10	< 15	$-$

Table 4.2: The `goodKS_loose` cuts of [97].

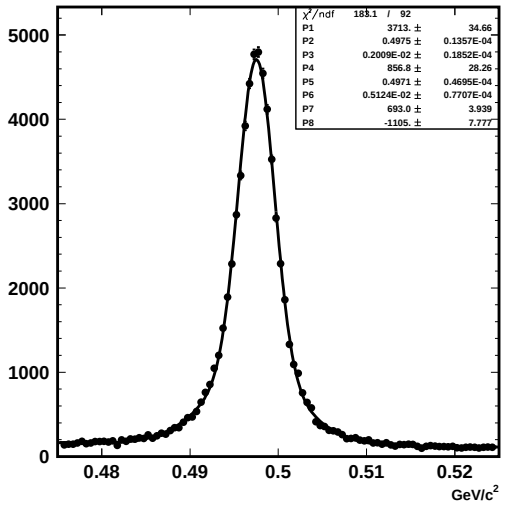

Figure 4.7: The invariant mass spectrum for K_S candidates after the `goodKS_loose` cuts have been applied. This spectrum is from runs 600 to 617 in experiment 15.

The resulting K_S invariant mass spectrum of figure 4.7 is then fitted with a double Gaussian. A 3σ cut is applied using the width of the wider Gaussian, $5.12\ \mathrm{MeV}/c^2$. In comparison, figure 4.8 shows the resulting spectrum after these cuts have been applied to experiment 15 signal MC.

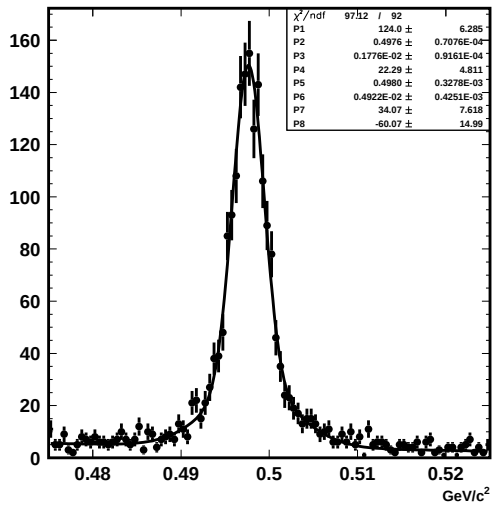

Figure 4.8: The invariant mass spectrum for K_S candidates after the `goodKS_loose` cuts have been applied for signal MC events.

4.10 D^0 meson reconstruction

D^0 meson candidates were reconstructed from charged tracks identified as kaons or pions, and from neutral pion candidates. The decay modes $D^0 \to K^-\pi^+$, $D^0 \to K^-\pi^+\pi^0$, and $D^0 \to K^-\pi^+\pi^-\pi^+$, and the corresponding charge conjugate $\bar{D}^0$ modes were searched for. The charged tracks used are selected according to the criteria described in §4.5, and the neutral pions were chosen according to the method described in §4.8. Candidates are selected from invariant mass windows which are dependent on their decay mode:

$$\begin{aligned} 1.8399 &< m(K^-\pi^+) < 1.8891\ \mathrm{GeV}/c^2, \\ 1.8334 &< m(K^-\pi^+\pi^0) < 1.8956\ \mathrm{GeV}/c^2, \\ 1.8502 &< m(K^-\pi^+\pi^-\pi^+) < 1.8788\ \mathrm{GeV}/c^2. \end{aligned}$$

The invariant mass peaks for the D^0 meson candidates were fitted with single or double Gaussian functions where appropriate. The candidate selection windows were determined by taking a 3σ region around the nominal D^0 meson mass for $K\pi\pi^0$ and $K\pi\pi\pi$ candidates, and 6σ of the narrower Gaussian for $K\pi$ candidates. The invariant mass spectra for D^0 candidates in experiment 15 are shown in figure 4.9. Similar plots for the invariant mass spectra in signal Monte–Carlo are shown in figure 4.10. The discrepancy between the mass resolution in the MC and experiment 15 is summarised in table 4.3. The most notable difference is in the peak width of the $D^0 \to K\pi\pi^0$ mode. This is mainly due to the difficulty in fitting a double Gaussian function to the peak of figure 4.9(b).

Track combinations that pass the relevant mass cut were then mass constrained vertex fitted and their

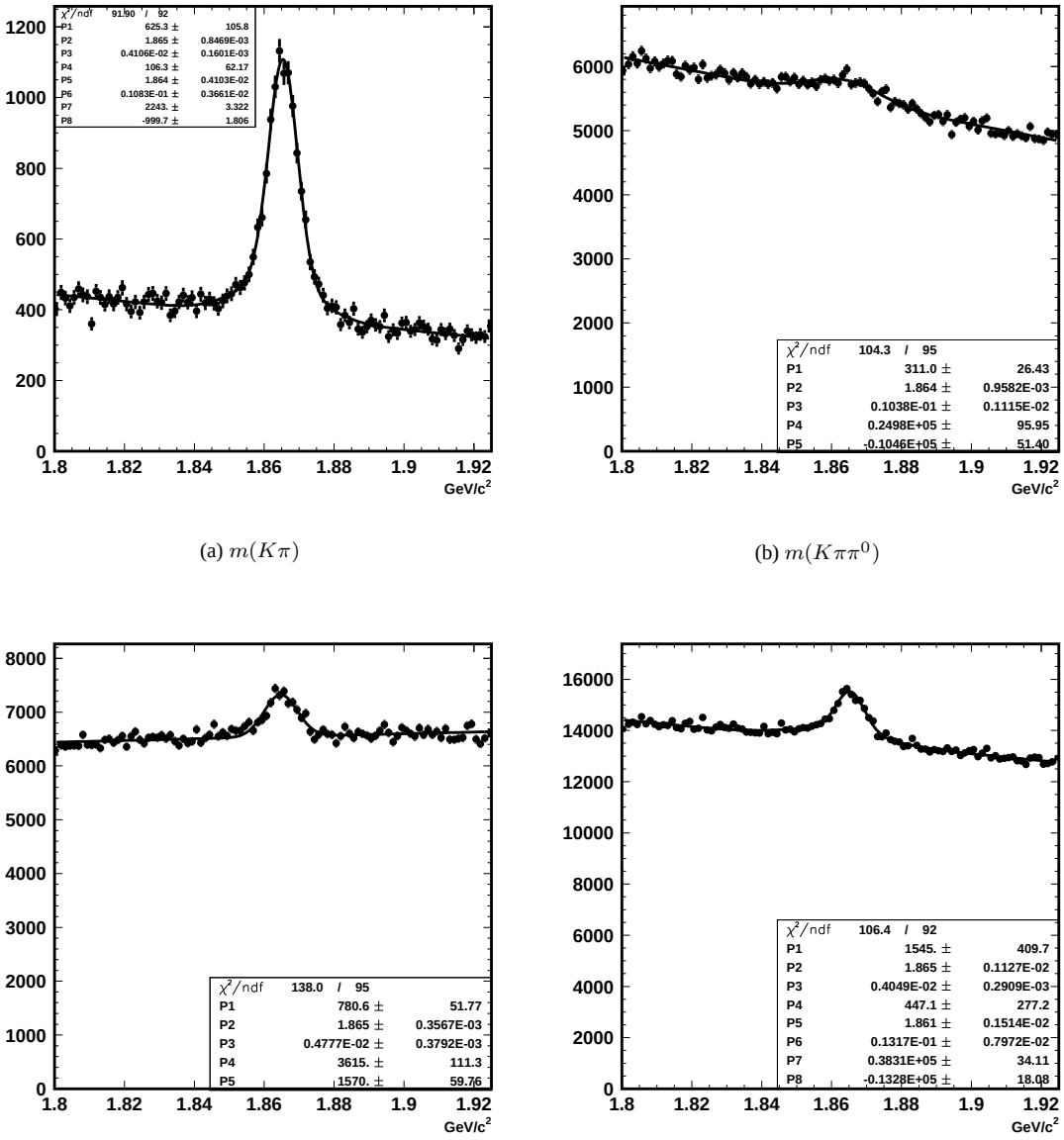

(a) $m(K\pi)$

(b) $m(K\pi\pi^0)$

(c) $m(K\pi\pi\pi)$

(d) All modes

Figure 4.9: The invariant mass spectrum for D^0 candidates. These spectra are for runs 600 to 617 in experiment 15.

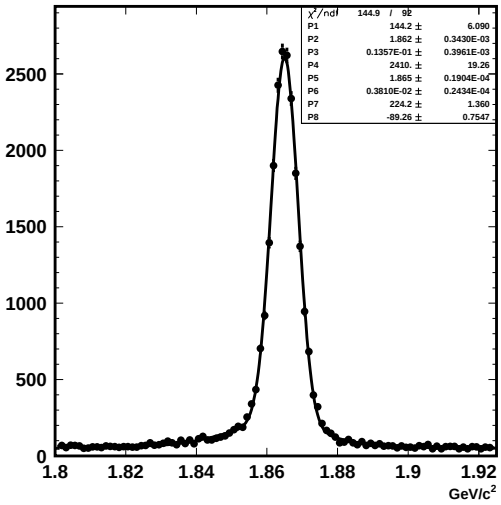

(a) $m(K\pi)$

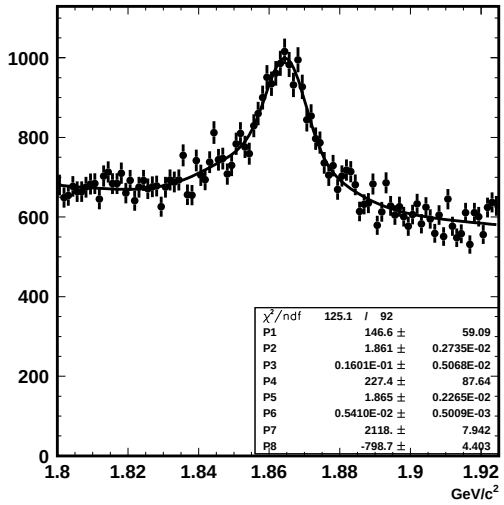

(b) $m(K\pi\pi^0)$

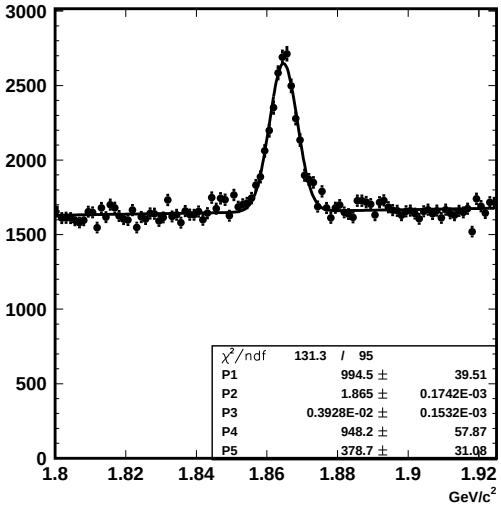

(c) $m(K\pi\pi\pi)$

Figure 4.10: The invariant mass spectrum for D^0 candidates. These spectra are from experiment 15 signal MC.

Decay Mode	experiment 15 data		experiment 15 Monte–Carlo	
	mean (GeV/c^2)	resolution (MeV/c^2)	mean (GeV/c^2)	resolution (MeV/c^2)
$K\pi$	1.865 ± 0.008	4.1 ± 0.2	1.865 ± 0.001	3.81 ± 0.02
$K\pi\pi^0$	1.864 ± 0.010	10.4 ± 1.1	1.865 ± 0.002	5.4 ± 0.5
$K\pi\pi\pi$	1.865 ± 0.004	4.8 ± 0.4	1.865 ± 0.001	3.9 ± 0.2

Table 4.3: The D^0 meson candidate means and resolutions for experiment 15.

momenta were reparameterised.

4.11 D^* reconstruction

D^{*+} and D^{*-} candidates were reconstructed by combining neutral D meson candidates with slow pion (π_s) tracks. This corresponds to a reconstruction of the $D^{*+} \to D^0\pi^+$ decay mode and its charge conjugate. The slow pion candidate's momentum is required to be less than $300\ \mathrm{MeV}/c$. These slow pions are then combined with D^0 candidates from all three modes described in §4.10 to form D^{*+} candidates. Slow pion candidates are not subject to particle identification, nor to the impact parameter cuts of §4.5.

Unlike the other particle candidates, which are chosen from invariant mass windows, D^* candidates are selected from a 6σ region around the narrow peak in the $m(D^0\pi_s) - m(D^0)$ distribution, where $m(D^0)$ is the mass of the D^0 daughter candidate after a mass constrained vertex fit. Figure 4.11 shows these distributions in experiment 15, and figure 4.12 shows them for signal Monte–Carlo.

The background shape in figures 4.11 and 4.12 is modelled with a threshold function, which is given by

$$f(x) = A(x - m(\pi^+))^{\frac{1}{2}} + B(x - m(\pi^+))^{\frac{3}{2}}, \tag{4.16}$$

where A and B are free parameters, $m(\pi^+)$ is the charged pion mass, and x is the value of $m(D^0\pi_s) - m(D^0)$. The peak was fitted with a double Gaussian, except for the $D^{*+} \to D^0(K\pi\pi^0)\pi_s^+$ mode in figure 4.11(b), where the use of a single Gaussian function resulted in a better reduced χ^2 for the fit.

D^* candidates are selected which satisfy the condition $142.77 < m(D^0\pi_s) - m(D^0) < 148.11\ \mathrm{MeV}/c^2$. The resolutions from data and signal MC are compared in table 4.4.

D^* candidates which pass the $m(D^0\pi_s) - m(D^0)$ cut are mass constrained vertex fitted, and their momentum is refitted.

4.12 *B* meson reconstruction

B meson candidates are reconstructed from the D^{*+}, $\bar{D}^0$, and K meson candidates. Due to the conservation of energy the B mesons coming from the $\Upsilon(4S)$ decay must each have half of the beam energy. This

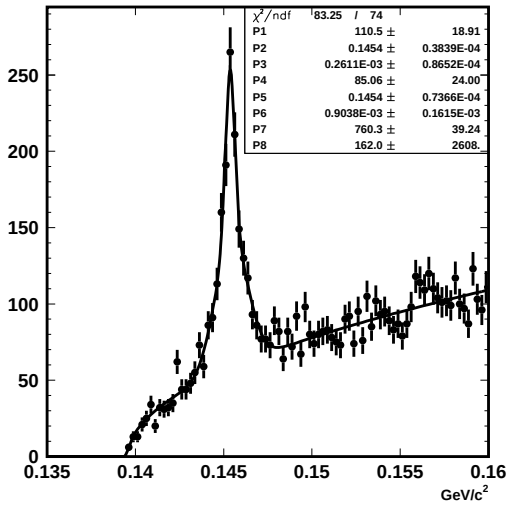

(a) $D^0 \to K\pi$ candidates

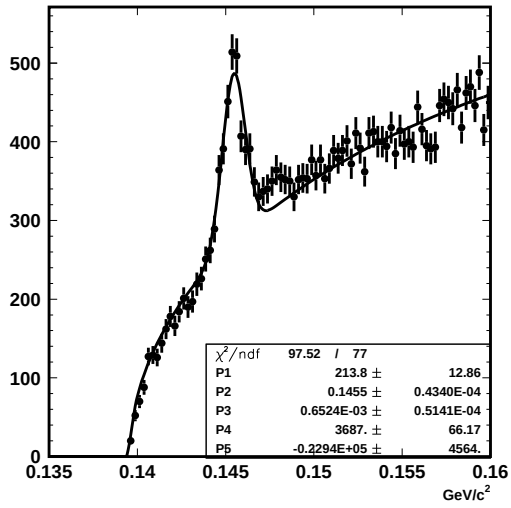

(b) $D^0 \to K\pi\pi^0$ candidates

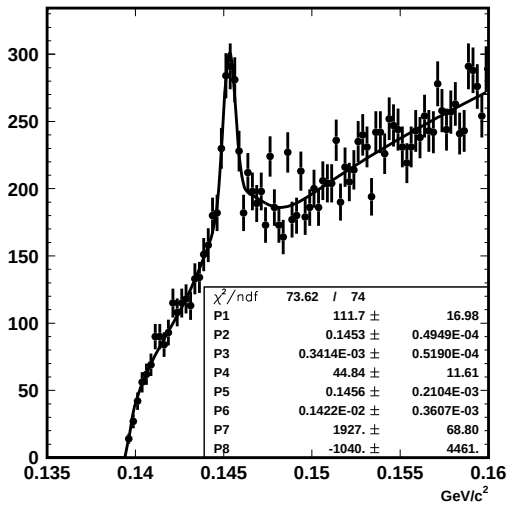

(c) $D^0 \to K\pi\pi\pi$ candidates

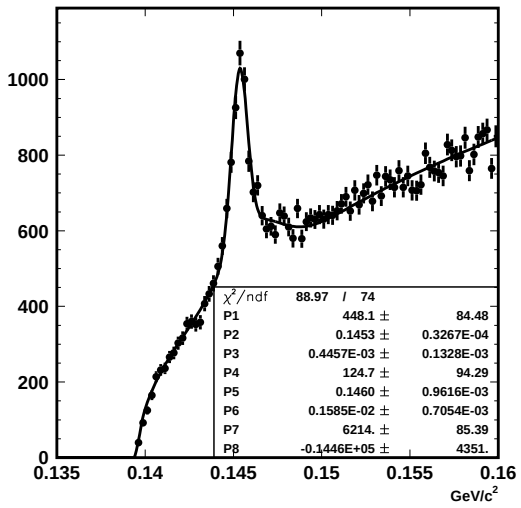

(d) All submodes

Figure 4.11: $m(D^0\pi_s) - m(D^0)$ for D^* candidates. These spectra are for runs 600 to 617 in experiment 15.

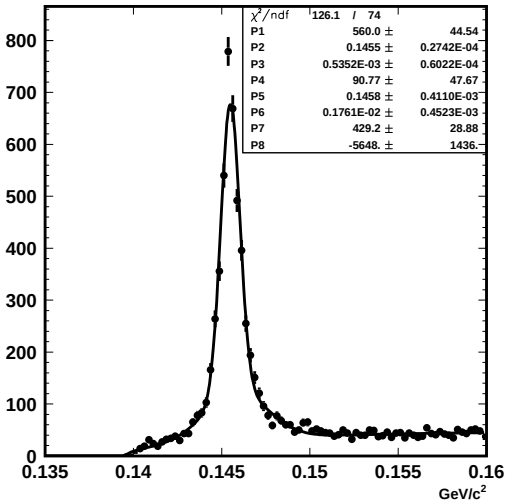

(a) $D^0 \to K\pi$ candidates

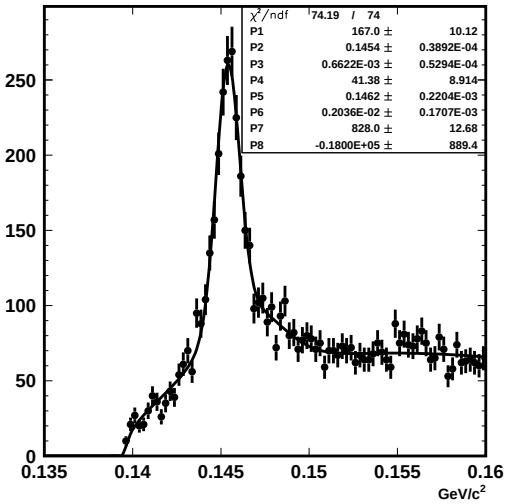

(b) $D^0 \to K\pi\pi^0$ candidates

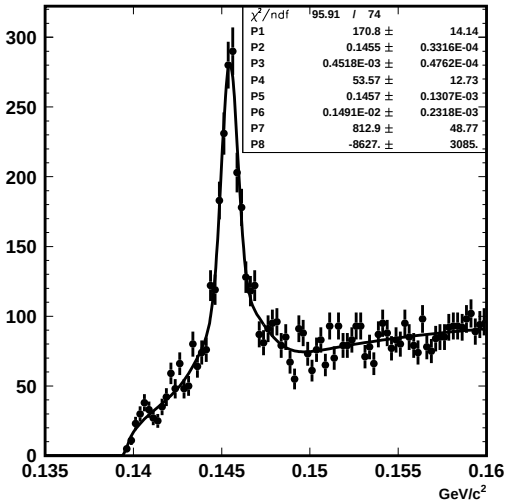

(c) $D^0 \to K\pi\pi\pi$ candidates

Figure 4.12: $m(D^0\pi_s) - m(D^0)$ for D^* candidates in signal MC.

Decay Mode	Sample	σ_1 (keV/c^2)	σ_2 (keV/c^2)
$K\pi$	e15	904 ± 162	261 ± 87
	MC15	1761 ± 452	535 ± 60
$K\pi\pi^0$	e15	n/a	652 ± 51
	MC15	2036 ± 171	662 ± 53
$K\pi\pi\pi$	e15	1422 ± 361	341 ± 52
	MC15	1491 ± 232	452 ± 48
All modes	e15	1585 ± 705	446 ± 133

Table 4.4: The resolution of $m(D^0\pi_s) - m(D^0)$ for D^* candidates.

constraint provides for two variables which are useful in identifying B meson candidates. These are the beam constrained mass,

$$M_{bc} = \sqrt{(E_{cm}/2)^2 - P_B^2}, \tag{4.17}$$

and the missing energy,

$$\Delta E = E_B - E_{cm}/2. \tag{4.18}$$

Here E_B is the reconstructed energy of the B meson candidate, E_{cm} is the beam energy, and P_B is the reconstructed momentum of the B meson candidate in the $\Upsilon(4S)$ rest frame.

Due to the large number of tracks required to reconstruct $B \rightarrow D^* D^{(*)} K$ decays the combinatorial background from the many possible ways to combine tracks is quite high. This leads to instances where there are many possible B meson candidates per event, as shown in figure 4.13.

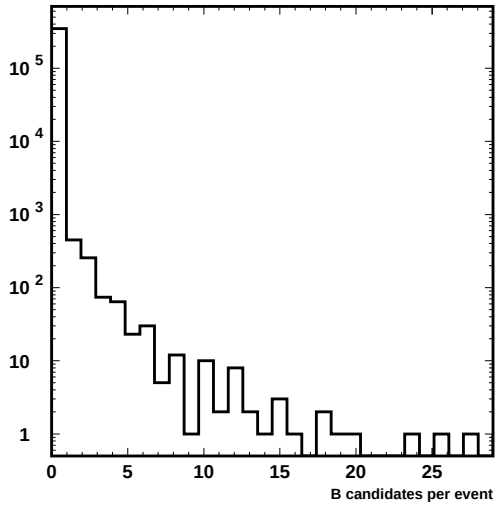

Figure 4.13: The number of B meson candidates per event in experiment 15

In order to pick a single, *best* B meson for each event, a χ^2 value is constructed for each candidate.

This is defined as

$$\chi^2_B = \chi^2_{D^*} + \chi^2_{D^0} + \chi^2_{\bar{D}^0} \quad (+\chi^2_{K_S}) \tag{4.19}$$

where

$$\chi^2_{D^*} = \frac{\left|m(D^0\pi) - m(D^*)\right|^2}{\sigma^2_{D^*}}, \tag{4.20}$$

$$\chi^2_{D^0} = \frac{\left|m(K\pi, K\pi\pi^0, K\pi\pi\pi) - m(D^0)\right|^2}{\sigma^2_{D^0(K\pi,K\pi\pi^0,K\pi\pi\pi)}}, \tag{4.21}$$

and

$$\chi^2_{K_S} = \frac{\left|m(\pi^+\pi^-) - m(K_S)\right|^2}{\sigma^2_{K_S}}. \tag{4.22}$$

The resolutions, $\sigma_{D^0(K\pi,K\pi\pi^0,K\pi\pi\pi)}$, σ_{D^*}, and σ_{K_S}, are measured from experiment 15. On the occasions that two or more B meson candidates are made from the same D^* and D^0 candidates, but different prompt kaons, the B meson candidate with the best χ^2 value from a vertex constrained fit is selected. This method avoids biasing the M_{bc} and ΔE distributions so that they may be used to calculate the signal yield.

Chapter 5

Reconstruction efficiency and background study

One of the aims of reconstructing doubly charmed B meson decays is to measure their branching ratios. These measurements will go some way to resolving the charm counting problem discussed in §2.5. An analysis of the D^*K and $D^{(*)0}K$ mass spectrum can also be used to look for the resonances described in §2.6. A measurement of the time dependent decay asymmetry of equation 2.57 for $B^0 \to D^{*+}D^{*-}K_S$ decays will enable a measurement of *CP* violation, as described in §2.4.

While the latter two objectives can be accomplished through an analysis of B meson candidates that satisfy the selection criteria of chapter 4, the first task, measuring the branching ratio, requires knowledge of the efficiency with which the analysis method reconstructs events. This is determined by studying Monte–Carlo events that are generated to replicate the hypothesised doubly charmed decay chains.

Alterations to the KEKB accelerator operating conditions over time may affect the reconstruction efficiency. Specifically, changes in beam background conditions may affect the low momentum tracking performance of the CDC. At several stages significant improvements were made to the accelerator tuning parameters which reduced the beam background. To account for effects such as these, signal MC was generated which replicated the KEKB operating conditions during experiments 11, 13, 15 and 17. These experiments were chosen to provide a broad cross–section of the background conditions across the data set described in §4.1.

5.1 Signal efficiency

The decays of B mesons to the doubly charmed final states $D^{*+}\bar{D}^0K^-$, $D^{*+}\bar{D}^{*0}K^-$, $D^{*+}D^{*-}K^-$ and $D^{*+}D^{*-}K_S$ can be examined seperately according to the decay mode of the D^0 and $\bar{D}^0$ mesons in the final stage of the decay cascade. By reconstructing the intermediate D^0 mesons through their decay to the

three final states described in §4.10 there are nine submodes via which each B meson may decay.

Each of these submodes will contribute in different proportion to the measured B meson signal yield. This weighting will be relative to both the branching ratio of the relevant D^0 meson decay modes and the reconstruction efficiency of the individual submode. The products of the branching ratios of $D^0 \to K\pi$, $K\pi\pi^0$ and $K\pi\pi\pi$ decays are summarised in table 5.1. While the $K\pi\pi^0$ and $K\pi\pi\pi$ final states have significantly higher branching ratios they tend to have lower reconstruction efficiencies and all the submodes generally contribute equally to the inclusive yield.

D^0 mode	$\bar{D}^0$mode	Branching ratio, $\mathcal{B}_i^{D\bar{D}}$
$D^0 \to K^-\pi^+$	$\bar{D}^0 \to K^+\pi^-$	1.467×10^{-3}
	$\bar{D}^0 \to K^+\pi^-\pi^0$	5.324×10^{-3}
	$\bar{D}^0 \to K^+\pi^-\pi^+\pi^-$	2.869×10^{-3}
$D^0 \to K^-\pi^+\pi^0$	$\bar{D}^0 \to K^+\pi^-$	5.324×10^{-3}
	$\bar{D}^0 \to K^+\pi^-\pi^0$	19.321×10^{-3}
	$\bar{D}^0 \to K^+\pi^-\pi^+\pi^-$	10.411×10^{-3}
$D^0 \to K^-\pi^+\pi^-\pi^+$	$\bar{D}^0 \to K^+\pi^-$	2.869×10^{-3}
	$\bar{D}^0 \to K^+\pi^-\pi^0$	10.411×10^{-3}
	$\bar{D}^0 \to K^+\pi^-\pi^+\pi^-$	5.61×10^{-3}

Table 5.1: The product of D^0 and $\bar{D}^0$ branching ratios, from [7].

The decays $D^0 \to K\pi\pi^0$ and $K\pi\pi\pi$ most often proceed through intermediate resonant states, such as $K\rho$, $K^*\pi$, $K\pi\rho$ or $K^*\rho$. As this may affect the reconstruction efficiency, care was taken to model this as accurately as possible using the event generator, `QQ98`.

Signal MC data was created by using the detector simulator software, `GSIM`, to simulate the detector interaction of particles generated by `QQ98`, and then the tracks were reconstructed with the standard Belle reconstruction routines. The `b20020424_1007` version of the Belle software library was used for this purpose.

For each doubly charmed decay the nine submodes were treated individually with a separate MC sample. The study of experiment 15 conditions was performed with a sample of roughly 20,000 events in each submode. Due to the large period of time required to generate MC data, and the high level of demand on limited computing resources, it was only possible to create 10,000 events of each submode for experiments 11, 13 and 17. Nonetheless, this corresponds to a signal MC sample of 180,000 events for each of the doubly charmed decay modes in experiment 15, and 90,000 events for each in the other three experiments.

In keeping with chapter 4, the experiment 15 MC sample was used as the basis of the efficiency study. Thus the efficiencies calculated in the following section refer exclusively to experiment 15, however the results of the studies of the other experiments can be found in appendix A on page 121.

As described in §4.12, B meson candidates are identified using the beam constrained mass, M_{bc}, and the missing energy, ΔE.

The shape of the beam constrained mass peak is generally independent of the type of B meson decay being reconstructed. It peaks at the B meson mass, $5.2794\ \mathrm{GeV}/c^2$, and the background shape is generally modelled by the ARGUS function [98, 99], which is given by

$$\frac{dN}{dM_{bc}} = A \times M_{bc} \times \sqrt{1 - \frac{M_{bc}^2}{(E_{\mathrm{cm}}/2)^2}} \times \exp\left[-a\left(1 - \frac{M_{bc}^2}{(E_{\mathrm{cm}}/2)^2}\right)\right], \tag{5.1}$$

where A is a normalisation factor and a describes the shape of the ARGUS function. The width of M_{bc} is primarily determined by the beam energy spread and is normally of the order of $3\ \mathrm{MeV}/c^2$ in the Belle experiment. It tends to be independent of the number and nature of final state particles used to reconstruct the decay. This makes it very difficult to identify any background events which may peak in the M_{bc} signal region as they can be indistinguishable from the signal itself.

For this reason a fit to the missing energy is usually used to determine the signal yield. For a correctly reconstructed B meson candidate ΔE should be zero. Due to energy losses, particularly in the case of events with photons and π^0 mesons, and due to imperfections in the detector's reconstruction of track momentum, ΔE can often be shifted up or down by the order of a few MeV. These processes also make the width of ΔE dependent on the mode of decay. Additionally, the ΔE resolution can be improved by kinematic vertexing, especially when momentum refitting is also performed.

Since the shape of ΔE tends to differ greatly for different B meson decays it is normally quite straightforward to separate any background shapes from the signal shape. By projecting events from a 3σ region around the B meson mass in M_{bc} onto the ΔE axis most signal events are preserved. The resulting spectrum in ΔE can be fitted using various Gaussian functions to represent the signal and background shapes, and background from continuum decays or false combinations of tracks can generally be modelled with a first order polynomial.

However, in the case of doubly charmed B meson decays there are just too many possible final states for it to be feasible to use a fit to the ΔE spectrum as the primary determinant of the signal yield. To proceed in a strictly correct manner it would be necessary to model each B meson signal peak with the sum of nine Gaussians, and some of the ΔE spectra would require up to 36 Gaussians to fit all the signal peaks. It generally suffices to use two, or in some cases three Gaussians to model the inclusive signal peaks in ΔE, however this is not ideal. As there is little or no background from other B decays for $B \to D\bar{D}K$,[1] due primarily to the large number of tracks and strict limits on the momentum of the particles in the decay chain, it suffices to measure the yield from a fit to M_{bc}. Hence all the efficiencies are measured from an analysis of the M_{bc} spectrum for each submode.

[1] see §5.2 later in this chapter

5.1.1 $\bar{B}^0 \to D^{*+}\bar{D}^0 K^-$

Signal MC events of $\bar{B}^0 \to D^{*+}\bar{D}^0 K^-$ were reconstructed using the analysis procedure described in chapter 4.

It can be seen in figure 5.1 that the M_{bc} resolution is largely independent of which $D^0 \otimes \bar{D}^0$ submode the B meson candidate decayed via, while figure 5.2 demonstrates the dependence of the shape of the ΔE spectrum on the decay chain of the B meson. The widths of these signal peaks are summarised in table 5.2.

$\bar{B}^0 \to D^{*+}\bar{D}^0 K^-$		Experiment 15		
$D^{*+} \to D^0\pi_s^+$		ϵ_i	$\sigma(M_{bc})$ (MeV/c^2)	$\sigma(\Delta E)$ (MeV)
$D^0 \to K^-\pi^+$	$\bar{D}^0 \to K^+\pi^-$	0.0857 ± 0.0021	2.9 ± 0.1	6.9 ± 0.1
	$\bar{D}^0 \to K^+\pi^-\pi^0$	0.0272 ± 0.0012	3.2 ± 0.1	8.3 ± 0.4
	$\bar{D}^0 \to K^+\pi^-\pi^+\pi^-$	0.0297 ± 0.0012	3.0 ± 0.1	7.1 ± 0.3
$D^0 \to K^-\pi^+\pi^0$	$\bar{D}^0 \to K^+\pi^-$	0.0276 ± 0.0012	3.1 ± 0.1	9.4 ± 0.5
	$\bar{D}^0 \to K^+\pi^-\pi^0$	0.0084 ± 0.0007	2.8 ± 0.2	12.0 ± 1.1
	$\bar{D}^0 \to K^+\pi^-\pi^+\pi^-$	0.0082 ± 0.0007	3.1 ± 0.2	8.3 ± 0.7
$D^0 \to K^-\pi^+\pi^-\pi^+$	$\bar{D}^0 \to K^+\pi^-$	0.0298 ± 0.0012	3.1 ± 0.1	7.2 ± 0.3
	$\bar{D}^0 \to K^+\pi^-\pi^0$	0.0093 ± 0.0007	3.2 ± 0.2	8.4 ± 0.8
	$\bar{D}^0 \to K^+\pi^-\pi^+\pi^-$	0.0090 ± 0.0007	3.1 ± 0.2	7.8 ± 0.5
Average			3.0 ± 0.1	7.3 ± 0.3

Table 5.2: Efficiencies and signal shapes for $\bar{B}^0 \to D^{*+}\bar{D}^0 K^-$ events in experiment 15 signal MC.

The sum of the products of the efficiencies and D^0 branching ratios for the reconstruction of $\bar{B}^0 \to D^{*+}D^0 K^-$ in experiment 15 signal MC is

$$\sum_{i=1}^{9} \mathcal{B}_i^{D\bar{D}} \epsilon_i = (9.84 \times \pm 0.20) \times 10^{-4}. \tag{5.2}$$

Taking into account the $D^{*\pm} \to D^0\pi^\pm$ branching ratio this becomes

$$\epsilon(B^0 \to D^0 D^{*-} K^+)_{\mathrm{e15}} = (6.66 \pm 0.13) \times 10^{-4}. \tag{5.3}$$

The signal shape of the sum of the nine submodes can be calculated by taking an average of all the widths in table 5.2. This average should be weighted by the error of each measurement, and by the contribution of each submode i, such that

$$\bar{\sigma}^2 = \sum_{i=1}^{9} \frac{W_i \sigma_i^2}{(\epsilon(\sigma_i^2))^2} \Big/ \sum_{i=1}^{9} \frac{W_i}{(\epsilon(\sigma_i^2))^2}, \tag{5.4}$$

where σ_i^2 is the variance of the peak, $\epsilon(\sigma_i^2)$ is the error of the measurement of the variance, and $W_i = \mathcal{B}_i^{D\bar{D}}\epsilon_i$ is the efficiency and branching fraction dependent weighting factor for each submode. The average

$D^0 \to K^-\pi^+$ $D^0 \to K^-\pi^+\pi^0$ $D^0 \to K^-\pi^+\pi^-\pi^+$

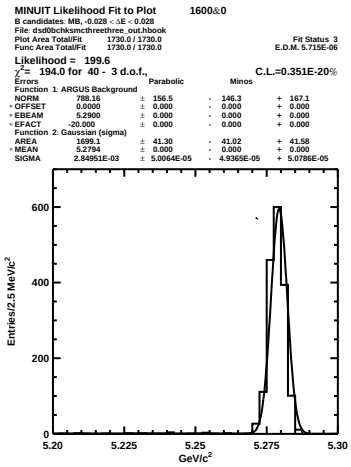

(a) $\bar{D}^0 \to K^+\pi^-$

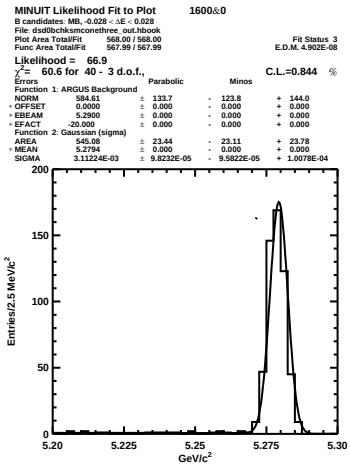

(b) . . .

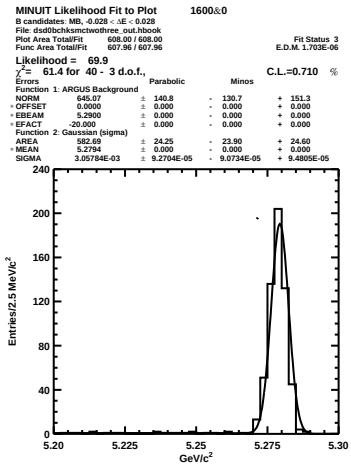

(c) . . .

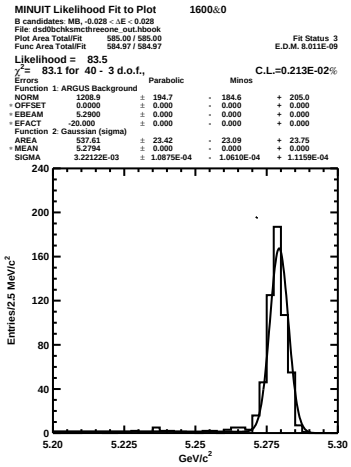

(d) $\bar{D}^0 \to K^+\pi^-\pi^0$

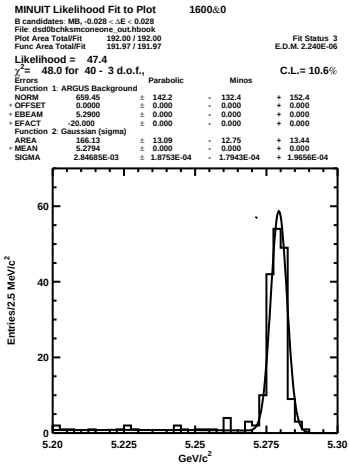

(e) . . .

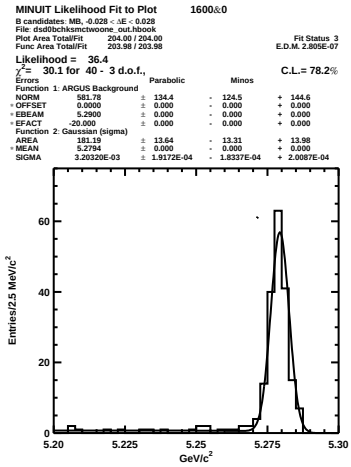

(f) . . .

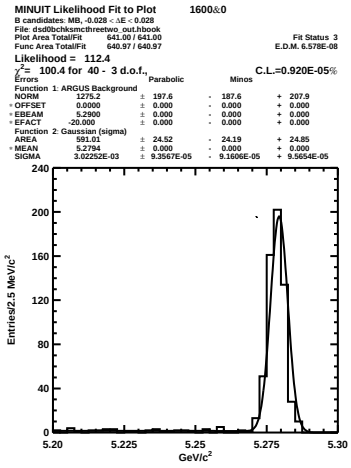

(g) $\bar{D}^0 \to K^+\pi^-\pi^+\pi^-$

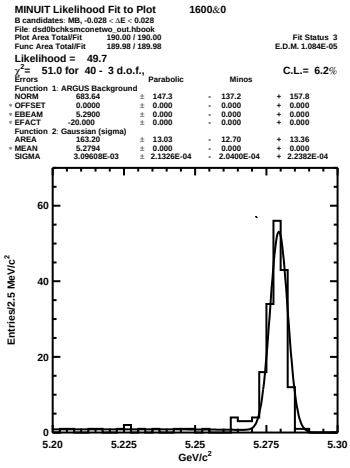

(h) . . .

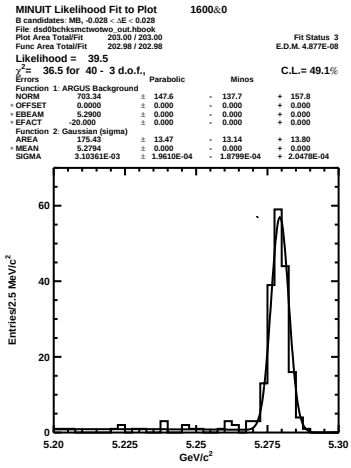

(i) . . .

Figure 5.1: M_{bc} for $\bar{B}^0 \to D^{*+}\bar{D}^0K^-$ events in experiment 15 signal MC. Each column corresponds to a single D^0 decay mode, and each row to a single $\bar{D}^0$ decay mode.

$D^0 \to K^-\pi^+$ $D^0 \to K^-\pi^+\pi^0$ $D^0 \to K^-\pi^+\pi^-\pi^+$

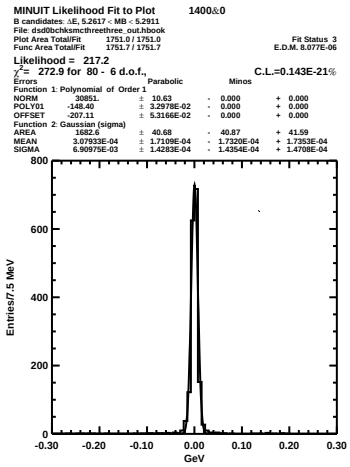

(a) $\bar{D}^0 \to K^+\pi^-$

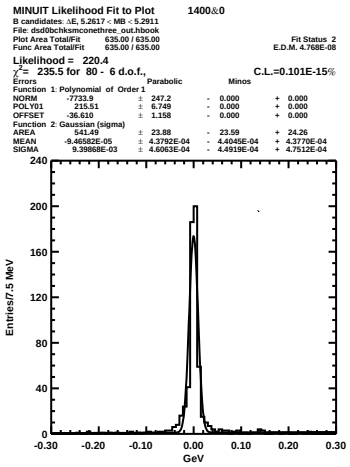

(b) …

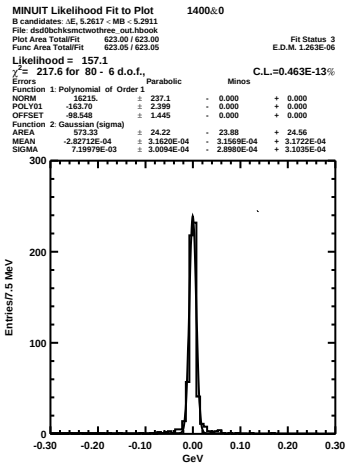

(c) …

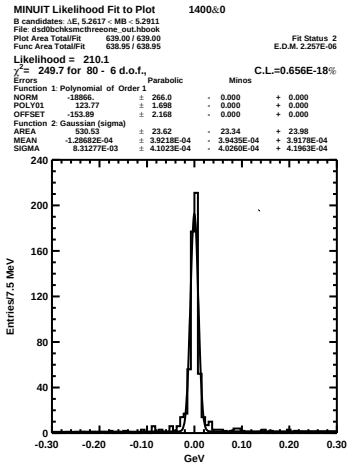

(d) $\bar{D}^0 \to K^+\pi^-\pi^0$

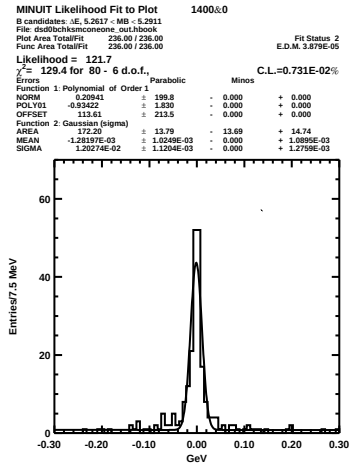

(e) …

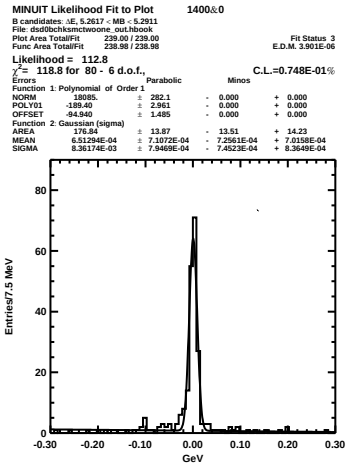

(f) …

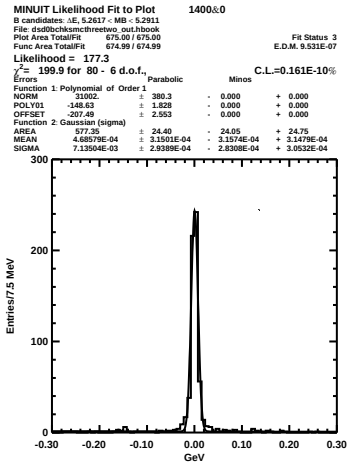

(g) $\bar{D}^0 \to K^+\pi^-\pi^+\pi^-$

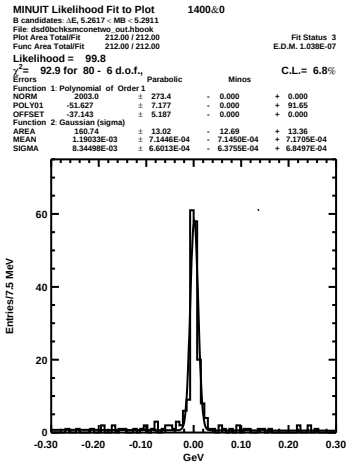

(h) …

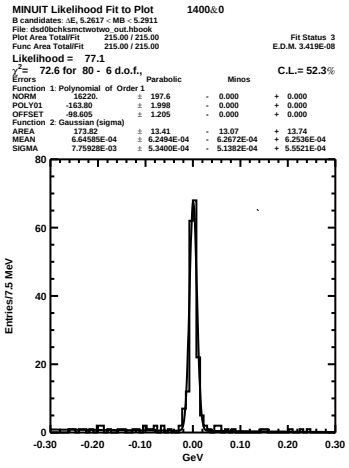

(i) …

Figure 5.2: ΔE for $\bar{B}^0 \to D^{*+}\bar{D}^0K^-$ events in experiment 15 signal MC. Each column corresponds to a single D^0 decay mode, and each row to a single $\bar{D}^0$ decay mode.

width of the M_{bc} peaks in figure 5.1 is $3.0\ \mathrm{MeV}/c^2$. The ΔE distributions are each fitted with a single Gaussian function, however many of the peaks in figure 5.2 have non-Gaussian components due to energy losses, especially for photon candidates, and errors in the measurement of track momenta. This particularly affects the submodes with neutral pions in the final state, and is most prominent in figure 5.2(e), where both the D^0 and $\bar{D}^0$ meson decay to the $K\pi\pi^0$ final state. However, using a double Gaussian function to fit these peaks does not provide a significantly better reduced χ^2, and only serves to complicate the parameterisation.

Alternatively the shape can be determined directly from a fit to the weighted sum of the histograms of figure 5.1 or 5.2. These inclusive M_{bc} and ΔE spectra are shown in figure 5.3. The resolutions of

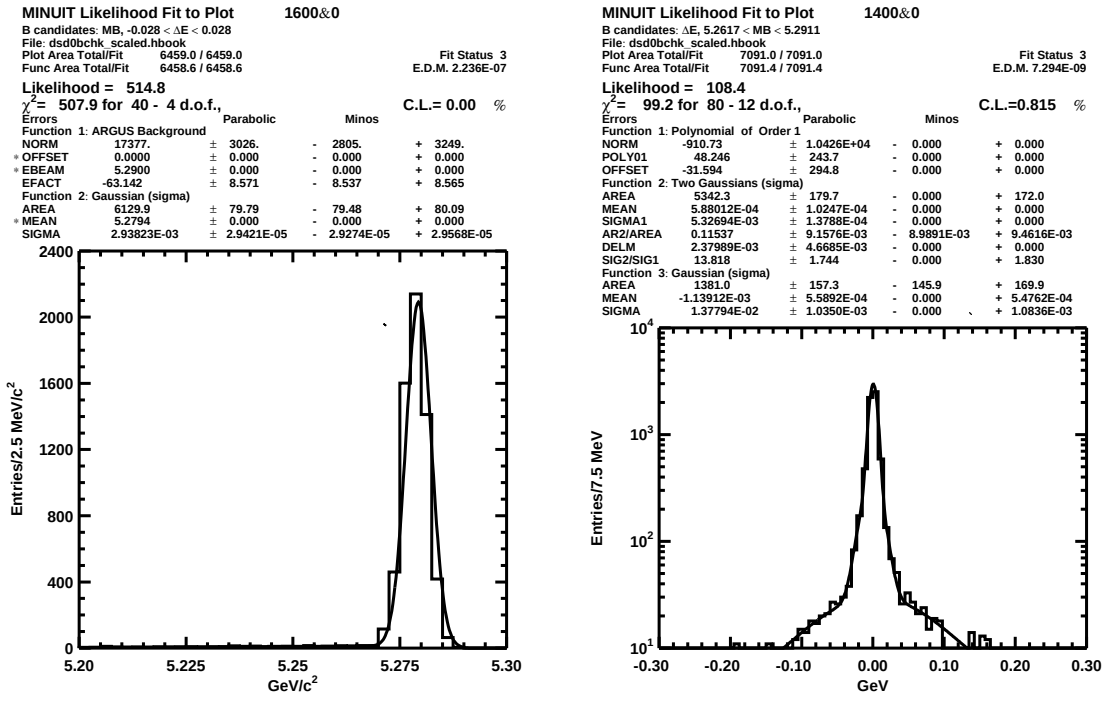

(a) M_{bc} (b) ΔE

Figure 5.3: Signal distributions for $\bar{B}^0 \to D^{*+}\bar{D}^0 K^-$ events in experiment 15 signal MC.

the narrow Gaussian peaks determined from these fits are $\sigma(M_{bc}) = 2.94 \pm 0.03\mathrm{MeV}/c^2$ and $\sigma(\Delta E) = 5.3 \pm 0.1\mathrm{MeV}$, which is in good agreement with the first method. It was necessary to use three Gaussians to obtain a reasonable χ^2/ndf for the fit of the ΔE spectrum in figure 5.3(b). Two of these Gaussians are used to fit the narrow central peak. The means of these peaks are offset by about $-1\ \mathrm{MeV}/c^2$, which is consistent with the energy shift seen in some of the ΔE spectra of figure 5.2. The third Gaussian fits the smaller, broader component of the peak, which is only discernible when the peak is plotted on a logarithmic

scale.

There are therefore three possibilities presented for fitting the inclusive ΔE spectrum. The simplest is to fit the signal peak with a single Gaussian whose width is the weighted average of all the widths in table 5.2. A more accurate, but also complicated, method is to fit the peak using nine Gaussian functions, one for each submode. Aside from the difficult practicalities of performing such a fit, this does not adequately address the non–Gaussian components of the ΔE peak. Using the shape determined from figure 5.3(b) offers the best compromise.

5.1.2 $\bar{B}^0 \to D^{*+}\bar{D}^{*0}K^-$

Decays of neutral B mesons to the $D^{*+}\bar{D}^{*0}K^-$ final state are analysed by performing a reconstruction of the $D^{*+}\bar{D}^0K^-$ decay channel. This omits the slow neutral pion or photon which originates from the $\bar{D}^{*0} \to \bar{D}^0\pi^0$ or $\bar{D}^{*0} \to \bar{D}^0\gamma$ decay.

The missing momentum of the photon or π^0 meson manifests as missing energy in the B meson candidates, and thus a shifted peak in the ΔE spectrum. The signal peak is centred around $-152\ \mathrm{MeV}$, as is evident in figure 5.4(b). This shift is of the same order of magnitude as the $D^{*0} - D^0$ mass difference. The double Gaussian function used to fit the signal shape represents the contributions from the $D^{*0} \to D^0\gamma$ and $D^{*0} \to D^0\pi^0$ decays[2]. Any non–Gaussian components are either lost in the reconstruction method, or are insignificant compared to the scale of these two contributions.

To identify signal B meson candidates the M_{bc} distribution of figure 5.4(a) is plotted for a side–band centred around $\Delta E = -152\,\mathrm{MeV}$. Both signal distributions in figure 5.4 are the sum of histograms created from an analysis of each of the nine individual submodes, as were those in figure 5.3. The resolutions of the individual M_{bc} and ΔE peaks are listed in table 5.3.

Due to the absence of one of the daughter particles, the momentum of the B meson candidate is not correctly calculated, and the M_{bc} signal shape becomes distorted. Therefore a bifurcated Gaussian, with different widths, σ_A and σ_B, to either side of its mean value, is used to fit the beam constrained mass. The weighted average of σ_A for all nine submodes is $6.1\ \mathrm{MeV}/c^2$, and the average of the right side width is $\bar{\sigma}_B = 4\ \mathrm{MeV}/c^2$. The fit of figure 5.4(a) returns $\sigma_A = 5.9 \pm 0.1\ \mathrm{MeV}/c^2$ and $\sigma_B = 3.9 \pm 0.1\ \mathrm{MeV}/c^2$.

Table 5.4 lists the reconstruction efficiency of each submode, and the combination of these for experiment 15 signal MC is $(9.54 \pm 0.21) \times 10^{-4}$. Multiplying this figure by the $D^{*\pm} \to D^0\pi^\pm$ branching ratio the efficiency is calculated as

$$\epsilon(B^0 \to D^{*0}D^{*-}K^+)_{\mathrm{e15}} = (6.46 \pm 0.14) \times 10^{-4}. \tag{5.5}$$

Events from the decay $B^- \to D^{*+}D^{*-}K^-$ peak in roughly the same region as $\bar{B}^0 \to D^{*+}\bar{D}^{*0}K^-$,

[2]The area of the primary Gaussian in figure 5.4(a) is $55 \pm 3\%$ of the total area, comparable with $\mathcal{B}(D^{*0} \to D^0\pi^0) = 61.9 \pm 2.9\%$.

$\bar{B}^0 \to D^{*+}\bar{D}^{*0}K^-$		Experiment 15		
$D^{*+} \to D^0\pi_s^+$		$\sigma_A(M_{bc})$ (MeV/c^2)	$\sigma_B(M_{bc})$ (MeV/c^2)	$\sigma(\Delta E)$ (MeV)
$D^0 \to K^-\pi^+$	$\bar{D}^0 \to K^+\pi^-$	5.7 ± 0.1	3.8 ± 0.1	24.0 ± 0.6
	$\bar{D}^0 \to K^+\pi^-\pi^0$	7.0 ± 0.4	4.2 ± 0.2	30.4 ± 1.4
	$\bar{D}^0 \to K^+\pi^-\pi^+\pi^-$	6.3 ± 0.3	3.9 ± 0.2	26.1 ± 1.1
$D^0 \to K^-\pi^+\pi^0$	$\bar{D}^0 \to K^+\pi^-$	6.7 ± 0.3	4.2 ± 0.2	26.1 ± 1.2
	$\bar{D}^0 \to K^+\pi^-\pi^0$	7.1 ± 0.7	4.4 ± 0.4	36.6 ± 3.3
	$\bar{D}^0 \to K^+\pi^-\pi^+\pi^-$	7.5 ± 0.6	4.2 ± 0.4	31.4 ± 2.9
$D^0 \to K^-\pi^+\pi^-\pi^+$	$\bar{D}^0 \to K^+\pi^-$	6.8 ± 0.4	4.2 ± 0.2	23.1 ± 1.0
	$\bar{D}^0 \to K^+\pi^-\pi^0$	7.3 ± 0.7	4.2 ± 0.3	22.9 ± 2.2
	$\bar{D}^0 \to K^+\pi^-\pi^+\pi^-$	7.4 ± 0.6	4.0 ± 0.4	23.0 ± 2.7
Average		6.1 ± 0.3	4.0 ± 0.2	25.2 ± 1.2

Table 5.3: Signal shapes for $\bar{B}^0 \to D^{*+}\bar{D}^{*0}K^-$ events in experiment 15 signal MC.

$\bar{B}^0 \to D^{*+}\bar{D}^{*0}K^-$		Experiment 15
$D^{*+} \to D^0\pi_s^+$		ϵ_i
$D^0 \to K^-\pi^+$	$\bar{D}^0 \to K^+\pi^-$	0.0772 ± 0.0020
	$\bar{D}^0 \to K^+\pi^-\pi^0$	0.0247 ± 0.0012
	$\bar{D}^0 \to K^+\pi^-\pi^+\pi^-$	0.0282 ± 0.0013
$D^0 \to K^-\pi^+\pi^0$	$\bar{D}^0 \to K^+\pi^-$	0.0252 ± 0.0012
	$\bar{D}^0 \to K^+\pi^-\pi^0$	0.0091 ± 0.0007
	$\bar{D}^0 \to K^+\pi^-\pi^+\pi^-$	0.0095 ± 0.0008
$D^0 \to K^-\pi^+\pi^-\pi^+$	$\bar{D}^0 \to K^+\pi^-$	0.0265 ± 0.0012
	$\bar{D}^0 \to K^+\pi^-\pi^0$	0.0095 ± 0.0007
	$\bar{D}^0 \to K^+\pi^-\pi^+\pi^-$	0.0081 ± 0.0007

Table 5.4: Effi ciencies for $\bar{B}^0 \to D^{*+}\bar{D}^{*0}K^-$ events in experiment 15 signal MC.

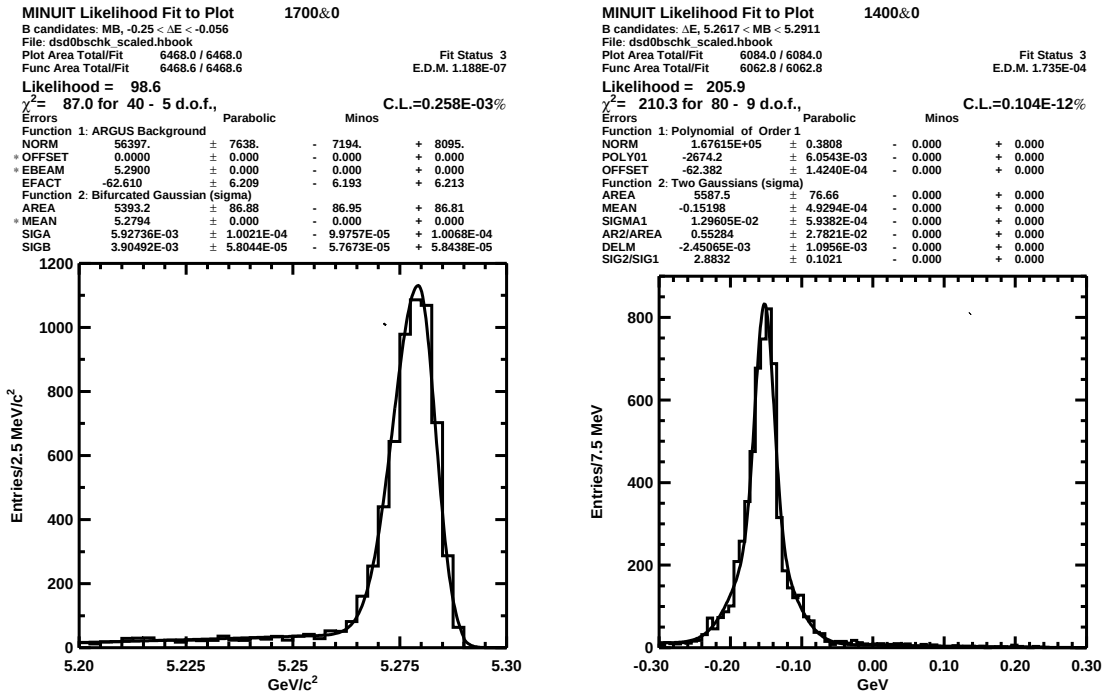

(a) M_{bc} (b) ΔE

Figure 5.4: Signal distributions for $\bar{B}^0 \to D^{*+}\bar{D}^{*0}K^-$ events in experiment 15 signal MC.

since the four–momentum of the missing π^- meson from the $D^{*-} \to \bar{D}^0\pi^-$ decay is comparable to that of the π^0 or photon from the $\bar{D}^{*0}$ decay. To estimate the background contribution from these charged B meson decays a comparable sample of MC events was analysed using the same analysis technique.

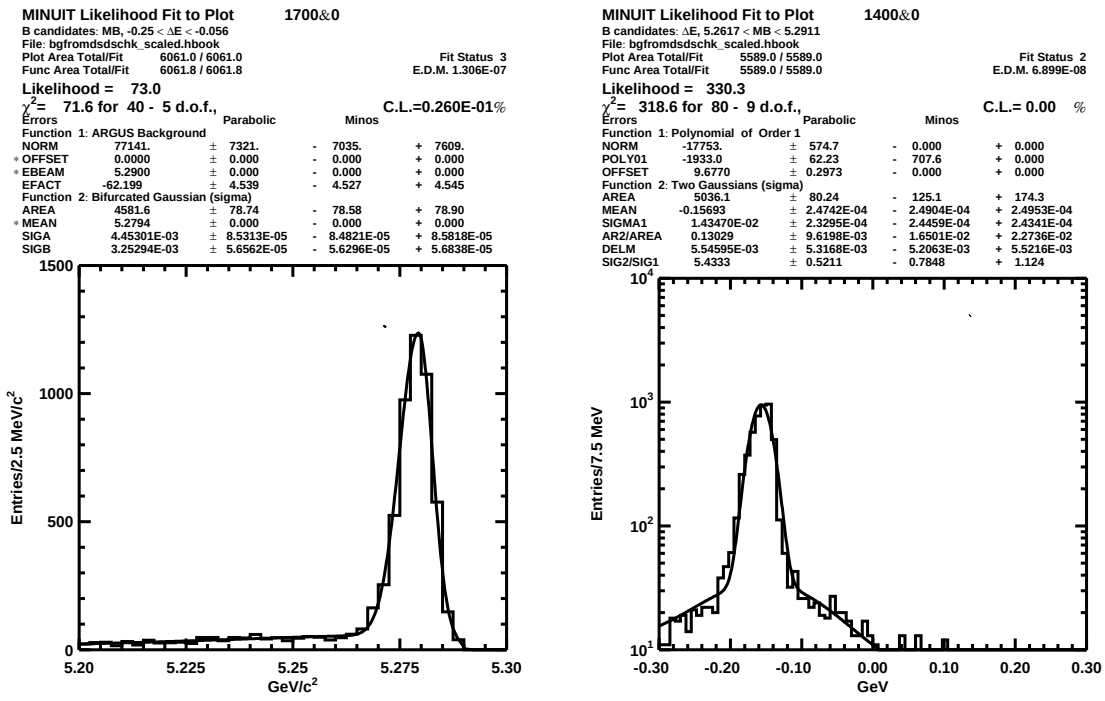

(a) M_{bc} (b) ΔE

Figure 5.5: Signal distributions for $B^- \to D^{*+}D^{*-}K^-$ events falsely reconstructed as $\bar{B}^0 \to D^{*+}\bar{D}^0K^-$ in experiment 15 signal MC.

Figure 5.5(b) demonstrates that the $B^- \to D^{*+}D^{*-}K^-$ events peak in the same signal region as $\bar{B}^0 \to D^{*+}\bar{D}^{*0}K^-$ events. Therefore the yield in this signal region will contain B mesons from both decay modes. The ΔE distribution for these partially reconstructed $B^- \to D^{*+}D^{*-}K^-$ decays consists of a central Gaussian peak and a smaller non–Gaussian contribution similar to that of figure 5.3(b). Unlike the shape of figure 5.4(b), the central peak of figure 5.5(b) can be modelled with a single Gaussian function since only one sort of D^* decay contributes to it. The peak is centred at $\Delta E = -157$ MeV, which is roughly comparable to the difference in mass between the D^{*+} and D^0 meson.

The M_{bc} shape of figure 5.5(a) is asymmetric in the same manner as that of figure 5.4(a). However, this asymmetry is smaller, and the peak is narrower: $\sigma_A = 4.5 \pm 0.1\ \mathrm{MeV}/c^2$ and $\sigma_B = 3.3 \pm 0.1\ \mathrm{MeV}/c^2$.

The fake rate for $\bar{B}^0 \to D^{*+}\bar{D}^{*0}K^-$ from $B^- \to D^{*+}D^{*-}K^-$ events is determined from a fit to each of the nine possible decay submodes, the results of which are shown in table 5.5. The total fake rate

$B^- \to D^{*+}D^{*-}K^-$		Experiment 15
$D^{*+} \to D^0\pi_s^+$	$D^{*-} \to \bar{D}^0\pi_s^-$	$\epsilon_i^{\rm fake}$
$D^0 \to K^-\pi^+$	$\bar{D}^0 \to K^+\pi^-$	0.0642 ± 0.0019
	$\bar{D}^0 \to K^+\pi^-\pi^0$	0.0240 ± 0.0012
	$\bar{D}^0 \to K^+\pi^-\pi^+\pi^-$	0.0232 ± 0.0012
$D^0 \to K^-\pi^+\pi^0$	$\bar{D}^0 \to K^+\pi^-$	0.0237 ± 0.0011
	$\bar{D}^0 \to K^+\pi^-\pi^0$	0.0078 ± 0.0007
	$\bar{D}^0 \to K^+\pi^-\pi^+\pi^-$	0.0072 ± 0.0007
$D^0 \to K^-\pi^+\pi^-\pi^+$	$\bar{D}^0 \to K^+\pi^-$	0.0252 ± 0.0012
	$\bar{D}^0 \to K^+\pi^-\pi^0$	0.0082 ± 0.0007
	$\bar{D}^0 \to K^+\pi^-\pi^+\pi^-$	0.0072 ± 0.0007

Table 5.5: Fake rate for $\bar{B}^0 \to D^{*+}\bar{D}^{*0}K^-$ from $B^- \to D^{*+}D^{*-}K^-$ events in experiment 15 signal MC.

is $(8.39 \pm 0.21) \times 10^{-4}$. Multiplying this by both D^* branching ratios determines

$$\epsilon(B^+ \to D^{*+}D^{*-}K^+)_{\rm e15\_fake} = (3.85 \pm 0.09) \times 10^{-4}. \tag{5.6}$$

The shape for each background submode is summarised in table 5.6.

$B^- \to D^{*+}D^{*-}K^-$		Experiment 15		
$D^{*+} \to D^0\pi_s^+$	$D^{*-} \to \bar{D}^0\pi_s^-$	$\sigma_A(M_{bc})$ (MeV/c^2)	$\sigma_B(M_{bc})$ (MeV/c^2)	$\sigma(\Delta E)$ (MeV)
$D^0 \to K^-\pi^+$	$\bar{D}^0 \to K^+\pi^-$	4.4 ± 0.1	3.2 ± 0.1	14.1 ± 0.3
	$\bar{D}^0 \to K^+\pi^-\pi^0$	5.2 ± 0.3	3.6 ± 0.2	16.8 ± 0.8
	$\bar{D}^0 \to K^+\pi^-\pi^+\pi^-$	4.9 ± 2.9	3.4 ± 0.2	15.5 ± 0.7
$D^0 \to K^-\pi^+\pi^0$	$\bar{D}^0 \to K^+\pi^-$	5.2 ± 0.3	3.5 ± 0.2	16.6 ± 0.8
	$\bar{D}^0 \to K^+\pi^-\pi^0$	7.2 ± 0.8	3.6 ± 0.4	18.1 ± 1.8
	$\bar{D}^0 \to K^+\pi^-\pi^+\pi^-$	6.7 ± 0.1	4.3 ± 0.4	15.7 ± 1.6
$D^0 \to K^-\pi^+\pi^-\pi^+$	$\bar{D}^0 \to K^+\pi^-$	4.7 ± 0.2	3.6 ± 0.2	15.3 ± 0.7
	$\bar{D}^0 \to K^+\pi^-\pi^0$	6.9 ± 0.7	3.7 ± 0.3	14.9 ± 1.4
	$\bar{D}^0 \to K^+\pi^-\pi^+\pi^-$	5.0 ± 0.5	3.7 ± 0.3	16.3 ± 1.4
Average		4.8 ± 0.3	3.4 ± 0.2	15.2 ± 0.7

Table 5.6: Resolutions for partially reconstructed $B^- \to D^{*+}D^{*-}K^-$ decays in experiment 15 signal MC.

5.1.3 $B^- \to D^{*+}D^{*-}K^-$

The fake rate of equation 5.6 does not provide an estimate of the $B^+ \to D^{*+}D^{*-}K^+$ background in and of itself. The background yield must be calculated as

$$B = \mathcal{B}(B^+ \to D^{*+}D^{*-}K^+) \times \epsilon(B^+ \to D^{*+}D^{*-}K^+)_{\rm e15\_fake}. \tag{5.7}$$

To measure the branching ratio, $\mathcal{B}(B^+ \to D^{*+}D^{*-}K^+)$, a full reconstruction of charged B candidates is performed. The reconstruction efficiency is measured using the same analysis technique as in §5.1.1. In this instance a B^- is reconstructed using D^{*+}, D^{*-} and K^- candidates.

$B^- \to D^{*+}D^{*-}K^-$		Experiments 15		
$D^{*+} \to D^0\pi_s^+$	$D^{*-} \to D^0\pi_s^-$	ϵ_i	$\sigma(M_{bc})$ (MeV/c^2)	$\sigma(\Delta E)$ (MeV)
$D^0 \to K^-\pi^+$	$\bar{D}^0 \to K^+\pi^-$	0.0200 ± 0.0010	3.0 ± 0.1	6.4 ± 0.3
	$\bar{D}^0 \to K^+\pi^-\pi^0$	0.0062 ± 0.0006	2.8 ± 0.2	8.6 ± 0.9
	$\bar{D}^0 \to K^+\pi^-\pi^+\pi^-$	0.0060 ± 0.0006	3.5 ± 0.2	7.8 ± 0.5
$D^0 \to K^-\pi^+\pi^0$	$\bar{D}^0 \to K^+\pi^-$	0.0050 ± 0.0005	3.5 ± 0.3	10.9 ± 1.0
	$\bar{D}^0 \to K^+\pi^-\pi^0$	0.0020 ± 0.0003	3.9 ± 0.5	9.0 ± 1.1
	$\bar{D}^0 \to K^+\pi^-\pi^+\pi^-$	0.0018 ± 0.0003	3.6 ± 0.5	4.4 ± 0.7
$D^0 \to K^-\pi^+\pi^-\pi^+$	$\bar{D}^0 \to K^+\pi^-$	0.0066 ± 0.0006	3.0 ± 0.2	7.9 ± 0.6
	$\bar{D}^0 \to K^+\pi^-\pi^0$	0.0019 ± 0.0003	3.4 ± 0.5	8.1 ± 1.2
	$\bar{D}^0 \to K^+\pi^-\pi^+\pi^-$	0.0025 ± 0.0004	3.5 ± 0.4	8.9 ± 1.0
Average			3.0 ± 0.2	6.7 ± 0.6

Table 5.7: Efficiencies and signal shapes for $B^- \to D^{*+}D^{*-}K^-$ events in experiment 15 signal MC.

The ΔE spectrum of figure 5.6(b) peaks around zero. Due to the extra vertexing constraint from the $D^{*-} \to \bar{D}^0\pi^-$ decay the ΔE signal shape is narrower than that of figure 5.3(b), and it is well modelled by a double Gaussian function.

The efficiency for reconstructing $B^+ \to D^{*+}D^{*-}K^+$ decays is determined by summing the products of the efficiencies, ϵ_i, in table 5.7 with the branching ratio of each $D^0 \otimes \bar{D}^0$ submode, $\mathcal{B}_i^{D\bar{D}}$, shown in table 5.1. The efficiency is $(2.16 \pm 0.09) \times 10^{-4}$. Multiplying this by the product of the D^* branching ratios determines

$$\epsilon(B^+ \to D^{*+}D^{*-}K^+)_{\mathrm{e15}} = (9.92 \pm 0.43) \times 10^{-5}. \tag{5.8}$$

5.1.4 $\bar{B}^0 \to D^{*+}D^{*-}K_S$

The inclusive M_{bc} and ΔE spectra for $B^0 \to D^{*+}D^{*-}K_S$ signal MC decays are shown in figure 5.7. Like the spectrum of figure 5.6(b) the ΔE shape for these decays is reasonably well modelled by a double Gaussian function with a narrow width of $5.4\ \mathrm{MeV}/c^2$. The vertexing constraints from the two D^* decays and from the $K_S \to \pi^+\pi^-$ decay greatly improve the resolution relative to other decay modes. The shapes and reconstruction efficiencies for each submode are summarised in table 5.8.

The sum of the products of the efficiencies and D^0 branching ratios for $\bar{B}^0 \to D^{*+}D^{*-}K_S$ is $(9.81 \pm 0.64) \times 10^{-5}$. As mentioned in §3.4 the K_S meson is not constrained to decay to the $\pi^+\pi^-$ final state by the event generator when these signal MC events are produced, so the branching ratio of $K_S \to \pi^+\pi^-$ does not need to be accounted for. However, we are really interested in the $B^0 \to D^{*+}D^{*-}K^0$ branching

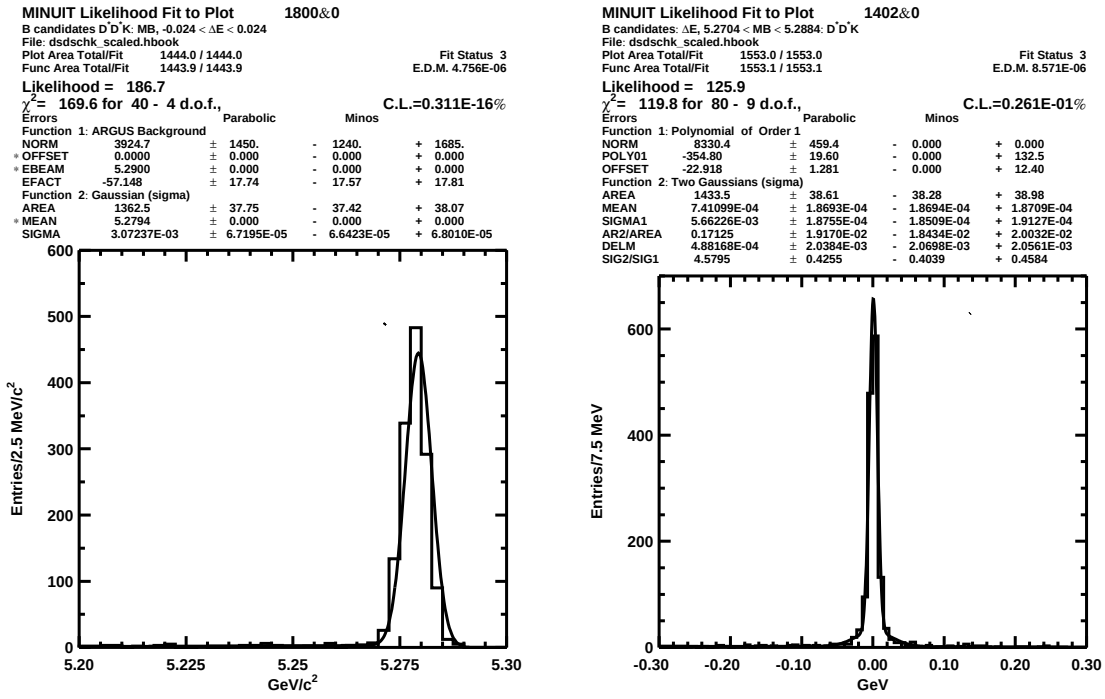

(a) M_{bc} (b) ΔE

Figure 5.6: Signal distributions for $B^- \to D^{*+}D^{*-}K^-$ events in experiment 15 signal MC.

$\bar{B}^0 \to D^{*+}D^{*-}K_S$		Experiment 15		
$D^{*+} \to D^0\pi_s^+$	$D^{*-} \to \bar{D}^0\pi_s^-$	ϵ_i	$\sigma(M_{bc})$ (MeV/c^2)	$\sigma(\Delta E)$ (MeV)
$D^0 \to K^-\pi^+$	$\bar{D}^0 \to K^+\pi^-$	0.0089 ± 0.0007	3.0 ± 0.2	6.4 ± 0.5
	$\bar{D}^0 \to K^+\pi^-\pi^0$	0.0023 ± 0.0004	3.0 ± 0.4	10.1 ± 1.7
	$\bar{D}^0 \to K^+\pi^-\pi^+\pi^-$	0.0037 ± 0.0004	3.6 ± 0.3	8.1 ± 0.7
$D^0 \to K^-\pi^+\pi^0$	$\bar{D}^0 \to K^+\pi^-$	0.0025 ± 0.0004	3.3 ± 0.5	28.2 ± 2.6
	$\bar{D}^0 \to K^+\pi^-\pi^0$	0.0010 ± 0.0002	3.0 ± 0.5	4.3 ± 0.8
	$\bar{D}^0 \to K^+\pi^-\pi^+\pi^-$	0.0006 ± 0.0002	4.1 ± 0.8	12.3 ± 2.9
$D^0 \to K^-\pi^+\pi^-\pi^+$	$\bar{D}^0 \to K^+\pi^-$	0.0031 ± 0.0004	2.7 ± 0.3	8.1 ± 0.7
	$\bar{D}^0 \to K^+\pi^-\pi^0$	0.0010 ± 0.0002	2.7 ± 0.5	7.2 ± 0.1
	$\bar{D}^0 \to K^+\pi^-\pi^+\pi^-$	0.0008 ± 0.0002	4.0 ± 1.0	11.0 ± 1.7
Average			3.0 ± 0.3	5.7 ± 0.8

Table 5.8: Effi ciencies and signal shapes for $\bar{B}^0 \to D^{*+}D^{*-}K_S$ events in experiment 15 signal MC.

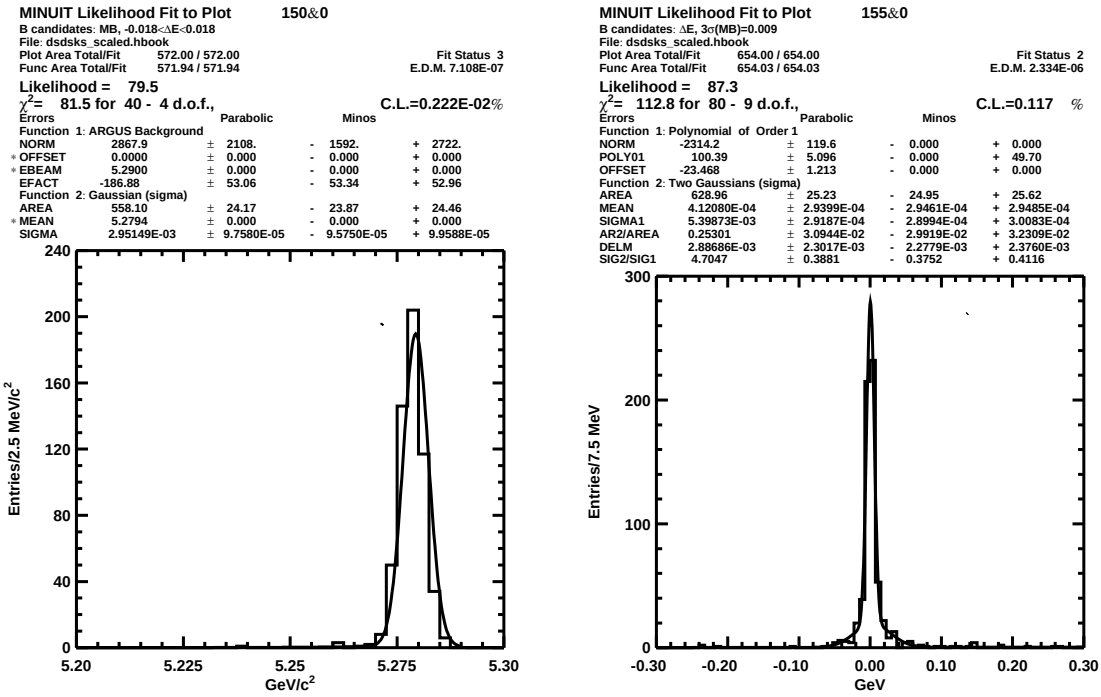

(a) M_{bc} (b) ΔE

Figure 5.7: Signal distributions for $\bar{B}^0 \to D^{*+} D^{*-} K_S$ events in experiment 15 signal MC.

ratio, and since a K^0 manifests as a K_S in half of its decays an extra factor of 0.5 must be included in the efficiency calculation. Therefore, by multiplying the weighted average of the efficiencies in table 5.8 by the D^* branching ratios and by 0.5, the $B^0 \to D^{*+}D^{*-}K^0$ reconstruction efficiency is calculated as

$$\epsilon(B^0 \to D^{*+}D^{*-}K^0)_{\mathrm{e15}} = (2.25 \pm 0.08) \times 10^{-5}. \tag{5.9}$$

5.1.5 Summary

The efficiency for reconstructing each doubly charmed B meson decay was calculated by taking the weighted average of the reconstruction efficiencies measured in signal MC. The signal MC was generated to replicate the run conditions of experiments 11, 13, 15 and 17. The weighting used in this analysis may be expressed as

$$\bar{\epsilon} = \frac{N(B\bar{B})_{\mathrm{e7+9+11}}}{N(B\bar{B})} \cdot \epsilon_{\mathrm{e11}} + \frac{N(B\bar{B})_{\mathrm{e13}}}{N(B\bar{B})} \cdot \epsilon_{\mathrm{e13}} + \frac{N(B\bar{B})_{\mathrm{e15}}}{N(B\bar{B})} \cdot \epsilon_{\mathrm{e15}} + \frac{N(B\bar{B})_{\mathrm{e17+19}}}{N(B\bar{B})} \cdot \epsilon_{\mathrm{e17}}, \tag{5.10}$$

where $N(B\bar{B})_{ex}$ is the number of events in experiment x. The number of $B\bar{B}$ events in each experiment is summarised in table 4.1, and the efficiencies for each experiment are shown in table 5.9. The † denotes that the efficiency refers to the partial reconstruction method with a missing pion or photon.

Mode	Experiment 11	Experiment 13	Experiment 15	Experiment 17
$B^0 \to D^0 D^{*-} K^+$	6.83 ± 0.20	6.90 ± 0.19	6.66 ± 0.13	6.26 ± 0.19
$B^0 \to D^{*0} D^{*-} K^{+\dagger}$	7.09 ± 0.22	7.28 ± 0.21	6.46 ± 0.14	6.45 ± 0.20
$B^+ \to D^{*+} D^{*-} K^{+\dagger}$	4.16 ± 0.13	3.97 ± 0.14	3.85 ± 0.09	3.71 ± 0.12
$B^+ \to D^{*+} D^{*-} K^+$	1.11 ± 0.07	1.01 ± 0.06	0.92 ± 0.04	0.95 ± 0.05
$B^0 \to D^{*+} D^{*-} K^0$	0.210 ± 0.018	0.212 ± 0.018	0.225 ± 0.008	2.25 ± 0.020

Table 5.9: Experiment dependent reconstruction effi ciencies ($\times 10^{-4}$).

Thus, the weighted efficiencies for each of the decay modes are:

$$\begin{aligned}
\bar{\epsilon}(B^0 \to D^0 D^{*-} K^+) &= 6.54 \times 10^{-4}, \\
\bar{\epsilon}(B^0 \to D^{*0} D^{*-} K^+)^\dagger &= 6.69 \times 10^{-4}, \\
\bar{\epsilon}(B^+ \to D^{*+} D^{*-} K^+)^\dagger &= 3.90 \times 10^{-4}, \\
\bar{\epsilon}(B^+ \to D^{*+} D^{*-} K^+) &= 1.02 \times 10^{-4}, \\
\bar{\epsilon}(B^0 \to D^{*+} D^{*-} K^0) &= 2.19 \times 10^{-5},
\end{aligned} \tag{5.11}$$

when all nine submodes are reconstructed. There is a considerably higher background level underneath the signal peaks in the $B^0 \to D^0 D^{*-} K^+$ reconstruction compared to $B^+ \to D^{*+} D^{*-} K^+$, since the double

D^* reconstruction requirement is very effective at rejecting fake signal candidates. This background is predominantly due to incorrect combinations of tracks, and comes mainly from the final states with higher track multiplicity, namely those with a $D^0 \to K\pi\pi^0$ or $D^0 \to K\pi\pi\pi$ transition. By only examining the five submodes where at least one of the D^0 or $\bar{D}^0$ mesons decays to the $K\pi$ final state, which has much lower background levels (see figures 4.9(a) and 4.10(a)), the contribution from this background is reduced while the better portion of signal candidates are retained. The reconstruction efficiencies when only these five submodes are used are:

$$\begin{aligned} \bar{\epsilon}(B^0 \to D^0 D^{*-} K^+)_{K\pi} &= 3.80 \times 10^{-4}, \\ \bar{\epsilon}(B^0 \to D^{*0} D^{*-} K^+)^{\dagger}_{K\pi} &= 3.79 \times 10^{-4}, \\ \bar{\epsilon}(B^+ \to D^{*+} D^{*-} K^+)^{\dagger}_{K\pi} &= 2.27 \times 10^{-4}. \end{aligned} \tag{5.12}$$

5.2 Background study

As mentioned in §5.1, many analyses of B meson decays are susceptible to background from other decay modes which peaks in the same signal region as the mode being investigated. However, due to the large number of tracks required to reconstruct doubly charmed B meson decays, quite stringent requirements are imposed upon the momentum of the final state particles. By requiring that the B meson candidates decay via intermediate D^* and D^0 mesons these constraints are further tightened. The combination of these factors tends to eliminate any significant backgrounds from other decay channels that might peak in the signal region.

However, to rule out any such background a study of a large sample of MC events was performed. These events were generated to simulate the behaviour of the accelerator during experiment 15, replicating the run by run conditions in the manner described in §3.4.

Generic Monte–Carlo data was generated in four samples: neutral B meson decays[3]; charged B meson decays; $e^+e^- \to u\bar{u}, d\bar{d}, s\bar{s}$; and $e^+e^- \to c\bar{c}$ decays. The four samples were generated in the same proportion as in which they are expected to occur in $e^+\,e^-$ interactions at the KEKB Interaction Point. The total number of events in the combined MC data set matches the number of events in experiment 15, given in table 4.1.

`QQ98`, the event generator which mediates the decays of the particles, has a default model of $B^0 \to D^0 D^{*-} K^+$, $B^0 \to D^{*0} D^{*-} K^+$, and $B^0 \to D^{*+} D^{*-} K^0$ decays with branching ratios of 0.5%, 1.5%, and 1.5% respectively. The colour suppressed $B^+ \to D^{*+} D^{*-} K^+$ decays were not simulated.

[3]This sample is also known as the mixed MC sample, since $B^0 - \bar{B}^0$ mixing is permitted

5.2.1 $B^0 \to D^0 D^{*-} K^+$

A full reconstruction of $B^0 \to D^0 D^{*-} K^+$ was performed on the generic MC sample. Figure 5.8 shows the resulting scatter plot of M_{bc} verses ΔE with boxes outlining the two signal regions for $B^0 \to D^0 D^{*-} K^+$ and $B^0 \to D^{*0} D^{*-} K^+$.

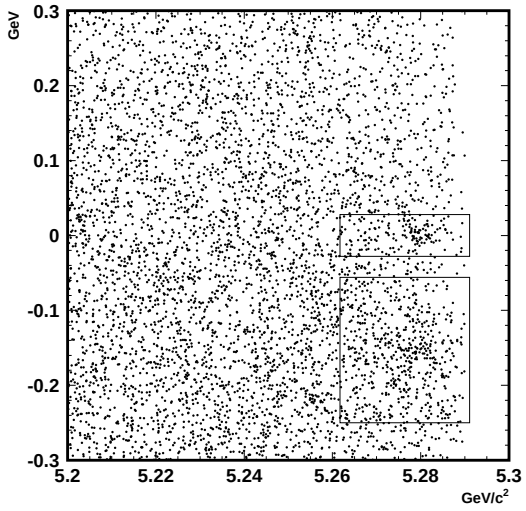

Figure 5.8: M_{bc} vs ΔE for $B^0 \to D^0 D^{*-} K^+$ in generic MC.

The projection of the B candidates onto the M_{bc} axis, after a 3σ cut is made on ΔE, is shown in figure 5.9. Figure 5.9(b) demonstrates the contribution of the four types of events to the M_{bc} distribution for $B^0 \to D^0 D^{*-} K^+$ decay candidates. It is quite clear that the charged B meson and continuum MC samples do not contribute to the signal peak. A fit to the histogram, using the Gaussian shape determined in §5.1.1, results in a signal yield of 50.2 ± 9.6 events. The shape of the ARGUS function was determined from a two dimensional fit to the entire area of figure 5.9, in which both signal peaks were modelled by two dimensional Gaussian functions. It is possible to calculate the branching ratio of $B^0 \to D^0 D^{*-} K^+$ decays in this MC sample using the reconstruction efficiency of equation 5.3. This measured branching ratio is

$$\mathcal{B}(B^0 \to D^0 D^{*-} K^+)_{\texttt{QQ98}} = (5.56 \pm 1.07) \times 10^{-3}, \tag{5.13}$$

where the error is statistical. The result of equation 5.13 is in good agreement with the branching ratio input into `QQ98`.

The validity of the yield measurement can be cross checked by fitting the ΔE signal peak. The missing energy spectrum is shown in figure 5.10. The central peak, fitted with the three Gaussians determined in §5.1.1, has an area of 48.6 ± 6.8 events. The contribution from continuum events and charged B decays to the distribution of figure 5.10(b) is flat underneath both the central $B^0 \to D^0 D^{*-} K^+$ and shifted

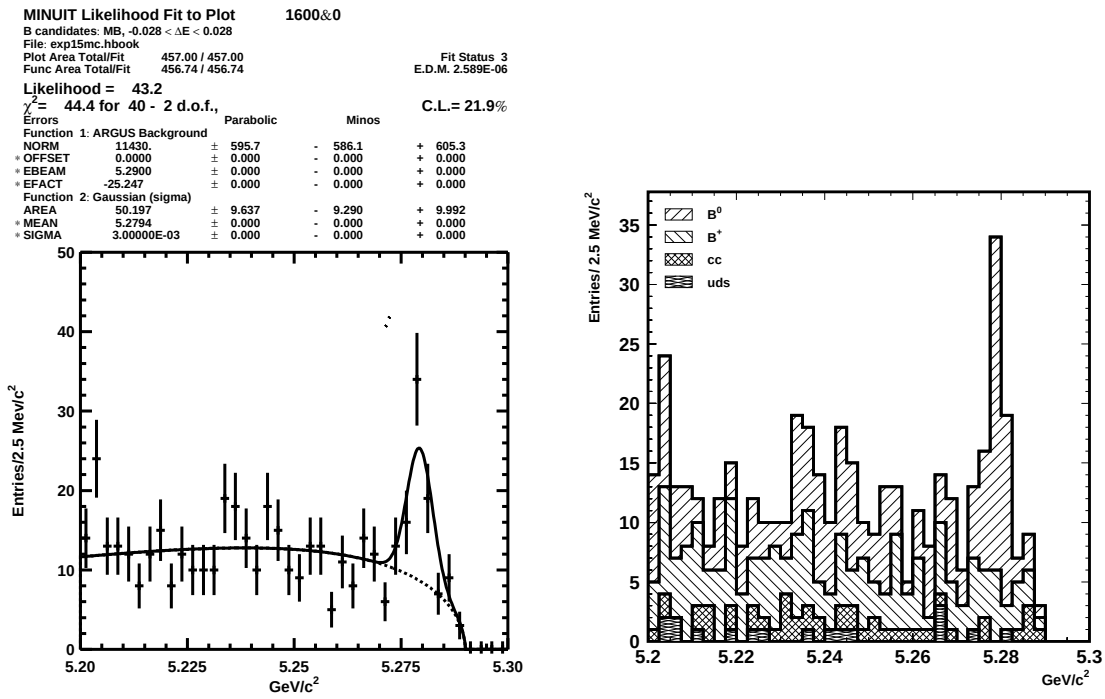

(a) M_{bc}

(b) M_{bc}, breakdown by type.

Figure 5.9: M_{bc} for $B^0 \to D^0 D^{*-} K^+$ decays in generic MC.

$B^0 \to D^{*0} D^{*-} K^+$ peaks.

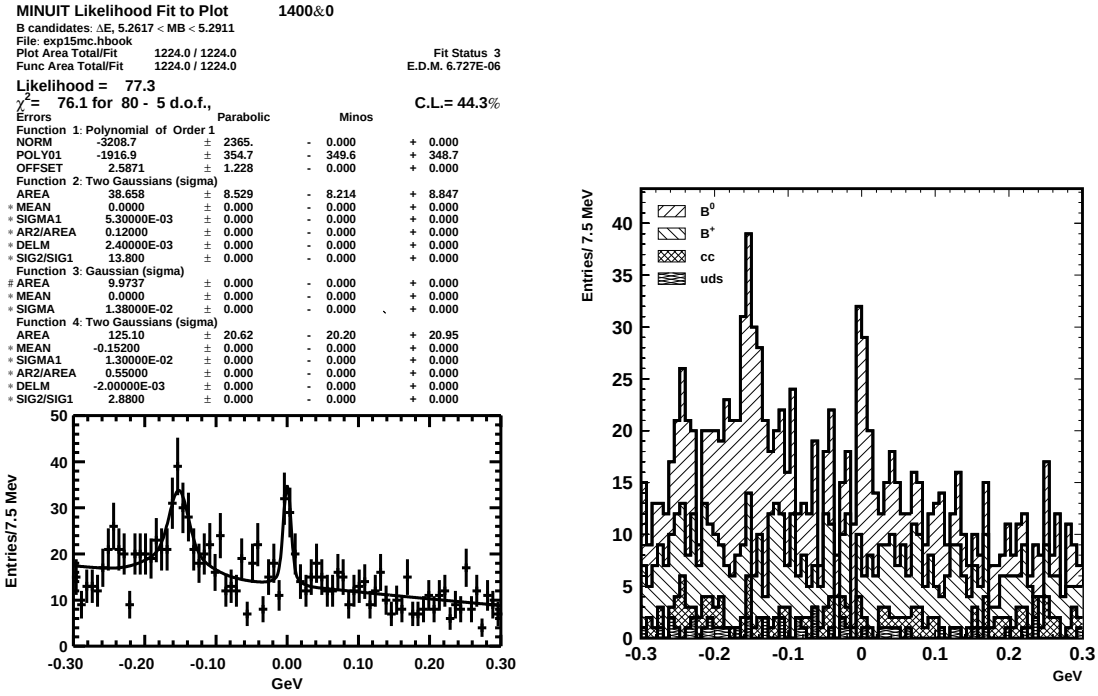

(a) ΔE

(b) ΔE, breakdown by type

Figure 5.10: ΔE for $B^0 \to D^{(*)0} D^{*-} K^+$ decays in generic MC.

5.2.2 $B^0 \to D^{*0} D^{*-} K^+$

The same test was performed for $B^0 \to D^{*0} D^{*-} K^+$ decays in the generic MC sample. The projection of the lower signal region from figure 5.8 onto the M_{bc} axis is displayed in figure 5.11.

The fit to the signal peak, which is detailed in figure 5.11(a), returns an area of 137.4 ± 20.9 events for the bifurcated Gaussian. The widths, σ_A and σ_B, were fixed to the results of the fit shown in figure 5.4(a). The branching ratio, calculated using the efficiency of equation 5.5, is

$$\mathcal{B}(B^0 \to D^{*0} D^{*-} K^+)_{\texttt{QQ98}} = (1.57 \pm 0.24) \times 10^{-2}. \tag{5.14}$$

In figure 5.11(b) the continuum and charged B contribution to the decay appears to be flat under the signal peak. This also reflects the absence of $B^+ \to D^{*+} D^{*-} K^+$ events in the MC sample.

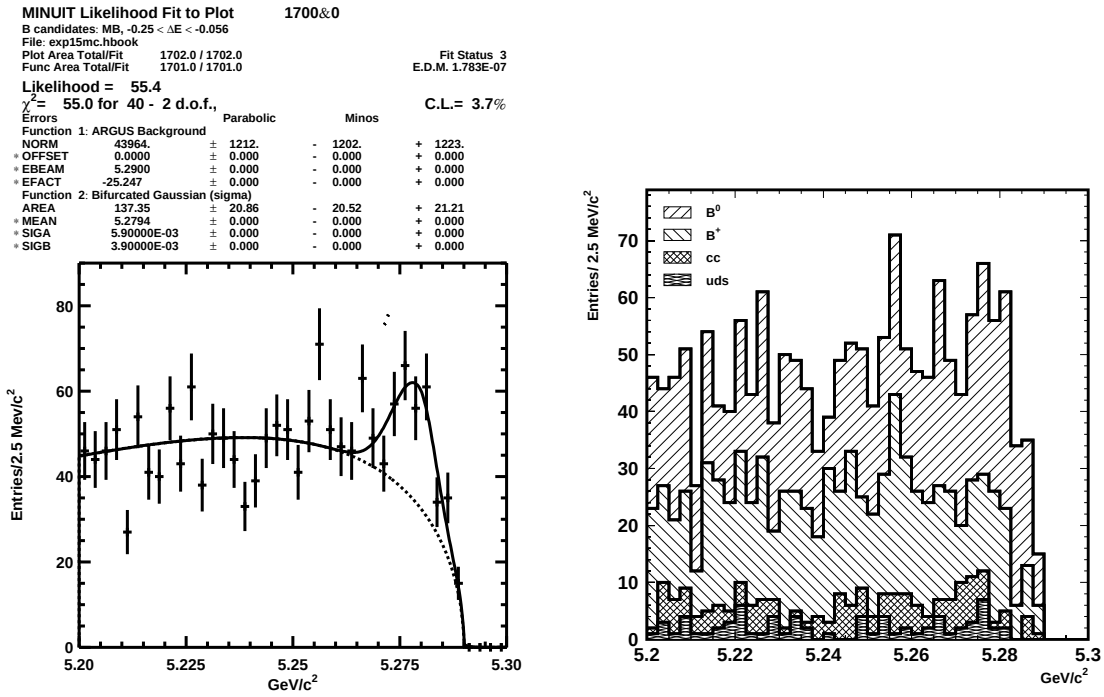

(a) M_{bc}

(b) M_{bc}, breakdown by type

Figure 5.11: M_{bc} for $\bar{B}^0 \to D^{*+}\bar{D}^{*0}K^-$ decays in generic MC.

Chapter 6

Results and Analysis

6.1 Reconstruction in on–resonance data

The analysis procedure discussed in the preceding chapters was used to reconstruct doubly charmed B meson decays from the Belle data set that was prepared for the XXXI International Conference on High Energy Physics – ICHEP 2002, in July 2002. The entirety of the $78.13\ \mathrm{fb}^{-1}$ data set described in §4.1, which consists of experiments 7 through 19, was analysed using the `b20020703_0706` version of the Belle software.

6.1.1 $B^+ \to D^{*+}D^{*-}K^+$

The $B^+ \to D^{*+}D^{*-}K^+$ decays were reconstructed as described in §5.1.3. The M_{bc} vs ΔE scatter plot is shown in figure 6.1(b) with the signal region outlined by a box. The number of signal candidates was determined from a fit to the M_{bc} distribution of figure 6.1(c) with the width of the signal Gaussian fixed to $3.0\ \mathrm{MeV}/c^2$. Only B meson candidates with a missing energy that satisfied a cut of $|\Delta E| < 24\ \mathrm{MeV}$ were included in the plot of figure 6.1(c). Similarly, the ΔE distribution of figure 6.1(a) only includes candidates with M_{bc} within a 3σ region around the B meson mass.

The area of the M_{bc} signal peak is 9.1 ± 3.8 events. The statistical significance of the fit is given by

$$\sqrt{-2\ln(\mathcal{L}(0) - \mathcal{L}_{\max})}, \tag{6.1}$$

where $\mathcal{L}_{\max}$ is the likelihood of the fit with the nominal signal yield, and $\mathcal{L}(0)$ is the likelihood with the signal yield set to zero. The fit of figure 6.1(c) has a statistical significance of 2.9σ.

To check this fit, the signal yield was also calculated from the ΔE distribution with a fit using the double Gaussian shape measured in figure 5.6(b). This fit of the ΔE spectrum indicates that there are only 1.5 ± 3.0 events, essentially a null result. It is possible that the peak in M_{bc} is created by incorrectly

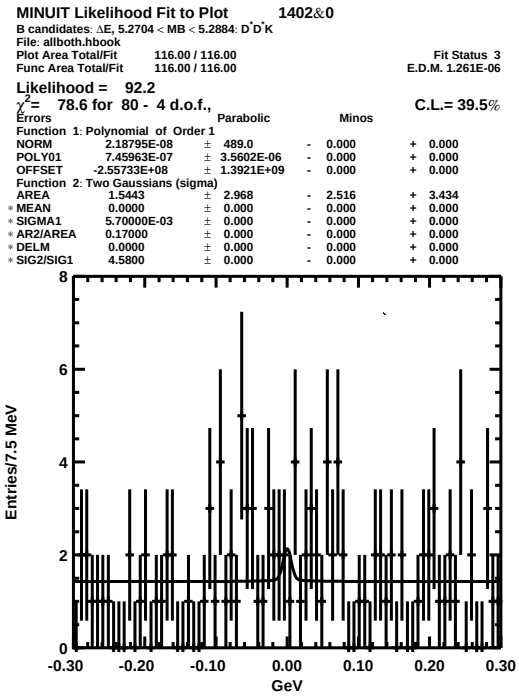

(a) ΔE for $5.2704 < M_{bc} < 5.2884$

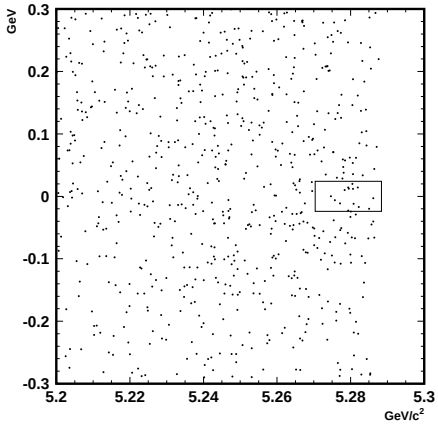

(b) M_{bc} vs. ΔE

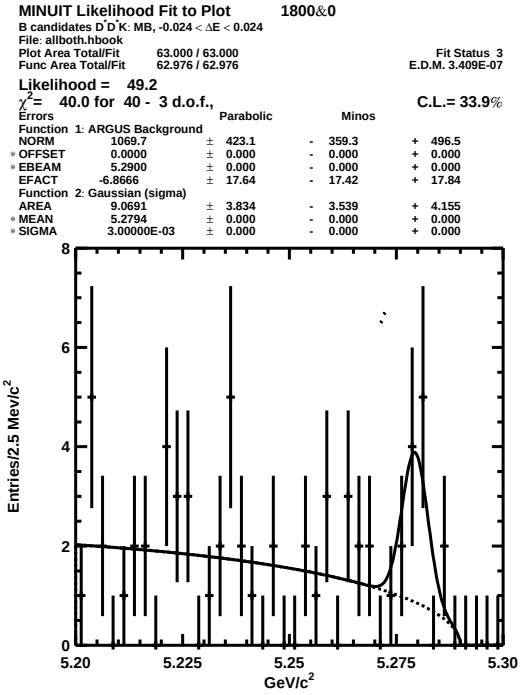

(c) M_{bc} for $-0.024 < \Delta E < 0.024$

Figure 6.1: M_{bc} and ΔE distributions for $B^+ \to D^{*+}D^{*-}K^+$, 78.13 fb^{-1} data set.

reconstructed D^* candidates. If a D^0 meson candidate is combined with a track that is not in fact a slow pion from a D^* decay, then it is feasible that a peak may be observed in the M_{bc} spectrum but not in the ΔE spectrum.

While it is possible to calculate a central value of the branching ratio for these decays using the fit to the M_{bc} spectrum, not much statistical significance can be assigned to the result, particularly as the yield from the ΔE spectrum is not in agreement.

6.1.2 $B^0 \to D^{(*)0} D^{*-} K^+$

Partly because there is no requirement for a second $D^* \to D^0\pi$ decay, the reconstruction of $B^0 \to D^0 D^{*-} K^+$ has a higher efficiency and results in significantly more candidates than that of $B^+ \to D^{*+} D^{*-} K^+$, as can be seen in figure 6.2(b). As discussed in §5.1.2, the ΔE distribution from a full reconstruction of $B^0 \to D^0 D^{*-} K^+$ also contains events from $B^0 \to D^{*0} D^{*-} K^+$ and $B^+ \to D^{*+} D^{*-} K^+$.

The background shape of the two M_{bc} distributions of figures 6.2(a) and 6.2(c) is fitted using the ARGUS function of equation 5.1. The shape parameter, a, was determined in a two dimensional fit to the entire area of figure 6.2(b). For this fit the background in ΔE is assumed to be flat and linear, and the background in M_{bc} is expected to follow the ARGUS shape. The two dominant signal peaks of $B^0 \to D^0 D^{*-} K^+$ and $B^0 \to D^{*0} D^{*-} K^+$ were modelled with two dimensional Gaussian functions. The means and widths of these Gaussians were fixed to the weighted averages described in tables 5.2 and 5.3. Figure 6.3 demonstrates the shape of the fitted functions.

The signal yields are calculated from fits to the M_{bc} distributions of figures 6.2(a) and 6.2(c). A slice representing a 3.5σ region around $\Delta E = 0$ was projected onto M_{bc} to produce the spectrum of figure 6.2(a). This figure displays the M_{bc} signal peak for $B^0 \to D^0 D^{*-} K^+$ decays with the requirement that $|\Delta E| < 28\ \mathrm{MeV}$. The width of the Gaussian used to fit the peak was fixed to $3.0\ \mathrm{MeV}/c^2$, which was determined from figure 5.3(a). There are (91.8 ± 18.0) $B^0 \to D^0 D^{*-} K^+$ event candidates from this fit.

The M_{bc} distribution of figure 6.2(c) was histogrammed for candidates satisfying $|\Delta E + 0.152| < 98\ \mathrm{MeV}$. The signal peak was fitted using a bifurcated Gaussian with $\sigma_A = 5.9\ \mathrm{MeV}/c^2$ and $\sigma_B = 3.9\ \mathrm{MeV}/c^2$. The area of the Gaussian in this fit is 499.6 ± 45.0 events.

These yields are cross checked by fitting the ΔE distribution of figure 6.2(d). Here the shifted peak was fitted using a double Gaussian with means and widths fixed to the parameters determined from the experiment 15 MC study. The peak centred around zero was modelled using the triple Gaussian shape of figure 5.3(b). This central peak has an area of 91.4 ± 20.7 events, and the shifted peak has an area of 417.0 ± 44.5 events. These signal yields do not suggest that the M_{bc} fit results are biased or incorrect.

However, as discussed in §5.1.2, the shifted peak in ΔE can contain events from $B^+ \to D^{*+} D^{*-} K^+$ decays. Using the fake rate, $\bar{\epsilon}(B^+ \to D^{*+} D^{*-} K^+)^\dagger$, of equation 5.11, and the yield measured in §6.1.1 the contribution of these charged B meson decays to the signal peak of figure 6.2(c) is estimated to be 33.8 ± 14.3 events.

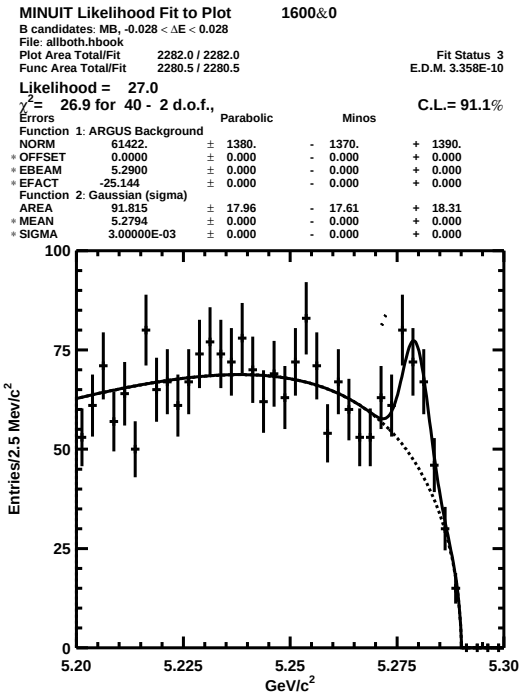

(a) M_{bc} for $-0.028 < \Delta E < 0.028$

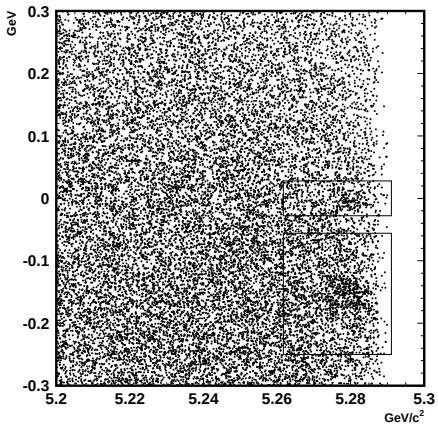

(b) M_{bc} vs. ΔE

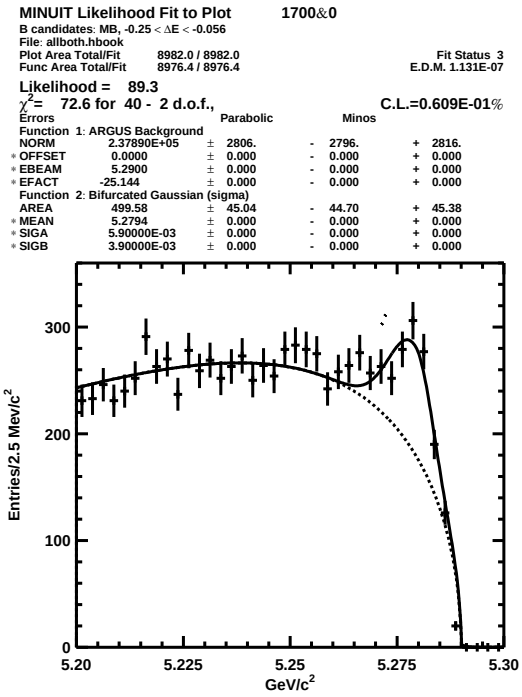

(c) M_{bc} for $-0.098 < \Delta E + 0.152 < 0.098$

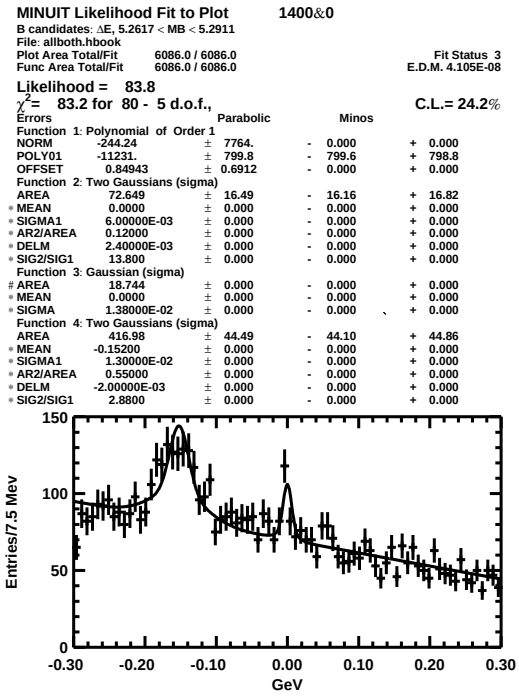

(d) ΔE for $5.2617 < M_{bc} < 5.2911$

Figure 6.2: M_{bc} and ΔE distributions for $B^0 \to D^{(*)0} D^{*-} K^+$, 78.13 fb^{-1} data set.

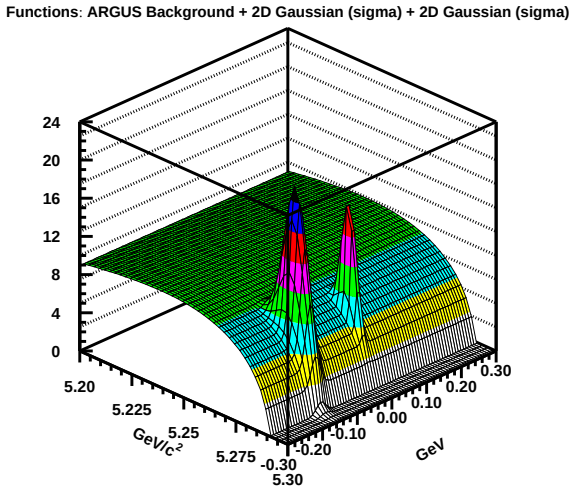

Figure 6.3: Two dimensional fi t to M_{bc} and ΔE distributions for $B^0 \to D^{(*)0}D^{*-}K^+$, 78.13 fb^{-1} data set.

By adding another bifurcated Gaussian to the fit of figure 6.2(c), with a fixed area of 33.8, and fixed widths of $\sigma_A = 4.5$ MeV$/c^2$ and $\sigma_B = 3.3$ MeV$/c^2$, the yield for $B^0 \to D^{*0}D^{*-}K^+$ is determined to be 461.8 ± 45.1, as shown in figure 6.4.

The signal to background ratio of the $B^0 \to D^{(*)0}D^{*-}K^+$ spectrum can be improved by only looking at the five decay submodes where either the D^0 or $\bar{D}^0$ meson decays to the $K\pi$ final state. When this further requirement is imposed on candidate events the signal peaks become much clearer, which can be seen in figure 6.5.

The signal yield for $B^0 \to D^0D^{*-}K^+$ decays in figure 6.5(a) is 66.9 ± 10.6 events, and in figure 6.5(c), the area of the M_{bc} peak is 261.5 ± 23.4 events. The contribution from the $B^+ \to D^{*+}D^{*-}K^+$ process to this second peak is estimated to be 19.2 ± 8.1 events. This leads to an estimated yield of 240.5 ± 23.4 events for $B^0 \to D^{*0}D^{*-}K^+$, as shown in the fit of figure 6.6.

These yields are consistent with the results of the ΔE fit in figure 6.5(d), where the central peak has an area of 57.1 ± 11.52 events, and the shifted peak contains 215.97 ± 23.7 events.

6.1.3 $B^0 \to D^{*+}D^{*-}K_S$

The distributions of M_{bc} and ΔE for reconstructed $B^0 \to D^{*+}D^{*-}K_S$ decays have remarkably little background, as can be seen in figure 6.7. Despite the very low efficiency for this decay mode, an increase in the density of the M_{bc} vs ΔE scatter plot can be seen inside the signal box shown in figure 6.7(b).

The signal yield in M_{bc}, determined from the fit of figure 6.7(c), is 13.1 ± 3.8 events. The area of the ΔE distribution of figure 6.7(a), which is 10.4 ± 3.5 events, is in good agreement with this. The M_{bc} peak

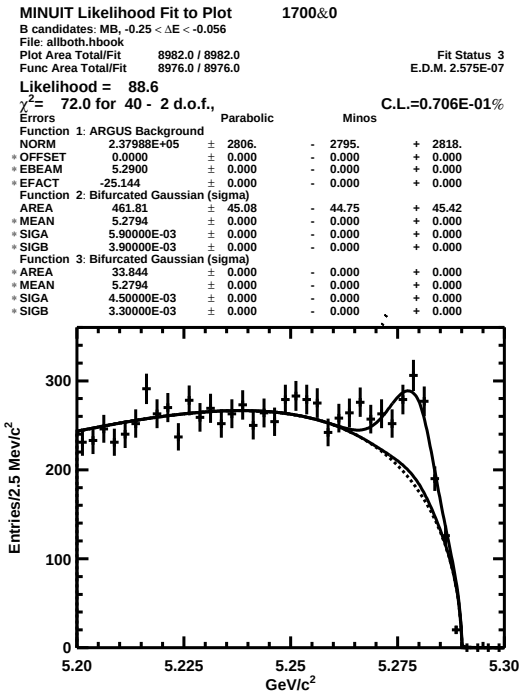

Figure 6.4: Corrected fit of M_{bc} for $B^0 \to D^{*0}D^{*-}K^+$ candidates.

has a statistical significance of 6.1σ.

6.2 Dalitz plots

Dalitz plots of candidates in the $B^0 \to D^0D^{*-}K^+$ and $B^0 \to D^{*0}D^{*-}K^+$ signal regions are shown in figure 6.8. Any evidence of the intermediate resonances predicted by Colangelo and De Fazio [68] may manifest as bands or some other structure in these Dalitz plots. The Dalitz plots of figures 6.8(c) and 6.8(d) are not strictly correct, since the momentum of the D^{*0} candidate is not determined in the reconstruction method of §5.1.2. They are more contracted in s than they should be, due to the missing π^0 or photon momentum. Nonetheless, they provide some insight into the nature of the $B^0 \to D^{*0}D^{*-}K^+$ transition.

Following the convention of Ref. [68] the parameters s and s_- are defined as

$$\begin{aligned} s &= (p_{D^{(*)0}} + p_K)^2, \text{ and} \\ s_- &= (p_{D^{*-}} + p_K)^2, \end{aligned} \tag{6.2}$$

where $p_{D^{*-}}$ is the momentum of the charged D^*, $p_{D^{(*)0}}$ is the momentum of the D^{*0} or D^0, and p_K is the momentum of the prompt kaon.

Since there is a significant level of background events below the signal region in figures 6.2(a) and 6.2(c)

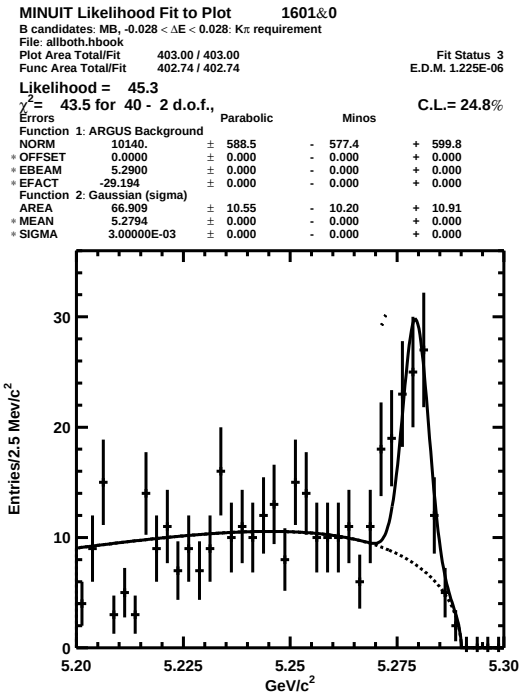

(a) M_{bc} for $-0.028 < \Delta E < 0.028$

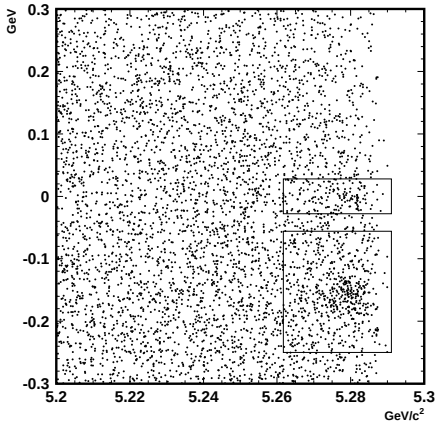

(b) M_{bc} vs. ΔE

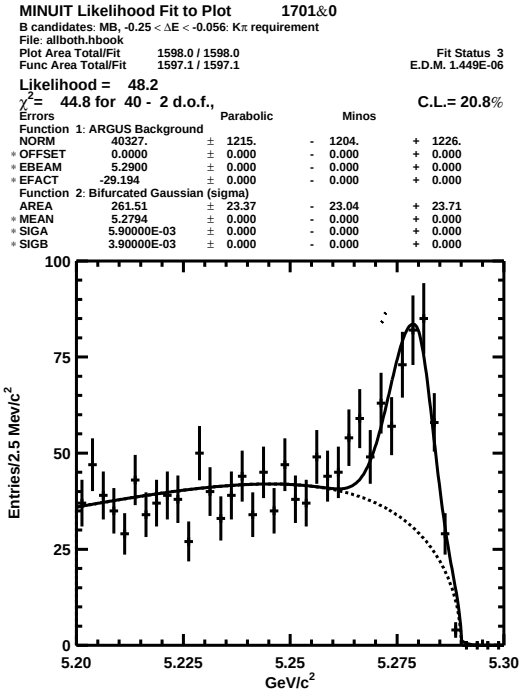

(c) M_{bc} for $-0.098 < \Delta E + 0.152 < 0.098$

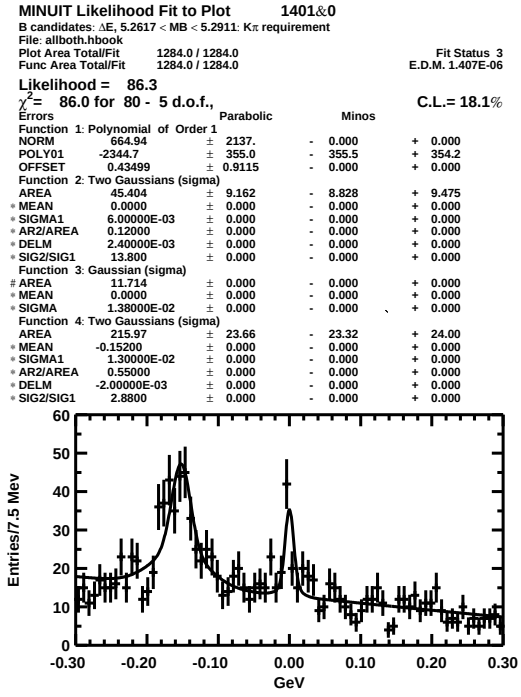

(d) ΔE for $5.2617 < M_{bc} < 5.2911$

Figure 6.5: M_{bc} and ΔE distributions for $B^0 \to D^{(*)0} D^{*-} K^+$, 78.13 fb^{-1} data set, requiring one $D^0 \to K\pi$.

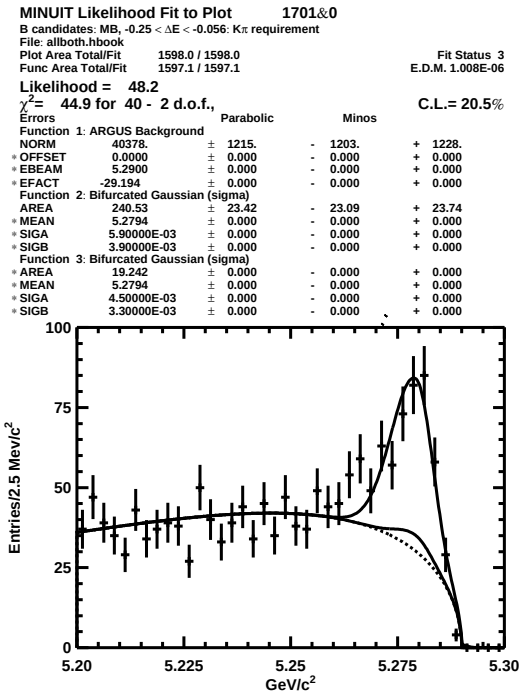

Figure 6.6: Corrected fi t of M_{bc} for $B^0 \to D^{*0}D^{*-}K^+$ candidates, requiring one $D^0 \to K\pi$.

the corresponding Dalitz plots also contain a large number of background events. To obtain a clearer view of the resonant structure of these doubly charmed decays, Dalitz plots were also generated for the cases where at least one D^0 or $\bar{D}^0$ candidate decayed to the $K\pi$ final state. The concentration of events in a band around $s = 6.5$ can be seen more clearly in figures 6.8(b) and 6.8(d).

The parameter s is the square of the invariant mass of the $D^{(*)0}K$ combination. From their results shown in figure 2.9, Colangelo and De Fazio predicted that the major resonant contribution to $B^0 \to D^0D^{*-}K^+$ or $B^0 \to D^{*0}D^{*-}K^+$ is from the intermediate D_{s0} or D^*_{s1} state respectively. The theoretically predicted Dalitz plots of figures 2.10(b) and 2.11(b) primarily vary along the direction of s, which is the axis dependent on the strong transition of equation 2.69. Therefore a study of s in $B^0 \to D^0D^{*-}K^+$ candidate events can be used to search for the D_{s0} resonance. Unfortunately it is not possible to search for the D^*_{s1} resonance using this sample of $B^0 \to D^{*0}D^{*-}K^+$ decays, since this analysis does not completely determine $p_{D^{*0}}$, as previously mentioned.

Figure 6.9 illustrates the projection of the Dalitz plots of figure 6.8 onto the s and s_- axes for $B^0 \to D^0D^{*-}K^+$ candidate events. In each case the solid histogram represents the signal region, and the dotted points with error bars represent the expected shape of phase space decays. The shape of these phase space decays was determined from a side band in the M_{bc} vs ΔE distribution. This side band is the projection of s and s_- for B meson candidates which satisfy $|\Delta E| < 10$ MeV and $5.22 < M_{bc} < 5.26$ GeV$/c^2$. The

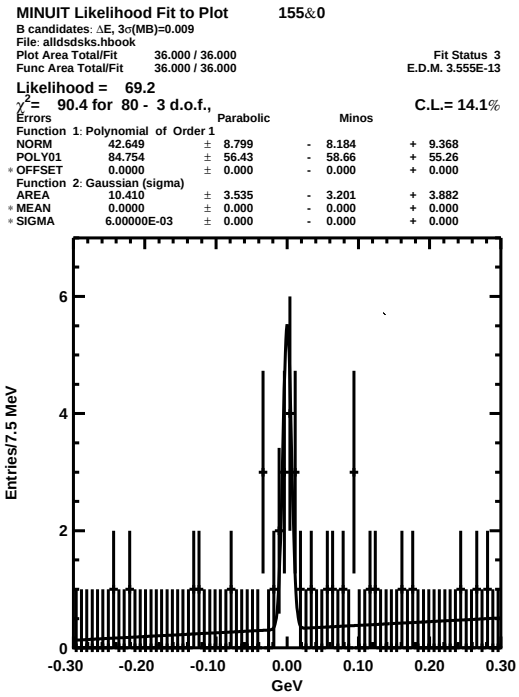

(a) ΔE for $5.2704 < M_{bc} < 5.2884$

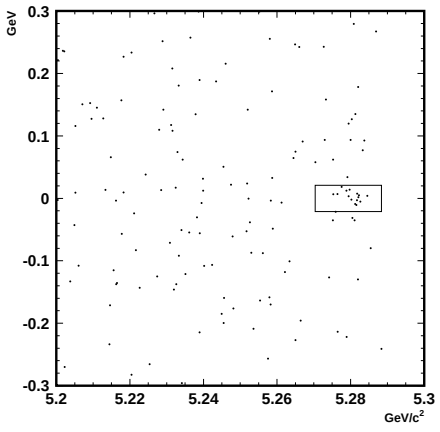

(b) M_{bc} vs. ΔE

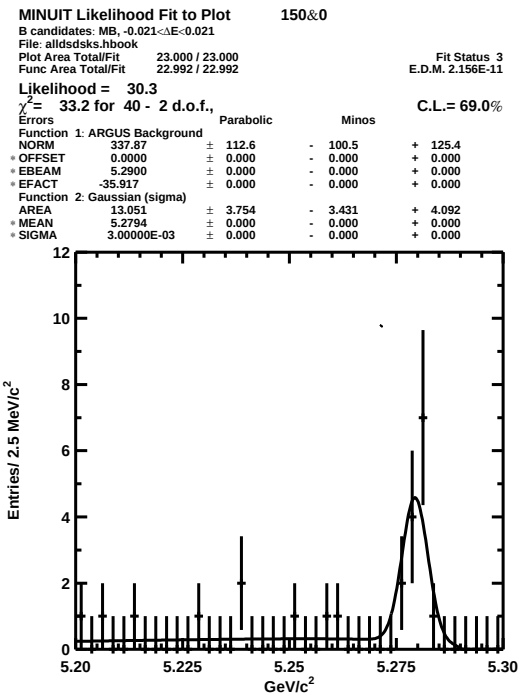

(c) M_{bc} for $-0.021 < \Delta E < 0.021$

Figure 6.7: M_{bc} and ΔE distributions for $B^0 \to D^{*+}D^{*-}K_S$, 78.13 fb^{-1} data set.

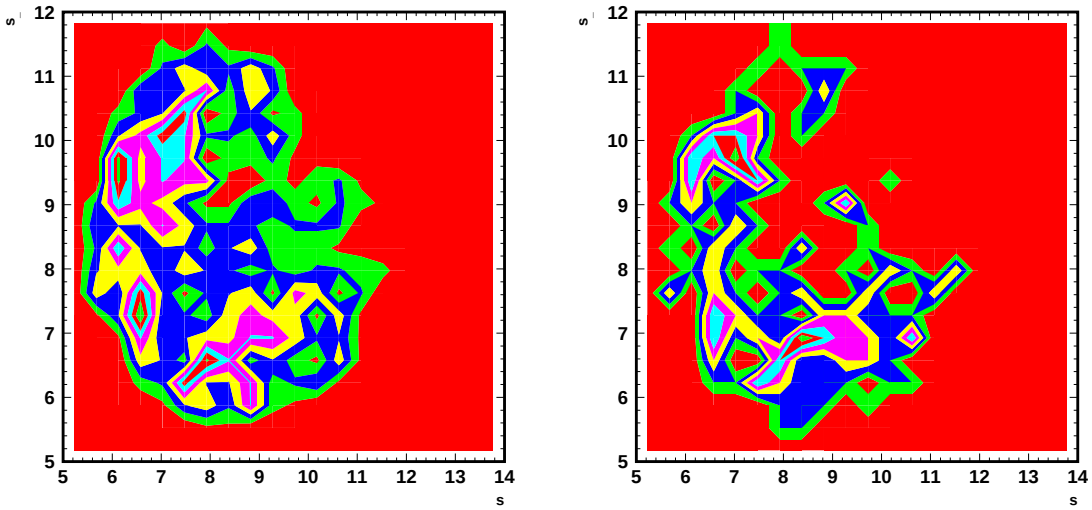

(a) $B^0 \to D^0 D^{*-} K^+$

(b) $B^0 \to D^0 D^{*-} K^+$, $K\pi$ requirement

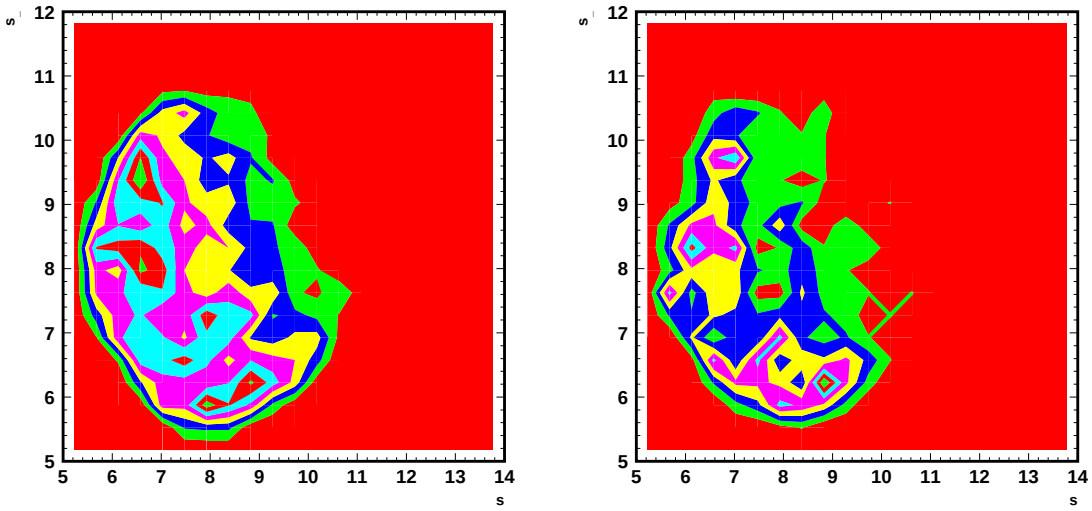

(c) $B^0 \to D^{*0} D^{*-} K^+$

(d) $B^0 \to D^{*0} D^{*-} K^+$, $K\pi$ requirement

Figure 6.8: Dalitz plots. The contours are equally spaced.

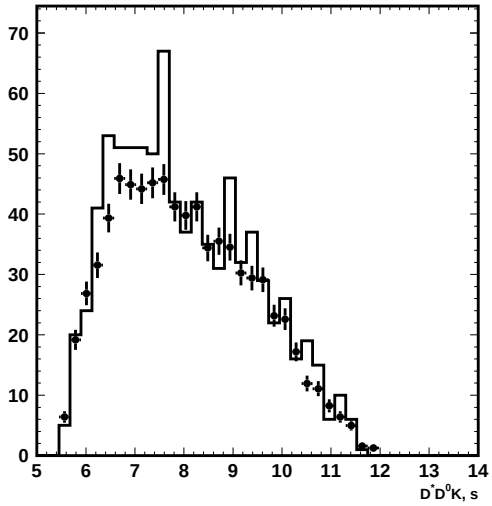

(a) $(p_{D^0} + p_K)^2$

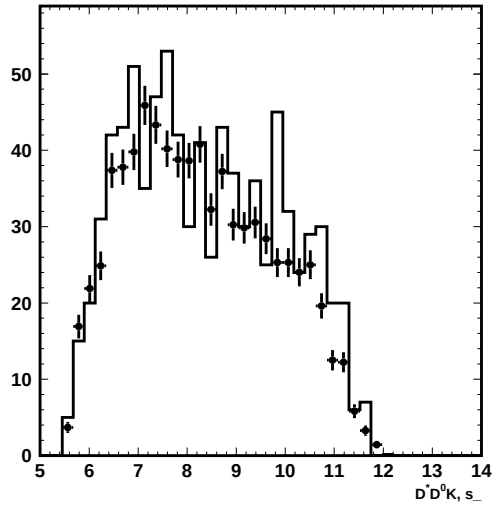

(b) $(p_{D^{*-}} + p_K)^2$

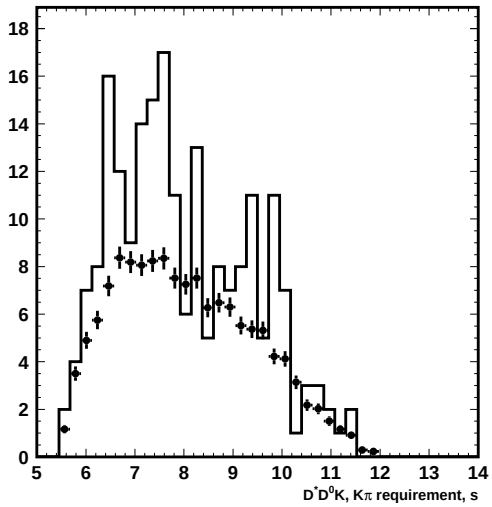

(c) $(p_{D^0} + p_K)^2$, $K\pi$ requirement

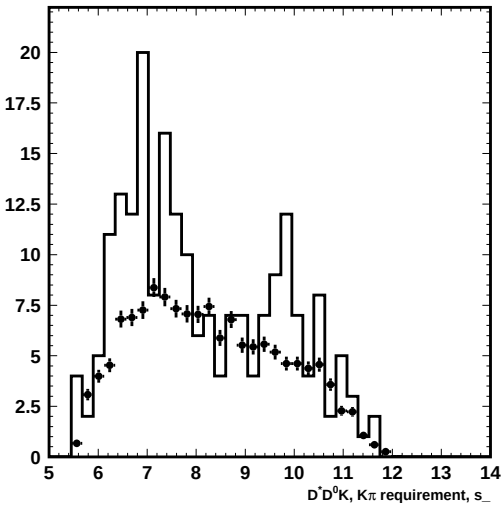

(d) $(p_{D^{*-}} + p_K)^2$,$K\pi$ requirement

Figure 6.9: Projections of s and s_- for $B^0 \to D^0 D^{*-} K^+$. The solid histograms represent the signal region, and the dotted points with error bars represent the expected shape of phase space decays.

background histograms are normalised to the number of background events in figures 6.2(a) and 6.5(a).

A slight excess of events can be seen above the background in the region of $s = 6.5$ in figure 6.9(a), and also around $s = 9$, but it is difficult to assess the significance of these peaks due to the large number of background events. The first peak appears more pronounced in figure 6.9(c), as does the second which also appears considerably broader. However, the low number of events in the $K\pi$ requirement sample makes it difficult to speculate as to how significant these are.

Perhaps a more intuitive appreciation of the resonant structure can be gained by looking at the $m(D^0K) - m(D^0)$ and $m(D^*K) - m(D^*)$ spectra shown in figure 6.10. These distributions have many of the same properties of the $m(D^0\pi_s) - m(D^0)$ spectra for D^* candidates in figure 4.11. Hence the background shape here is modelled with a threshold function similar to equation 4.16, but with $m(K^+)$ replacing $m(\pi^+)$.

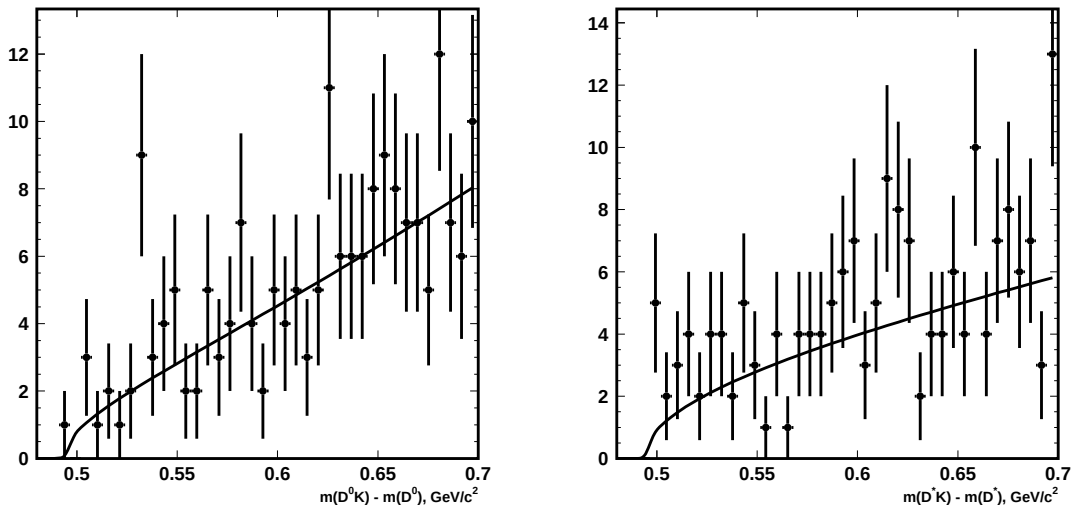

(a) $m(D^0K) - m(D^0)$ (b) $m(D^*K) - m(D^*)$

Figure 6.10: Mass differences for $B^0 \to D^0 D^{*-} K^+$ decays

Unfortunately there are not enough events in figure 6.10(a) to state conclusively that any intermediate resonances are seen. There appears to be some enhancement in the region $m(D^0K) - m(D^0) = 0.53$, and perhaps at 0.58 as well. The bins around $m(D^0K) - m(D^0) = 0.65$ are also slighlty higher than the fitted background shape. This is region is the approximate area any enhancement due to $D_{s1}(2536)^{\pm}$ or $D_{sJ}(2573)^{\pm}$ decays to D^0K^+ would be expected. However, these enhancements are certainly not significant enough to draw any inference regarding the presence of intermediate resonances.

The equivalent plot of $m(D^*K) - m(D^*)$ in figure 6.10(b) is much the same. There is a slight excess in some bins, but the total number of events is too small to make any definitive statement. It should be noted that according to Colangelo and De Fazio's work no enhancements due to hadronic resonances are to

be expected in figure 6.10(b), since the strong transition in $B^0 \to D^0 D^{*-} K^+$ decays is predicted to occur via $D_s^X \to D^0 K^+$.

6.3 Branching Fractions

The branching fraction for each B meson decay mode is calculated as

$$\mathcal{B} = \frac{Y_{\rm fit}}{2 \times f_{00} \times N(B\bar{B}) \times \bar{\epsilon}} \,, \tag{6.3}$$

where $Y_{\rm fit}$ is the signal yield, $f_{00} = 0.5$ is the branching fraction of $\Upsilon(4S) \to B^0 \bar{B}^0$, and $N(B\bar{B}) = 84.97 \times 10^6$ is the number of $B\bar{B}$ events. The efficiency, $\bar{\epsilon}$, is the weighted average of the reconstruction efficiencies measured using the experiment dependent signal MC data.

The branching ratios, calculated using all nine $D^0 \otimes \bar{D}^0$ submodes, are summarised in table 6.1. The errors quoted are due to the statistical uncertainty in the determination of the signal yield in each case. If

	Branching ratio	
Mode		$K\pi$ requirement
$B^0 \to D^0 D^{*-} K^+$	$(1.66 \pm 0.33) \times 10^{-3}$	$(2.08 \pm 0.33) \times 10^{-3}$
$B^0 \to D^{*0} D^{*-} K^+$	$(8.17 \pm 0.80) \times 10^{-3}$	$(7.51 \pm 0.73) \times 10^{-3}$
$B^+ \to D^{*+} D^{*-} K^+$	$(1.06 \pm 0.45) \times 10^{-3}$	
$B^0 \to D^{*+} D^{*-} K^0$	$(7.05 \pm 2.03) \times 10^{-3}$	

Table 6.1: Branching ratios.

only the five submodes containing a $D^0 \to K\pi$ decay are used the results in the right column of table 6.1 are obtained. There are not enough events in the $B^+ \to D^{*+} D^{*-} K^+$ and $B^0 \to D^{*+} D^{*-} K_S$ candidate M_{bc} and ΔE spectra when the $K\pi$ requirement is imposed to warrant measuring a branching ratio.

6.4 Systematic errors

Many of the parameters used to determine the branching ratios of table 6.1 are determined from a study of Monte–Carlo events in which the behaviour of the detector is simulated. However, as good as the `GEANT` based simulation software is, it is not perfect. Therefore it is necessary to identify the differences between the behaviour of the Belle detector and the MC simulation of it. For instance, there is a well known discrepancy in the resolution of invariant mass peaks when comparing MC events to data collected from KEKB. The MC mass peaks are systematically narrower than those seen in on resonance data. Since the same mass cuts are used in both analyses, more events will pass the cuts when studying MC than when studying on resonance data. Hence systematically more events will be reconstructed in MC, and the efficiency used in equation 6.3 will be overestimated. Some of these sorts of effects are greater than others,

and it is not always possible to correct for them. However, it is possible to estimate the maximum impact they are likely to make on the final result.

In any event, the dominant uncertainty in the reconstruction of $B \to D\bar{D}K$ decays is the uncertainty in the tracking efficiency of the Belle detector. As this uncertainty is so large, further understanding and reduction of the other errors only has a marginal effect in reducing the combined error.

The systematic errors in the calculation of the branching fractions for $B^0 \to D^0 D^{*-} K^+$ and $B^0 \to D^{*0} D^{*-} K^+$ are summarised in table 6.2. These errors are added in quadrature to give a total error due to systematic uncertainties of $^{+21}_{-23}\%$ in the first case, and $^{+22}_{-24}\%$ in the latter.

Source	Error (%)	
	$B^0 \to D^0 D^{*-} K^+$	$B^0 \to D^{*0} D^{*-} K^+$
$N(B\bar{B})$	± 1	± 1
Fitting parameters	± 3 $\quad \pm 2^\dagger$	± 3 $\quad \pm 3^\dagger$
Tracking	± 17	± 17
π^0 reconstruction	± 3	± 3
Particle identification	± 7 $\quad \pm 8^\dagger$	± 7 $\quad \pm 8^\dagger$
Intermediate branching fractions	± 5 $\quad \pm 4^\dagger$	± 5 $\quad \pm 4^\dagger$
Reconstruction efficiency	± 2	± 2
π^0 selection	-3	-3
D^0 selection	$^{+3}_{-11}$	$^{+3}_{-11}$
D^* selection	$+5$	$+5$
$\mathcal{B}(B^+ \to D^{*+} D^{*-} K^+)$	n/a	$^{+7}_{-5}$
Total	$^{+21}_{-23}$	$^{+22}_{-24}$

Table 6.2: Systematic errors in the calculation of the branching fractions. Errors marked with a † denote those with the $D^0 \to K\pi$ requirement.

The uncertainty in $\mathcal{B}(B^+ \to D^{*-} D^{*+} K^+)$ is estimated in a similar manner as for $\mathcal{B}(B^0 \to D^0 D^{*-} K^+)$, but an extra 3% is added to the tracking error to account for the second slow pion. The uncertainty in the reconstruction efficiency is also larger, at 5%, due to lower statistics in the signal MC distributions of figure 5.6(a). These additional uncertainties have very little effect on the overall uncertainty due to the dominance of the tracking error. The uncertainty is $^{+25}_{-27}\%$. Similarly, the low signal yield for the reconstruction of $B^0 \to D^{*+} D^{*-} K_S$ makes it impossible to study the error due to systematic uncertainties for the calculation of $\mathcal{B}(B^0 \to D^{*+} D^{*-} K^0)$ in much detail. The errors assumed for both of these decays are listed in table 6.3.

6.4.1 $N(B\bar{B})$

The total number of $B\bar{B}$ events in the $78.13\ \mathrm{fb}^{-1}$ data set used in this analysis is summarised in table 4.1. The branching ratios were calculated using $N(B\bar{B}) = 84,456,599$. The statistical error of 0.6% is considered as a systematic error due to the uncertainty in $N(B\bar{B})$.

Source	Error (%)	
	$B^+ \to D^{*+}D^{*-}K^+$	$B^0 \to D^{*+}D^{*-}K^0$
$N(B\bar{B})$	± 1	± 1
Fitting parameters	± 2	± 1
Tracking	± 22	± 24
K_S reconstruction	n/a	± 3
π^0 reconstruction	± 3	± 3
Particle identification	± 7	± 7
Intermediate branching fractions	± 5	± 5
Reconstruction efficiency	± 5	± 7
π^0 selection	-3	-3
D^0 selection	$^{+3}_{-11}$	$^{+3}_{-11}$
D^* selection	$+5$	$+5$
Total	$^{+25}_{-27}$	$^{+27}_{-29}$

Table 6.3: Systematic errors assumed in the calculation of the branching fractions for $B^+ \to D^{*+}D^{*-}K^+$ and $B^0 \to D^{*+}D^{*-}K^0$ decays.

6.4.2 Fitting

As described in §6.1.1 and §6.1.2 the shape of the ARGUS background and the width of the signal peak are fixed when determining the signal yield in the M_{bc} distributions. To estimate the effect that this has, each of these parameters were varied by $\pm 1\sigma$.

$B^0 \to D^0 D^{*-} K^+$

In the fit of figure 6.2(a) the peak width was fixed to $3.0\ \mathrm{MeV}/c^2$ which was determined from the results listed in table 5.2. The uncertainty of this width is $\pm 0.1\ \mathrm{MeV}/c^2$. Increasing the signal peak's width by 1σ increased the yield by 1.6%. Decreasing the width by 1σ reduced the yield by 1.7%. When the width was allowed to float it was fitted to be $3.2 \pm 0.6\ \mathrm{MeV}/c^2$, which is consistent with the result of the MC study.

Varying the shape of the ARGUS function by $\pm 1\sigma$ affected the yield by $\pm 2.5\%$. When the shape parameter, a, was allowed to float it was fitted to a value of -26.2 ± 2.7, as compared with $a = -25.1 \pm 0.7$ from the two dimensional fit of figure 6.2(b).

Taking the largest of these effects, the systematic error due to uncertainties in the fit of figure 6.2(a) is taken to be $\pm 2.5\%$.

The uncertainty in the fit of figure 6.5(a), where are least one D^0 meson was required to decay to the $K\pi$ final state, is marginally smaller than the above. Varying the ARGUS shape parameter, a, by $\pm 1\sigma$ changes the branching ratio measurement by $\pm 0.9\%$. When a was allowed to float the fit was skewed dramatically due to the low statistics in the left portion of figure 6.5(a). Since part of the methodology in determining the shape of the ARGUS function from a sideband is to make use of the larger statistics which are possibly available from a fit to a bigger area, this is not too concerning.

Modifying the fixed width of the M_{bc} peak in the fit of figure 6.5(a) only affected the branching ratio measurement by $\pm 1.6\%$. When the width was released as a free parameter it was fitted to be 3.6 ± 0.6 MeV/c^2, which is a distortion due to the two bins just to the left of the peak in figure 6.5(a). However, this fitted width is not inconsistent with the fixed value of 3.0 ± 0.1 MeV/c^2 determined in the experiment 15 MC study. The systematic error is taken to be $\pm 1.6\%$.

$B^0 \to D^{*0} D^{*-} K^+$

Variations in σ_A and σ_B have very little effect on the estimation of the signal yield in the fit of figure 6.4. The largest effect is due to varying σ_A by $\pm 1\sigma$ which varies the yield by $\pm 2.2\%$. If the widths are left as free parameters they are fitted to be $\sigma_A = 6.1 \pm 1.5$ MeV/c^2 and $\sigma_B = 3.0 \pm 0.3$MeV/c^2. If the ARGUS shape was varied by $\pm 1\sigma$ the yield varied by $\pm 2.8\%$. The systematic error is taken to be 2.8%.

Again, for the fit of figure 6.5(c) variations in σ_B made very little difference to the total yield, but changing σ_A by $\pm 1\sigma$ altered the branching ratio by $\pm 2.3\%$. Modifying the ARGUS shape parameter, a by $\pm 1\sigma$ changes the yield by $^{+1.9}_{-1.1}\%$. The greater of these, due to variations in the width of the signal peak, is taken as the systematic error for $B^0 \to D^{*0} D^{*-} K^+$ reconstructions requiring a $D^0 \to K\pi$ decay.

$B^+ \to D^{*+} D^{*-} K^+$

Varying the width of the Gaussian function used to determine the signal yield for $B^+ \to D^{*+} D^{*-} K^+$ by $\pm 1\sigma$ varied the estimation of the branching ratio by $\pm 2.2\%$. Due to the low number of events in figure 6.1(c) it is difficult to cross check the fixed width in table 5.7. Allowing it to float resulted in a fit with a width of $\sigma = 1.7 \pm 0.6$ MeV/c^2, and a yield of 7.9 ± 3.4 events. The width is changed significantly from the fixed value of 3.0 ± 0.2 MeV/c^2. This perhaps only serves to reinforce that this result is not significant enough to claim a branching ratio measurement.

$B^0 \to D^{*+} D^{*-} K^0$

The signal yield of figure 6.7(c) is quite insensitive to variations in the width of the peak, varying by only $\pm 0.3\%$. Changes in a also only affected the final branching ratio measurement by $\pm 0.4\%$, which is the systematic error quoted for this fit.

6.4.3 Charged track detection efficiency

In the full reconstruction of $B^0 \to D^0 D^{*-} K^+$ decays at least 6 charged tracks must be detected, one of which is a slow pion. In the case where both the D^0 and $\bar{D}^0$ decay to a $K\pi\pi\pi$ final state there are 10 charged tracks. The uncertainty in the tracking efficiency is therefore 6 to 10 times larger than the single track uncertainty. On average there are 6.6 tracks per event, which is calculated by taking a weighted average of all the submodes which contribute to the inclusive yield. With the extra requirement that at least

one D^0 decays to the $K\pi$ final state this average is lowered slightly to 6.3. The average number of tracks per signal event is similar in $B^0 \to D^{*0}D^{*-}K^+$ decays, and is rounded up to 7 tracks per event so as not to underestimate the uncertainty.

The reconstruction of $B^+ \to D^{*+}D^{*-}K^+$ decays requires one more track per event, increasing the average to 8 tracks per event. Reconstructions of $B^0 \to D^{*+}D^{*-}K_S$ events can require up to 12 completely reconstructed tracks. This is partly why the background level is so small in figure 6.7(c). These events on average contain 9 tracks.

The single track reconstruction uncertainty is determined by studying $\eta \to \pi^+\pi^-\pi^0$ and $\eta \to \gamma\gamma$ decays [100]. The branching ratios of these two decay channels are very precisely known and are implemented well in the MC generator, `QQ98`. The photon detection efficiency is cancelled by taking the ratio

$$\frac{N_{\rm data}(\eta \to \pi^+\pi^-\pi^0)/N_{\rm MC}(\eta \to \pi^+\pi^-\pi^0)}{N_{\rm data}(\eta \to \gamma\gamma)/N_{\rm MC}(\eta \to \gamma\gamma)} = \frac{\epsilon_{\rm data}(\pi^+\pi^-)}{\epsilon_{\rm MC}(\pi^+\pi^-)}, \tag{6.4}$$

where N is the signal yield of the relevant decay, and ϵ is the two track reconstruction efficiency. The single track reconstruction efficiency is determined by taking the square root of equation 6.4. Details of the fitting procedure can be found in [100]. At this level no significant difference is found between the tracking efficiency in data and MC. The square root of the fitting error is assigned as the tracking efficiency systematic error.

The latest study of the single track reconstruction uncertainty [101] quotes an error of 2% for each track with high transverse momentum. This estimate does not include CDC background events which are included in the signal MC. Therefore, as in the study of the $B \to D^{*\pm}D^{\mp}$ branching fraction made by Iwasaki [102], the uncertainty is overestimated because the degradation of tracking quality due to CDC background is taken into account in the signal MC. Estimating the uncertainty for the reconstruction with the average number of tracks, 7, the uncertainty due to tracking efficiency error is 14% for the $B^0 \to D^0D^{*-}K^+$ and $B^0 \to D^{*0}D^{*-}K^+$ reconstructions.

Following the $B \to D^{*\pm}D^{\mp}$ measurement [101], the uncertainty for the low momentum pion is taken to be 3%, from a study of $B^0 \to D^{*-}\pi^+$ decays [103]. The total tracking efficiency uncertainty is 17% for $B^0 \to D^0D^{*-}K^+$ and $B^0 \to D^{*0}D^{*-}K^+$. The reconstruction of $B^+ \to D^{*+}D^{*-}K^+$ requires an extra low momentum pion, which increases the tracking systematic error to 22%. The extra charged track required in $B^0 \to D^{*+}D^{*-}K_S$ reconstructions brings the total error due to tracking uncertainties for these decays to 24%.

6.4.4 K_S reconstruction

There is an additional uncertainty of 2.8% which is introduced in the reconstruction of the K_S candidate when employing the `goodKS_loose` cuts of Fang [97].

6.4.5 Neutral pion detection

The reconstruction of neutral pions has been extensively studied by the Belle collaboration [104]. The dominant uncertainties in the π^0 detection efficiency are due to cut selection, photon energy smearing, and a modest nonlinear energy response correction for the ECL. The quadratic sum of these is 3%.

Some 65% of the the doubly charmed decays being examined contain at least one neutral pion in the final state, and 17% contain two. When at least one $D^0 \to K\pi$ decay is required in the reconstruction at least 50% of the reconstructed events contain a π^0 candidate. Applying the same reasoning as Iwasaki [102] the uncertainty is estimated as 3%.

6.4.6 Particle identification

The performance of the particle identification was studied using $D^{*+} \to D^0(K\pi)\pi$ decays [105]. An uncertainty of 2% is assigned for each kaon, and 2% for each pion. All reconstructed events, except for $B^0 \to D^{*+}D^{*-}K_S$, contain three charged kaons. Some 30% of reconstructed events contain four or more pion candidates to which particle identification is applied[1]. With the $K\pi$ requirement this fraction is increased to 40%. There are only two charged pions in the other events.

The uncertainty due to kaon identification is then $2\% \times 3 = 6\%$, and for pion identification it is $2\% \times 4 = 8\%$ or $2\% \times 2 = 4\%$. Taking the uncertainty due to pion identification to be 5.2% the total uncertainty is 7%. The uncertainty due to pion identification is increased to 5.6% by the $K\pi$ requirement, and the total uncertainty is 8%. This error can also be used to estimate the error for the $B^+ \to D^{*+}D^{*-}K^+$ and $B^0 \to D^{*+}D^{*-}K^0$ reconstructions, since neither the extra slow pion, nor the charged pions from the K_S decay are subject to particle identification.

6.4.7 Intermediate branching fractions

Estimations of the contribution of each submode to the total yield are based on the determination of the reconstruction efficiency of each submode in signal MC, and on the relative branching ratio of each submode, as shown in equation 5.3. The relative branching ratios are calculated using the measurements of the D^0 and D^{*+} branching fractions in [7]. The uncertainty due to these measurements is 4.9% for all nine submodes, and 4.0% when only the five containing a $D^0 \to K\pi$ are used. For the $B^+ \to D^{*+}D^{*-}K^+$ and $B^0 \to D^{*+}D^{*-}K^0$ branching ratio calculations, the additional uncertainty from the second D^* branching ratio measurements increases the error to 5.1%. Adding the uncertainty of the K_S branching ratio in quadrature does not change this result within the number of significant figures quoted.

[1] No particle identification is performed on the slow pion from the D^* decay.

6.4.8 Efficiency calculation

The calculations of the reconstruction efficiencies in sections 5.1.1 and 5.1.2 have a statistical error of 2.2%. For the calculation of the $B^+ \to D^{*+}D^{*-}K^+$ efficiency in §5.1.3 the statistical uncertainty is 4.4%. Due to the much lower yield in the MC study the $B^0 \to D^{*+}D^{*-}K_S$ efficiency calculation in §5.1.4 has an even higher uncertainty of 6.5%.

6.4.9 Mass resolution discrepancies between data and Monte–Carlo

As can be seen by comparing figures 4.9 and 4.10, and figures 4.11 and 4.12 respectively, the resolution of mass peaks differs between data and MC for D^0 and D^* candidates. This is also true of neutral pion candidates.

To study any systematic error from these resolution differences the effects of varying the size of the mass windows for all the intermediate states by $\pm 1\sigma$ were examined. For the $M(D^*) - M(D^0)$ selection window the cuts were varied by a larger amount, since similar studies found that the differences between data and MC grew in the tail region of the $M(D^*) - M(D^0)$ distribution [102].

Unfortunately, there were not enough events in the signal regions of the $B^+ \to D^{*+}D^{*-}K^+$ or $B^0 \to D^{*+}D^{*-}K_S$ reconstructions to perform a detailed study of these resolution differences. However, the D^0, D^*, and π^0 meson momentum distribution for all four of these doubly charmed B meson decay modes are quite similar, so it is reasonable to assign the error from the $B^0 \to D^{*0}D^{*-}K^+$ study to these other two modes as well.

π^0 selection

Varying the π^0 mass window by $\pm 1\sigma$ varies the branching ratio by -3% for $B^0 \to D^0D^{*-}K^+$ and $B^0 \to D^{*0}D^{*-}K^+$.

D^0 selection

The branching fraction is relatively stable under changes to the D^0 meson selection criteria. The $D^0 \to K\pi$ seems to be well modelled in MC, as changes of $\pm 1\sigma$ to the mass window only expose a difference of $+1\%$ and -3.4%.

Variations in the selection of $D^0 \to K\pi\pi^0$ candidates had a larger effect. The branching fraction varied by as much as $+3\%$ and -7%. The $D^0 \to K\pi\pi\pi$ decay also seems to be less well modelled by the MC generator and `GSIM` – the branching fraction can vary by as much as -7% for tighter mass cuts.

Summing these in quadrature gives an error of $+3\%$ and -10.5%.

D^* selection

While varying the selection cuts for D^* candidates by as much as 3σ exposes a large discrepancy between data and MC, under smaller, more reasonable, variations the branching fraction is relatively stable. By decreasing the selection window by 1σ the branching fraction is increased by as much as 5%. Widening the selection window by 1σ also increases the measurement by about 3%, indicating that the 6σ region chosen in §4.11 is something of a local (stable) minimum.

Examining narrower regions, such as 3 or 4σ results in differences between the data and MC yield of as much as 12%, indicating that many more events may be present in the tails of the $M(D^*) - M(D^0)$ in data than in MC.

The uncertainty is estimated as 5%.

6.4.10 Background events

The branching ratio of $B^+ \to D^{*+}D^{*-}K^+$ is used to estimate the background from these events in the $B^0 \to D^{*0}D^{*-}K^+$ signal region. This branching ratio is measured in §6.3, however the statistical error is large. Varying this branching ratio, and thus the expected background contribution in the $B^0 \to D^{*0}D^{*-}K^+$ signal region, by as much as 2σ changes $\mathcal{B}(B^0 \to D^{*0}D^{*-}K^+)$ by $+7.1\%$ and -5.3%.

Chapter 7

Conclusion

7.1 Conclusion

Doubly charmed B meson decays were investigated using a $78\ \mathrm{fb}^{-1}$ data set of $B\bar{B}$ decays collected at the $\Upsilon(4S)$ resonance by the Belle detector. The branching ratios of $B^0 \to D^{*+}D^{*-}K^0$ and $B^0 \to D^0D^{*-}K^+$ decays are measured using a full reconstruction technique, and the branching ratio of $B^0 \to D^{*0}D^{*-}K^+$ is estimated using a partial technique. These branching ratios are measured to be:

$$\begin{aligned}
\mathcal{B}(B^0 \to D^0D^{*-}K^+) &= (1.66 \pm 0.33 \pm 0.35) \times 10^{-3}, \\
\mathcal{B}(B^0 \to D^{*0}D^{*-}K^+) &= (8.17 \pm 0.80 \pm 1.88) \times 10^{-3}, \\
\mathcal{B}(B^0 \to D^{*+}D^{*-}K^0) &= (7.05 \pm 2.03 \pm 1.97) \times 10^{-3},
\end{aligned}$$

where the first error is statistical and the second error is systematic. Further, an upper limit of

$$\mathcal{B}(B^+ \to D^{*+}D^{*-}K^+) < 1.6 \times 10^{-3},$$

is determined at a 90% confidence level.

The first two branching ratios are also measured using a cleaner subsample, where the additional requirement that at least one of the neutral D mesons decays to the $K\pi$ final state is imposed. When measured using only these decays the branching ratios are found to be:

$$\begin{aligned}
\mathcal{B}(B^0 \to D^0D^{*-}K^+) &= (2.08 \pm 0.33 \pm 0.46) \times 10^{-3}, \\
\mathcal{B}(B^0 \to D^{*0}D^{*-}K^+) &= (7.51 \pm 0.73 \pm 1.73) \times 10^{-3},
\end{aligned}$$

which are consistent with the first result.

These measurements are in good agreement with very recent preliminary results from the BABAR

collaboration [106], where they quote:

$$\begin{aligned}
\mathcal{B}(B^0 \to D^0 D^{*-} K^+) &= (3.1^{+0.4}_{-0.3} \pm 0.4) \times 10^{-3}, \\
\mathcal{B}(B^0 \to D^{*0} D^{*-} K^+) &= (11.8 \pm 1.0 \pm 1.7) \times 10^{-3}, \\
\mathcal{B}(B^0 \to D^{*+} D^{*-} K^0) &= (8.8^{+1.5}_{-1.4} \pm 1.3) \times 10^{-3}, \\
\mathcal{B}(B^+ \to D^{*+} D^{*-} K^+) &= (0.9 \pm 0.4 \pm 0.2) \times 10^{-3},
\end{aligned}$$

using a full reconstruction technique for all modes. In addition, BABAR placed an upper limit of

$$\mathcal{B}(B^+ \to D^{*+} D^{*-} K^+) < 1.8 \times 10^{-3},$$

at a 90% confidence level.

The results of a preliminary Dalitz analysis of $B^0 \to D^0 D^{*-} K^+$ candidates are inconclusive. The available data sample is neither large, nor pure enough to draw any firm conclusions from the three body final state analysis. With the addition of more data collected by the Belle detector in the future, enough decay candidates should be amassed within the cleaner, $K\pi$ requirement subsample to enable a comprehensive search for intermediate hadronic resonances. A full reconstruction of $B^0 \to D^{*0} D^{*-} K^+$, where the momentum of the D^{*0} meson is calculated, would enable a Dalitz analysis of these decays as well, and would extend the search area for these elusive broad charm resonances.

The first indications from an analysis of $B^0 \to D^{*+} D^{*-} K_S$ are promising. Candidate events can be reconstructed with very little background, which could make this mode ideal for studying time dependent *CP* asymmetries once enough events have been collected. This could feasibly occur within the next twelve months, and would also provide further constraints on the parameters of the Unitarity Triangle by measuring $\cos(2\phi_1)$.

7.2 Future developments

A full measurement of the $B \to D^{(*)} \bar{D}^{(*)} K$ inclusive branching fraction may go a long way towards resolving the discrepancy between the number of charmed hadrons per B decay, n_c, and the inclusive semileptonic branching ratio $\mathcal{B}_{\rm sl}$. There are 22 possible modes for doubly charmed B meson decays. The BABAR collaboration has released preliminary branching ratios for all of them [106], and the addition of results from the Belle should help to pin down this issue.

7.2.1 SVD 2.0

One of the major advantages of the BABAR detector over Belle for this sort of analysis is the five layer Silicon Vertex Tracker [107]. This micro vertex detector is not only used to measure vertex locations, but

also to track particles as they travel through the BABAR detector, a feat which Belle's three layer SVD cannot replicate. For analyses such as this one, which contain a large number of low momentum final state particles, the ability to track particles which do not travel far from the IP is invaluable.

Work is nearly complete on the construction of SVD 2.0, the Belle collaboration's solution to this problem. This replacement vertex detector is a four layer device, and will hopefully greatly increase the low momentum track finding efficiency of Belle. It is currently scheduled to be installed in January 2003.

7.2.2 Partial reconstruction

The CLEO Collaboration successfully implemented a partial reconstruction technique which makes use of the kinematic constraints upon the angles between the decay products in $B \to D^*\pi$ decays [108]. Such an analysis could also be performed on $B \to D^{(*)}\bar{D}^{(*)}K$ decays to increase the number of candidate events. However, whether this would come at the cost of sample purity needs to be resolved.

7.2.3 Strong coupling constants

A concurrent measurement of $\mathcal{B}(B^0 \to D^{*-}D_s^{*+})$ and $\mathcal{B}(B^0 \to D^{*-}D^{(*)0}K^+)$ will enable an experimental determination of the strong coupling constants g and h, by eliminating common systematic uncertainties in the measurements [68].

With the addition of more data collected at the $\Upsilon(4S)$ the Dalitz analysis discussed in this thesis may provide conclusive evidence for the existence of the D_{s0} and D_{s1} resonances.

7.2.4 *CP* violation

Better low momentum tracking from SVD 2.0 and higher luminosity will allow for a measurement of time dependent *CP* asymmetry in the decay $B^0 \to D^{*+}D^{*-}K_S$. Although the parameter $\sin(2\phi_1)$, which constrains the Unitarity Triangle, has been measured precisely by both the Belle [40] and BABAR [41] collaborations, examining further decay modes will serve either to increase the precision of the measurement, or to expose shortcomings in the KM mechanism for *CP* violation in the Standard Model. Furthermore, observation of time dependent *CP* asymmetry in these decay modes will enable a measurement of $\cos(2\phi_1)$, hopefully removing some of the discrete ambiguities in the Unitarity Triangle, and will serve as a further test of our understanding of this fundamental area of physics.

Appendix A

Reconstruction effi ciencies

$\bar{B}^0 \to D^{*+}\bar{D}^0 K^-$		Efficiency, ϵ_i, $\times 10^{-2}$		
$D^{*+} \to D^0\pi_s^+$		Experiment 11	Experiment 13	Experiment 17
$D^0 \to K^-\pi^+$	$\bar{D}^0 \to K^+\pi^-$	8.43 ± 0.29	8.23 ± 0.29	8.10 ± 0.29
	$\bar{D}^0 \to K^+\pi^-\pi^0$	2.50 ± 0.16	2.40 ± 0.16	2.73 ± 0.17
	$\bar{D}^0 \to K^+\pi^-\pi^+\pi^-$	3.11 ± 0.18	2.85 ± 0.17	2.73 ± 0.17
$D^0 \to K^-\pi^+\pi^0$	$\bar{D}^0 \to K^+\pi^-$	2.86 ± 0.17	2.84 ± 0.17	2.37 ± 0.16
	$\bar{D}^0 \to K^+\pi^-\pi^0$	0.96 ± 0.10	0.85 ± 0.09	0.91 ± 0.10
	$\bar{D}^0 \to K^+\pi^-\pi^+\pi^-$	0.73 ± 0.09	1.01 ± 0.10	0.58 ± 0.08
$D^0 \to K^-\pi^+\pi^-\pi^+$	$\bar{D}^0 \to K^+\pi^-$	3.21 ± 0.18	3.35 ± 0.18	3.11 ± 0.18
	$\bar{D}^0 \to K^+\pi^-\pi^0$	0.95 ± 0.10	0.98 ± 0.10	0.98 ± 0.10
	$\bar{D}^0 \to K^+\pi^-\pi^+\pi^-$	1.02 ± 0.10	1.21 ± 0.11	0.94 ± 0.10

Table A.1: Reconstruction effi ciency for $\bar{B}^0 \to D^{*+}\bar{D}^0 K^-$ decays in experiment dependent signal MC

$\bar{B}^0 \to D^{*+}\bar{D}^{*0} K^-$		Efficiency, ϵ_i, $\times 10^{-2}$		
$D^{*+} \to D^0\pi_s^+$		Experiment 11	Experiment 13	Experiment 17
$D^0 \to K^-\pi^+$	$\bar{D}^0 \to K^+\pi^-$	8.02 ± 0.29	8.27 ± 0.29	7.47 ± 0.28
	$\bar{D}^0 \to K^+\pi^-\pi^0$	2.40 ± 0.17	2.85 ± 0.17	2.52 ± 0.17
	$\bar{D}^0 \to K^+\pi^-\pi^+\pi^-$	3.00 ± 0.18	3.27 ± 0.19	2.97 ± 0.19
$D^0 \to K^-\pi^+\pi^0$	$\bar{D}^0 \to K^+\pi^-$	2.78 ± 0.17	2.51 ± 0.17	2.59 ± 0.17
	$\bar{D}^0 \to K^+\pi^-\pi^0$	1.10 ± 0.12	1.10 ± 0.10	0.96 ± 0.11
	$\bar{D}^0 \to K^+\pi^-\pi^+\pi^-$	0.99 ± 0.11	1.07 ± 0.11	0.67 ± 0.09
$D^0 \to K^-\pi^+\pi^-\pi^+$	$\bar{D}^0 \to K^+\pi^-$	3.01 ± 0.18	3.28 ± 0.19	3.07 ± 0.18
	$\bar{D}^0 \to K^+\pi^-\pi^0$	1.12 ± 0.11	1.00 ± 0.11	0.92 ± 0.11
	$\bar{D}^0 \to K^+\pi^-\pi^+\pi^-$	0.85 ± 0.10	0.90 ± 0.10	0.81 ± 0.10

Table A.2: Reconstruction effi ciency for $\bar{B}^0 \to D^{*+}\bar{D}^{*0} K^-$ decays in experiment dependent signal MC

$B^- \to D^{*+}D^{*-}K^-$		Efficiency, $\epsilon_i^{\rm fake}$, $\times 10^{-2}$		
$D^{*+} \to D^0\pi_s^+$	$D^{*-} \to \bar{D}^0\pi_s^-$	Experiment 11	Experiment 13	Experiment 17
$D^0 \to K^-\pi^+$	$\bar{D}^0 \to K^+\pi^-$	7.47 ± 0.28	6.66 ± 0.26	6.71 ± 0.27
	$\bar{D}^0 \to K^+\pi^-\pi^0$	2.23 ± 0.16	2.20 ± 0.16	2.14 ± 0.16
	$\bar{D}^0 \to K^+\pi^-\pi^+\pi^-$	2.58 ± 0.17	2.29 ± 0.16	2.23 ± 0.16
$D^0 \to K^-\pi^+\pi^0$	$\bar{D}^0 \to K^+\pi^-$	2.83 ± 0.17	2.54 ± 0.17	2.54 ± 0.17
	$\bar{D}^0 \to K^+\pi^-\pi^0$	0.85 ± 0.10	0.81 ± 0.11	0.66 ± 0.09
	$\bar{D}^0 \to K^+\pi^-\pi^+\pi^-$	0.79 ± 0.09	0.82 ± 0.10	0.80 ± 0.10
$D^0 \to K^-\pi^+\pi^-\pi^+$	$\bar{D}^0 \to K^+\pi^-$	2.52 ± 0.17	2.56 ± 0.16	2.50 ± 0.16
	$\bar{D}^0 \to K^+\pi^-\pi^0$	0.86 ± 0.10	0.84 ± 0.10	0.70 ± 0.10
	$\bar{D}^0 \to K^+\pi^-\pi^+\pi^-$	0.79 ± 0.10	0.84 ± 0.10	0.77 ± 0.10

Table A.3: Fake rate for $\bar{B}^0 \to D^{*+}\bar{D}^{*0}K^-$ from $B^- \to D^{*+}D^{*-}K^-$ decays in experiment dependent signal MC

$B^- \to D^{*+}D^*K^-$		Efficiency, ϵ_i, $\times 10^{-3}$		
$D^{*+} \to D^0\pi_s^+$	$D^{*-} \to \bar{D}^0\pi_s^-$	Experiment 11	Experiment 13	Experiment 17
$D^0 \to K^-\pi^+$	$\bar{D}^0 \to K^+\pi^-$	21.05 ± 1.45	16.50 ± 1.29	20.30 ± 1.43
	$\bar{D}^0 \to K^+\pi^-\pi^0$	5.93 ± 0.78	5.42 ± 0.74	6.87 ± 0.83
	$\bar{D}^0 \to K^+\pi^-\pi^+\pi^-$	6.95 ± 0.84	5.42 ± 0.74	6.77 ± 0.83
$D^0 \to K^-\pi^+\pi^0$	$\bar{D}^0 \to K^+\pi^-$	5.04 ± 0.72	7.01 ± 0.84	7.39 ± 0.87
	$\bar{D}^0 \to K^+\pi^-\pi^0$	3.10 ± 0.56	1.87 ± 0.44	1.15 ± 0.35
	$\bar{D}^0 \to K^+\pi^-\pi^+\pi^-$	2.29 ± 0.48	2.17 ± 0.47	1.26 ± 0.36
$D^0 \to K^-\pi^+\pi^-\pi^+$	$\bar{D}^0 \to K^+\pi^-$	5.76 ± 0.76	7.58 ± 0.87	6.16 ± 0.79
	$\bar{D}^0 \to K^+\pi^-\pi^0$	2.10 ± 0.46	1.79 ± 0.42	1.66 ± 0.41
	$\bar{D}^0 \to K^+\pi^-\pi^+\pi^-$	1.79 ± 0.42	3.09 ± 0.56	2.20 ± 0.47

Table A.4: Reconstruction efficiency for $B^- \to D^{*+}D^{*-}K^-$ decays in experiment dependent signal MC

$\bar{B}^0 \to D^{*+}D^{*-}K_S$		Efficiency, ϵ_i, $\times 10^{-3}$		
$D^{*+} \to D^0\pi_s^+$	$D^{*-} \to \bar{D}^0\pi_s^-$	Experiment 11	Experiment 13	Experiment 17
$D^0 \to K^-\pi^+$	$\bar{D}^0 \to K^+\pi^-$	9.49 ± 0.97	8.87 ± 0.94	7.86 ± 0.89
	$\bar{D}^0 \to K^+\pi^-\pi^0$	2.70 ± 0.52	2.87 ± 0.54	2.70 ± 0.52
	$\bar{D}^0 \to K^+\pi^-\pi^+\pi^-$	3.48 ± 0.59	3.78 ± 0.62	2.30 ± 0.48
$D^0 \to K^-\pi^+\pi^0$	$\bar{D}^0 \to K^+\pi^-$	2.66 ± 0.52	2.78 ± 0.53	2.58 ± 0.51
	$\bar{D}^0 \to K^+\pi^-\pi^0$	0.50 ± 0.22	0.50 ± 0.22	0.90 ± 0.30
	$\bar{D}^0 \to K^+\pi^-\pi^+\pi^-$	0.60 ± 0.24	0.27 ± 0.17	0.39 ± 0.20
$D^0 \to K^-\pi^+\pi^-\pi^+$	$\bar{D}^0 \to K^+\pi^-$	2.85 ± 0.54	2.85 ± 0.54	2.87 ± 0.54
	$\bar{D}^0 \to K^+\pi^-\pi^0$	1.00 ± 0.32	1.30 ± 0.36	1.64 ± 0.38
	$\bar{D}^0 \to K^+\pi^-\pi^+\pi^-$	0.80 ± 0.28	0.77 ± 0.28	9.00 ± 0.30

Table A.5: Reconstruction efficiency for $\bar{B}^0 \to D^{*+}D^{*-}K_S$ decays in experiment dependent signal MC

Bibliography

[1] Aristotle. *Physics.* Oxford University Press, 1996. Translated by Robin Waterfield.

[2] A. D. Sakharov. Violation of *CP* invariance, C asymmetry, and baryon asymmetry of the universe. *Pisma Zh. Eksp. Teor. Fiz.*, 5:32–35, 1967.

[3] Kamiokande Collaboration, Y. Fukuda, et al. Atmospheric muon–neutrino / electron–neutrino ratio in the multiGeV energy range. *Physics Letters B*, 335:237–245, 1994.

[4] Super-Kamiokande Collaboration, Y. Fukuda, et al. Evidence for oscillation of atmospheric neutrinos. *Physical Review Letters*, 81:1562–1567, 1998.

[5] Super-Kamiokande Collaboration, S. Fukuda, et al. Solar ^8B and hep neutrino measurements from 1258 days of Super–Kamiokande data. *Physical Review Letters*, 86:5651–5655, 2001.

[6] SNO Collaboration and M. S. Neubauer. First solar neutrino observations from SNO. *International Journal of Modern Physics A*, 16S1B:715–717, 2001.

[7] Particle Data Group. *Review of Particle Physics*, volume 15. Springer, 2000. The European Physical Journal C.

[8] Steven Weinberg. A model for leptons. *Physical Review Letters*, 19:1264–1266, 1967.

[9] A. Salam. Weak and electromagnetic interactions. In N. Svartholm, editor, *Elementary Particle Theory*, Nobel Symposium No. 8. Almqvist and Wiksell, Stockholm, 1969.

[10] S.L. Glashow. Partial symmetries of weak interactions. *Nuclear Physics*, 22:579–588, 1961.

[11] N. Cabibbo. Unitary symmetry and leptonic decays. *Physical Review Letters*, 10:531, 1963.

[12] M. Kobayashi and T. Maskawa. *CP* violation in the renormalizable theory of weak interaction. *Progress of Theoretical Physics*, 49:652–657, 1973.

[13] H. Fritzsch and M. Gell-Mann. Current algebra: Quarks and what else? In J.D. Jackson and A. Roberts, editors, *Proc. XVI Int. Conf. on High Energy Physics*, Batavia, Ill., 1972. National Accelerator Laboratory.

[14] W.J. Marciano and H. Pagels. Quantum chromodynamics. *Physics Reports*, 36C:137, 1978.

[15] W.E. Caswell and G.P. Lepage. Effective Lagrangian for bound state problems in QED, QCD and other field theories. *Physics Letters B*, 167:437, 1986.

[16] E. Eichten. Heavy quarks on the lattice. *Nuclear Physics (Proceedings, supplements)*, 4:170, 1988.

[17] G.P. Lepage and B.A. Thacker. Effective Lagrangians for simulation of heavy quark systems. *Nuclear Physics (Proceedings, supplements)*, 4:199, 1988.

[18] J. Schwinger. The theory of quantized fields. I. *Physical Review*, 82:914, 1951.

[19] J. Schwinger. The theory of quantized fields. II. *Physical Review*, 91:713, 1951.

[20] G Lüders. *Kgl. Dansk. Vidensk. Selsk. Mat.-Fys. Medd.*, 28:5.

[21] W. Pauli. *Niels Bohr and the Development of Physics*. McGraw–Hill, New York, 1955.

[22] T.D. Lee and C.N. Yang. Question of parity conservation in weak interactions. *Physical Review*, 104:254, 1956.

[23] C.S. Wu, E. Ambler, R.W. Hayward, D.D. Hoppes, and R.P. Hudson. Experimental test of parity conservation in beta decay. *Physical Review*, 105:1413, 1957.

[24] R.L. Garwin, L.M. Lederman, and M. Weinrich. Observations of the failure of conservation of parity and charge conjugation in meson decays: the magnetic moment of the free muon. *Physical Review*, 105:1415, 1957.

[25] J.L. Friedman and V.L. Telegdi. Nuclear emulsion evidence for parity nonconservation in the decay chain $\pi^+ \to \mu^+ \to e^+$. *Physical Review*, 106:1290, 1957.

[26] M. Gell-Mann and A. Pais. Behaviour of neutral particles under charge conjugation. *Physical Review*, 97:1387, 1955.

[27] J.H. Christenson, J.W. Cronin, V.L. Fitch, and R. Turlay. Evidence for the 2π decay of the K_2^0 meson. *Physical Review Letters*, 13(4):138–140, 1964.

[28] S. L. Glashow, J. Iliopoulos, and L. Maiani. Weak interactions with lepton–hadron symmetry. *Physical Review D*, 2:1285–1292, March 1970.

[29] Lincoln Wolfenstein. Parametrization of the Kobayashi–Maskawa matrix. *Physical Review Letters*, 51(21):1945 – 1947, 1983.

[30] Ashton B. Carter and A. I. Sanda. *CP* nonconservation in cascade decays of B mesons. *Physical Review Letters*, 45:952–954, 1980.

[31] Ashton B. Carter and A. I. Sanda. *CP* violation in B–meson decays. *Physical Review D*, 23:1567–1579, 1981.

[32] Ikaros I.Y. Bigi and A.I. Sanda. Notes on the observability of *CP* violations in B decays. *Nuclear Physics B*, 193:85, 1981.

[33] MAC Collaboration, E. Fernandez, et al. Lifetime of particles containing b quarks. *Physical Review Letters*, 51:1022–1025, 1983.

[34] MARKII Collaboration, N. S. Lockyer, et al. Measurement of the lifetime of bottom hadrons. *Physical Review Letters*, 51:1316–1319, 1983.

[35] ARGUS Collaboration, H. Albrecht, et al. Observation of $B^0 - \bar{B}^0$ mixing. *Physics Letters B*, 192: 245, 1987.

[36] KTeV Collaboration, A Alavi-Harati, et al. Observation of direct *CP* violation in $K_{S,L} \rightarrow \pi\pi$ decays. *Physical Review Letters*, 83:22–27, 1999.

[37] NA48 Collaboration, V Fanti, et al. A new measurement of direct *CP* violation in two pion decays of the neutral kaon. *Physics Letters B*, 465:335–348, 1999.

[38] Matthias Neubert. B physics and *CP* violation. *International Journal of Modern Physics A*, 11: 4173–4240, 1996.

[39] Yosef Nir and Helen R. Quinn. Theory of *CP* violation in B decays. SLAC–PUB–5643, in B Physics, ed. by S. Stone, World Scientific, 1994.

[40] Belle Collaboration, K. Abe, et al. An improved measurement of mixing–induced *CP* violation in the neutral B system. BELLE–CONF–0201, Preprint hep–ex/0207098, 2002.

[41] BABAR Collaboration, B. Aubert, et al. Measurement of the *CP*–violating asymmetry amplitude $\sin 2\beta$. BABAR –PUB–02/008, Preprint hep–ex/0207042, 2002.

[42] Isard Dunietz, Helen Quinn, Art Snyder, and Walter Toki. How to extract *CP*-violating asymmetries from angular correlations. *Physical Review D*, 43(7):2193, April 1991.

[43] Guido Michelon. A theoretical review of the $B \rightarrow D^{(*)}\bar{D}^{(*)}$ decay channel. SLAC–BABAR–NOTE 342, 1996.

[44] Jonathan L. Rosner. Determination of pseudoscalar-charmed-meson decay constants from B–meson decays. *Physical Review D*, 42(11):3732, December 1990.

[45] Zhi zhong Xing. New time distributions of $D^0 - \bar{D}^0$ or $B^0 - \bar{B}^0$ mixing and *CP* violation. *Physics Letters B*, 463:323–329, 1999.

[46] Xuan-Yem Pham and Zhi zhong Xing. *CP* asymmetries in $B_d \to D^{*+}D^{*-}$ and $B_s \to D_s^{*+}D_s^{*-}$ decays: P-wave dilution, penguin and rescattering effects. *Physics Letters B*, 458:375–382, 1999.

[47] J. Charles, A. Le Yaouanc, L. Oliver, O. Pène, and J.-C. Raynal. $B_d^0(t) \to DPP$ time-dependent Dalitz plots, *CP*-violating angles 2β, $2\beta + \gamma$, and discrete ambiguities. *Physics Letters B*, 425: 375–387, 1998. Erratum–ibid vol 433, p441.

[48] Yuval Grossman and Helen R. Quinn. Removing discrete ambiguities in *CP* asymmetry measurements. *Physical Review D*, 56:7259–7266, 1997.

[49] Amol S. Dighe, Isard Dunietz, and Robert Fleischer. Resolving a discrete ambiguity in the CKM angle β through $B_{u,d} \to J/\psi\, K^*$ and $B_s \to J/\psi\, \phi$ decays. *Physics Letters B*, 433:147–149, 1998.

[50] P. Colangelo, F. De Fazio, G. Nardulli, N. Paver, and Riazuddin. Analysis of the three-body $B \to D^+D^-\pi^0$ decay. *Physical Review D*, 60(033002), 1999.

[51] T.E. Browder, A. Datta, P.J. O'Donnel, and S. Pakvasa. Measuring β in $B \to D^{(*)+}D^{(*)-}K_s$ decays. *Physical Review D*, 61(054009), 2000.

[52] Guido Altarelli and S. Petrarca. Inclusive beauty decays and the spectator model. *Physics Letters B*, 261:303–310, 1991.

[53] Ikaros I. Y. Bigi, Boris Blok, Mikhail A. Shifman, and Arkady I. Vainshtein. The baffling semileptonic branching ratio of B mesons. *Physics Letters B*, 323:408–416, 1994.

[54] Adam F. Falk, Mark B. Wise, and Isard Dunietz. Inconclusive inclusive nonleptonic B decays. *Physical Review D*, 51:1183–1191, 1995.

[55] Emilio Bagan, Patricia Ball, Vladimir M. Braun, and P. Gosdzinsky. Charm quark mass dependence of QCD corrections to nonleptonic inclusive B decays. *Nuclear Physics B*, 432:3–38, 1994.

[56] E. Bagan, Patricia Ball, Vladimir M. Braun, and P. Gosdzinsky. Theoretical update of the semileptonic branching ratio of B mesons. *Physics Letters B*, 342:362–368, 1995.

[57] E. Bagan, Patricia Ball, B. Fiol, and P. Gosdzinsky. Next-to-leading order radiative corrections to the decay $b \to ccs$. *Physics Letters B*, 351:546–554, 1995.

[58] M.B. Voloshin. QCD radiative enhancement of the decay $b \to c\bar{c}s$. *Physical Review D*, 51:3948, 1995.

[59] Isard Dunietz. $B_s - \bar{B}_s$ mixing, *CP* violation, and extraction of CKM phases from untagged B_s data samples. *Physical Review D*, 52:3048–3064, 1995.

[60] T.E. Browder and K. Honscheid. B mesons. *Progress in Particle and Nuclear Physics*, 35:81, 1995.

[61] Gerhard Buchalla, Isard Dunietz, and Hitoshi Yamamoto. Hadronization of $b \to c\bar{c}s$. *Physics Letters B*, 364:188, December 1995.

[62] CLEO Collaboration. Exclusive reconstruction of $\bar{B} \to D^{(*)}\bar{D}^{(*)}K^{-}$. CLEO CONF 97-26, 1997.

[63] CLEO Collaboration, T.E. Coan, et al. Flavor-specific inclusive B decays to charm. *Physical Review Letters*, 80:1150–1155, 1998.

[64] M. Neubert and Christopher T. Sachrajda. Spectator effects in inclusive decays of beauty hadrons. *Nuclear Physics B*, 483:339–370, 1997.

[65] W.F. Palmer and Berthold Stech. Inclusive nonleptonic decays of B and D mesons. *Physical Review D*, 48:4174, 1993.

[66] BABAR Collaboration. Investigation of $B \to D^{(*)}\bar{D}^{(*)}K$ decays with the BABAR detector. BABAR–CONF–01/01, 2001.

[67] Belle Collaboration. Measurements of the branching fractions for $B \to D^{(*)}D^{(*)}$ and $B \to D^{(*)}D^{(*)}K$ at Belle. Belle–CONF–0104, 2001.

[68] P. Colangelo and F. De Fazio. On three–body $B^0 \to D^{*-}D^{(*)0}K^{+}$ decays and couplings of heavy mesons to light pseudoscalar mesons. *Physics Letters B*, 532:193–201, 2002. Preprint hep–ph/0201305.

[69] M. Beneke, G. Buchalla, M. Neubert, and C.T. Sachrajda. QCD factorization for exclusive non–leptonic B–meson decays: general arguments and the case of heavy–light final states. *Nuclear Physics B*, 591:313–418, 2000.

[70] CLEO Collaboration, A. Anastassov, et al. First measurement of $\Gamma(D^{*+})$ and precision measurement of $m_{D^{*+}} - m_{D^0}$. *Physical Review D*, 65(032003), 2002.

[71] Damir Becirevic and Alain Le Yaouanc. $\hat{g}$–coupling $(g_{B^*B\pi}, g_{D^*D\pi})$. A quark model with Dirac equation. *JHEP*, 03:021, 1999.

[72] A. Abada, D. Bećirević, Ph. Boucaud, G. Herdoiza, J.P. Leroy, A. Le Yaouanc, O. Pène, and J. Rodríguez-Quintero. First lattice QCD estimate of the $g_{D^*D\pi}$ coupling. Preprint hep–ph/0206237, June 2002.

[73] Paul Singer. Radiative decays of heavy mesons and the determination of the strong g–coupling. *Acta Phys. Polon. B*, 30:3849–3859, 1999. Preprint hep-ph/9910558.

[74] Dmitri Melikhov and Michael Beyer. Pionic coupling constants of heavy mesons in the quark model. *Physics Letters B*, 452:121–128, 1999.

[75] D. Melikhov and B. Stech. Weak form factors for heavy meson decays: An update. *Physical Review D*, 62(14006), 2000.

[76] Mark B. Wise. Chiral perturbation theory for hadrons containing a heavy quark. *Physical Review D*, 45:2188–2191, 1992.

[77] Gustavo Burdman and John F. Donoghue. Union of chiral and heavy quark symmetries. *Physics Letters B*, 280:287–291, 1992.

[78] Tung-Mow Yan, Hai-Yang Cheng, Chi-Yee Cheung, Guey-Lin Lin, Y.C. Lin, and Hoi-Lai Yu. Heavy–quark symmetry and chiral dynamics. *Physical Review D*, 46:1148–164, 1992.

[79] Adam F. Falk and Michael E. Luke. Strong decays of excited heavy mesons in chiral perturbation theory. *Physics Letters B*, 292:119–127, 1992.

[80] P. Colangelo, F. De Fazio, G. Nardulli, N. Di Bartolomeo, and R. Gatto. Strong coupling of excited heavy mesons. *Physical Review D*, 52(11):6422–6434, 1995.

[81] P. Colangelo and F. De Fazio. QCD interactions of heavy mesons with pions by light–cone sum rules. *The European Physical Journal C*, 4:503–511, 1998.

[82] KEKB B–factory design report. Technical Report 95-7, KEK, 1995.

[83] Belle Collaboration. The Belle detector. Progress Report 2000–4, KEK.

[84] URL `http://www.lns.cornell.edu/public/CLEO/soft/QQ`.

[85] R. Itoh. *QQ quick reference for Belle*. `http://belle.kek.jp/~software/qq/html/belle_qq.html`.

[86] R. Brun et. al. `GEANT3` user's guide. CERN DD/EE/84-1.

[87] H. Ozaki. Mini–DST tables V0.0. Belle Note 146, 1996.

[88] Brendan Casey. HadronB. Belle Note 390, 2001.

[89] G. Fox and S. Wolfram. Observables for the analysis of event shapes in e^+ e^- annihilation and other processess. *Physical Review Letters*, 41:1581, 1978.

[90] B. C. K. Casey. Measurement of the number of $B\bar{B}$ events in experiment 5 data and the $B\bar{B}$ cross section at KEKB. Belle Note 296, 2000.

[91] Tracking Group. Charged particle tracking in Belle. Belle Note 327, 2000.

[92] Y. Teramoto. Track extrapolations in the non–uniform magnetic field. Belle Note 188, 1997.

[93] Yukiyoshi Ohnishi. Track parameterization. Belle Note 148, 1996.

[94] KID Group, H. Hamasaki, T. Iijima, et al. Kaon identification in Belle. Belle Note 321, 2000.

[95] Junichi Tanaka. KFitter usage and effect. Belle Note 193, 1998.

[96] Junichi Tanaka. Kinematic fitting. Belle Note 194, 1998.

[97] F. Fang. Study of $K_S \to \pi^+\pi^-$ selection. Belle Note 323, 2000.

[98] ARGUS Collaboration, H. Albrecht, et al. Search for $b \to s\gamma$ in exclusive decays of B mesons. *Physics Letters B*, 229:304, 1989.

[99] ARGUS Collaboration, H. Albrecht, et al. Search for hadronic $b \to u$ decays. *Physics Letters B*, 241:278, 1990.

[100] Mikihiko Nakao, Hitomi Ikeda, Yutaka Ushiroda, and Shohei Nishida. Study of radiative decay $B \to K^*\gamma$ with Belle. Belle Note 333, 2000.

[101] Jiwoo Nam. Track finding efficiency study using η sample. Belle Note 434, 2001.

[102] Yoshihito Iwasaki. A measurement of $B \to D^{*\pm}D^{\mp}$ branching fraction. Belle Note 474, 2002.

[103] T. Aushev. Study of the $\pi^-_{\rm slow}$ efficiency using $B^0 \to D^{*-}\pi^+$ decay. Belle Note 480, 2002.

[104] Belle Collaboration, K. Abe, et al. Measurement of inclusive production of neutral pions from $\Upsilon(4S)$ decays. *Physical Review D*, 64(072001), 2001.

[105] Y. Unno. URL `http://bsunsrv1.kek.jp/secured/kid/performance/dstar_v6.0_e15/dstar.htm%l`.

[106] BABAR Collaboration. Measurement of the branching fractions for the exclusive decays of B^0 and B^+ to $\bar{D}^{(*)}D^{(*)}\ K$. BABAR –CONF–02/19, July 2002.

[107] Robert P. Johnson. BABAR silicon vertex tracker. *Nuclear Instruments and Methods in Physics Research Section A*, 383:7–12, 1996.

[108] CLEO Collaboration, G. Brandenberg, et al. New measurement of $B \to D^*\pi$ branching fractions. *Physical Review Letters*, 80(13):2762, March 1998.